A Si Photonic BiCMOS Coherent Quadrature Phase Shift Keying Transmitter based on Ring Modulators

Youngkwan Jo

The Graduate School

Yonsei University

Department of Electrical and Electronic Engineering

A Si Photonic BiCMOS Coherent Quadrature Phase Shift Keying Transmitter based on Ring Modulators

by

Youngkwan Jo

A Dissertation

Submitted to the Department of Electrical and Electronic Engineering

and the Graduate School of Yonsei University

in partial fulfillment of the requirements for the degree of

Doctor of Philosophy

December 2023

This certifies that the dissertation of Youngkwan Jo is approved.

_____

Thesis Supervisor: Woo-Young Choi

_____

Sang-Kook Han

_____

Donghyun Kim

_____

Minkyu Kim

_____

Lars Zimmermann

The Graduate School

Yonsei University

December 2023

Table of Contents

List of Tables

List of Figures

Abstract

A Si Photonic BiCMOS Coherent Quadrature Phase Shift Keying Transmitter based on Ring Modulators

Youngkwan Jo

Dept. of Electrical and Electronic Engineering

The Graduate School

Yonsei University

The rapid growth of data centers, driven by ever-increasing data traffic demands from various applications, has led to the transition from electrical interconnects to optical interconnects with the advantages of the performance, compactness and high data capacities. Silicon photonics emerges as a promising solution for optical interconnects to mass-produce photonic integrated circuits (PICs), fully exploiting the cost-effectiveness and scalability of silicon-on-insulator processes.

There have been two major trends in modulation formats for optical transceivers, intensity-modulation direct-detection (IM/DD) and coherent optical modulation. Coherent modulation offers several advantages such as reduced receiver sensitivity requirements, scalability through polarization and higher-order modulation with its reduced demands for wavelength parallelization. Coherent optical transceivers are moving to the short-reach data center interconnect application with decreased complexity from simplified digital-signal processing (DSP) and receiver architectures.

Integration of efficient optical modulators play a crucial role in achieving low-power and high-capacity Si photonic optical transceivers, and for this, depletion-type Si ring modulators (RMs) have shown their great potentials thanks to small device footprint, large modulation bandwidth and high energy efficiency for the increasing performance requirements, as a promising candidate for replacing Si Mach-Zehnder modulators (MZMs) for various applications. In addition, the Si RM offers a solution for the transition from pluggable transceivers to co-packaged optics (CPOs) where compact device size and low power consumption are essential factors.

The potentials of the RMs for efficient coherent optical transmitters in high-speed data center interconnect are explored. A Si coherent

transmitter electronic-photonic integrated circuit (EPIC) based on the Si RMs is demonstrated for 28-Gbaud quadrature-phase-shift keying signals within 0.25-μm Si photonic BiCMOS process, which allows the co-integration of the photonic devices, high-performance SiGe hetero-bipolar transistors (HBTs) and CMOS electronic circuits. To realize the efficient device, the Si RMs are characterized and optimized for the phase modulation. The performance of the fabricated coherent transmitter is evaluated and demonstrated with the coherent receiver EPIC implemented in the same photonic BiCMOS process for the various measurement configurations such as optical signal sources, showing the possibilities as a RM-based coherent transmitter EPIC and a monolithic all-silicon coherent transceiver sub-assembly. In addition, an analysis to improve performance of coherent modulators/transmitter based on RMs is investigated.

Keywords**:** optical interconnect, Si photonics, Si photonic BiCMOS process, monolithic integration, electronic-photonic integrated circuit (EPIC), coherent optical communications, quadrature phase shift keying (QPSK) modulators, coherent transmitters, ring modulators (RMs), modulator driver electronics, coherent receivers.

1. Introduction

1.1. Optical Interconnect

Fig. 1-1. World's biggest data center as of 2023, China Telecom Data Center Inner Mongolia Information Park [1].

Fig. 1-1 shows the China Telecom Data Center, currently the world's largest data center located in Inner Mongolia [1]. Over less than a century, data centers have evolved to the colossal 10,763,910 ft^2 China Telecom Data Center with a power consumption of 150 MW. The reason behind the scaling up of data centers is the explosive growth in demand for data traffic, driven by various internet-based applications such as cloud computing, artificial intelligence (AI), machine learning (ML), social network services (SNS), and multimedia streaming. Data centers consist of numerous servers, racks, and an

optical switching network, in addition to transceivers composed of transmitters, receivers, and various sub-blocks, these are designed to transmit and receive real-time data for various applications.

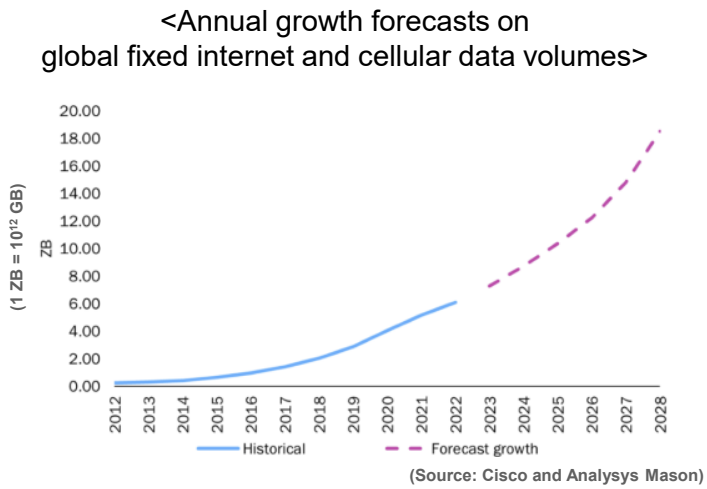

Fig. 1-2. Annual growth forecast on global fixed internet and cellular data volumes (ZB=10^{12} GB) [2].

As shown in Fig. 1-2, annual global internet traffic continues to grow steadily, with the data traffic projected to reach 18.5 zettabytes (ZB; 1 ZB = 10^{12} GB) by 2028, nearly three times the volume of 2022 [2]. To accommodate this explosive annual growth in global data traffic, data centers have continuously increased their overall throughput with ever-increasing number of transceivers with higher data capacities.

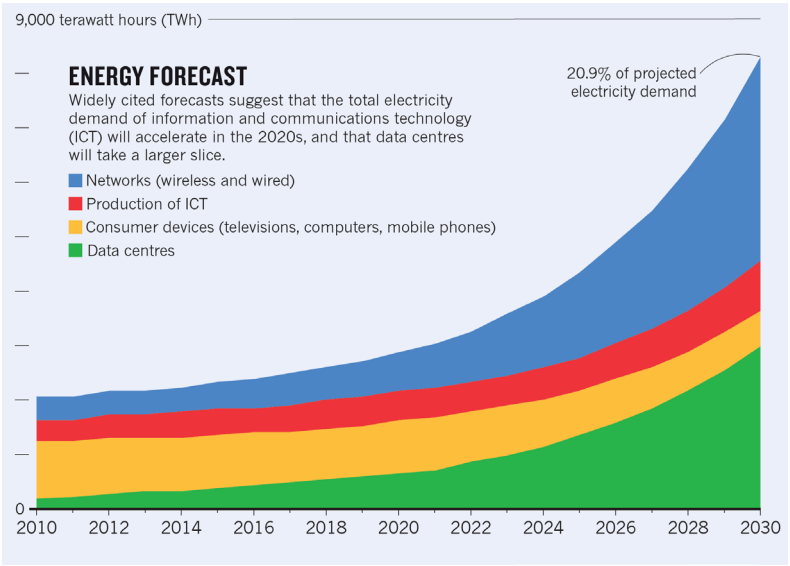

Fig. 1-3. Annual energy usage forecast for overall information and communication technology (ICT) until 2030 [3].

Fig. 1-3 shows an annual energy usage forecast of the information and communication technology (ICT) field until 2030 [3]. The overall power consumption in the ICT is expected to surge in the 2020s, with data centers contributing significantly to both the absolute and proportional amount of power consumed. This is due to the increasing number of data centers worldwide and the rising volume of internet traffic that individual data centers must handle, resulting in a geometric increase in power consumption. Consequently, minimizing the power consumption of individual hardware components within data centers while increasing the data capacity has become a crucial design focus.

This solves not only the performance enhancement of data centers but also the societal and environmental issues arising from the growing power demands [4].

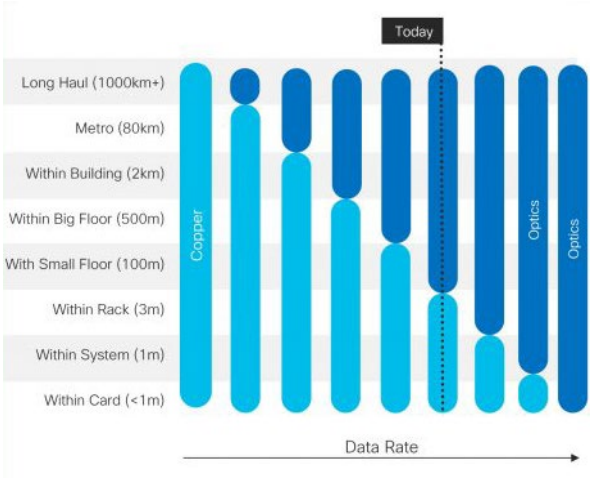

Fig. 1-4. Electrical (copper) interconnect vs optical interconnect for distance and data rate [5].

Data center interconnect (DCI) has evolved from copper-based electrical interconnects, which are currently unable to achieve the high link performance, compactness, lightweight and high transmission capacity required for supporting the demands on the internet traffic. The trend has shifted towards fiber-based optical interconnects, which can achieve the performance requirements. Fig. 1-4 illustrates the border between electrical and optical interconnects based on required data rates and transmission distances [5]. In the past, optical

interconnects had been mainly used for long-haul and metro transmission over 80 km but have expanded into DC-to-DC interconnects covering distances of several kilometers, and even intra-DC rack-to-rack and system-to-system connections within a few meters.

1.2. Silicon Photonics

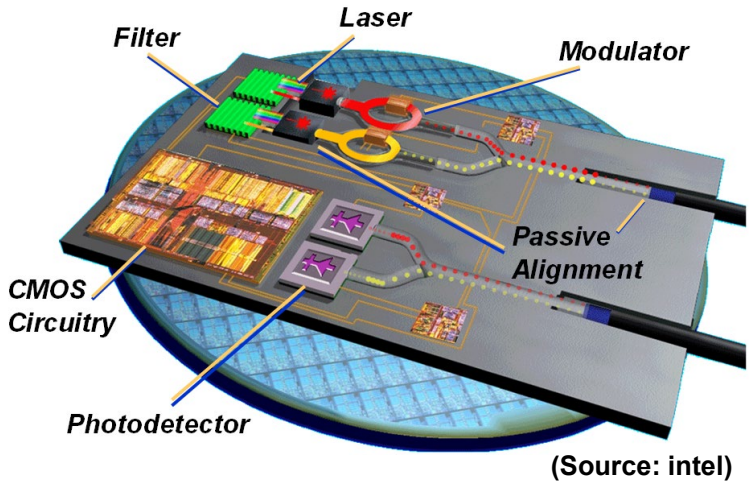

Fig. 1-5. Silicon photonic integrated circuit and its key components [6].

Silicon photonics is a fabrication technology for optical interconnects such as modulators, photodetectors and filters as photonic integrated circuits (PICs) on silicon-on-insulator (SOI) substrates [7-9], as shown in Fig. 1-5. Silicon photonics has evolved based on the mass producibility and cost-effectiveness of the silicon complementary-metal-oxide-semiconductor (CMOS) process which has been driven by the development of the integrated circuits (ICs) industry. It has gained momentum from various research and development efforts in hyper-scale DCI [10,11], bio- and chemical-sensors [12,13], light detection and ranging (LiDAR) [14,15], microwave photonics [16] and newly

emerging quantum computing [17] and neuromorphic photonics [18].

Because of the tremendous cost required for initial development and maintenance of the fabrication process for Si PICs, a fabless ecosystem for Si PIC industry has been established, where multiple users share a 200-mm or 300-mm wafer process run through multiple-wafer-runs (MPW) to manufacture PICs needed for various applications [19,20]. Fig. 1-6 presents worldwide manufacturers offering Si PIC foundry services at prototyping, CMOS pilot and industrial levels [21]. Table 1-1 shows the process specifications of representative examples of worldwide Si PIC foundries: IHP [22], IMEC [23], GlobalFoundries (GF) [24] and AMF [21]. Most of these processes are SOI-based, enabling tight confinement of optical modes due to the high refractive index contrast between silicon and silicon oxide. They also provide additional integration of silicon nitride (SiN) to enhance fabrication tolerance and achieve design diversity and stability required for various applications.

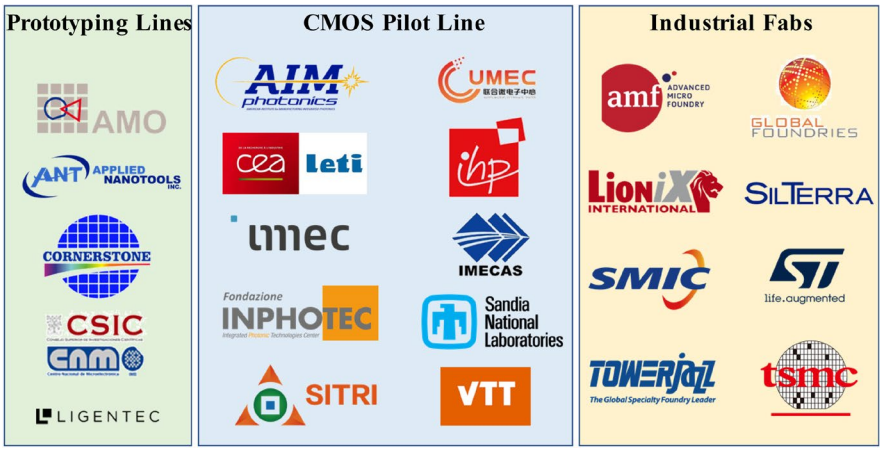

Fig. 1-6. Worldwide Si PIC foundries providing open access fabrication services [21].

Foundries	IHP	IMEC	GF	AMF
MPW platform	SOI	SOI	SOI	SOI/SiN
Wafer size (mm)	200	200	300	200
Film thickness (nm)	220	220	170	220 (SOI)/ 400 (SiN)
Process line	248nm	193nm	193nm (immersion)	193nm (Si)/ 248nm (SiN)
Minimum CD (nm)	-	130	90	120 (Si)/ 300 (SiN)
Typical MPW area (mm^2)	10	26.5	25	44.8

Table 1-1. Process specifications of Si PIC foundries examples [21-24].

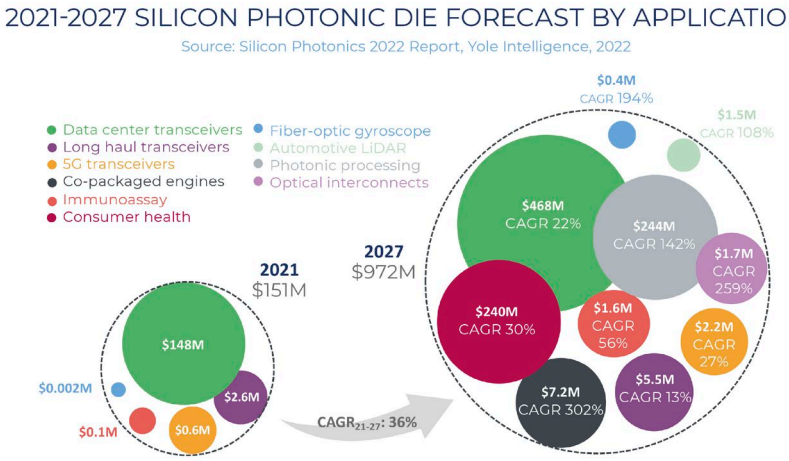

Fig. 1-7. Silicon photonic IC market forecast by applications from 2021 to 2027 [25].

(a)

(b)

Fig. 1-8(a) Intel's silicon photonics optical transceiver product for 400G (4-lane x 100G) data center reach, (400G DR4+ QSFP-DD) [26], (b) Cisco's 51.2Tbps (512-lane x 112G) co-packaged optic (CPO) product (Cisco Silicon One G200) [27].

Fig. 1-7 presents market forecasts for Si photonics by applications from 2021 to 2027 [25]. The market size is expected to grow at a

compound annual growth rate (CAGR) of 36% from 2021 to 2027. As shown in the figure, Si photonics is not only significantly contributing to optical transceivers for DCI, long-haul, and 5G applications but is also expected to find diverse applications such as photonic processing and consumer health in the future.

Silicon is a suitable material for telecommunication wavelengths at 1550 nm (C-band) and 1310 nm (O-band). Si photonic ICs can provide a high-volume production solution for optical transceivers as in Fig. 1-8(a), which is essential for accelerating high-capacity DCs [26]. Recently, co-packaged optics (CPOs) have become a trend in DCI, as in Fig. 1-8(b), where optical transceivers composed of transmitters, receivers and signal processing electronics and switching networks are co-integrated in a single 2.5D or 3D silicon package [27]. This trend is because the power consumption and device footprint consumed by all devices can be dramatically reduced, and higher data capacity required for DCI networks can be achieved from the integration of required sub-blocks for transceiver and switch together.

Si photonics has the drawback of requiring hybrid integration with III-V semiconductors as optical laser sources and suffering from inefficient direct modulation by electric fields. Among the photonic components consisting of optical transceiver, passive components such

as fiber-to-chip couplers, waveguides, and optical hybrids, as well as active components like Ge-on-Si photodetectors, are typically provided to PIC designers as a part of a process design kit (PDK) [24], [21]. However, because Si electro-optical (E/O) modulators based on the free-carrier effect have various performance metrics such as a driving voltage, 3-dB bandwidth, Q factor, insertion loss and extinction ratio, the performance optimization of optical modulators is essential for efficient implementation of low-power and high-capacity Si photonic optical transceivers [8], [10].

1.3. Coherent Optical Modulation

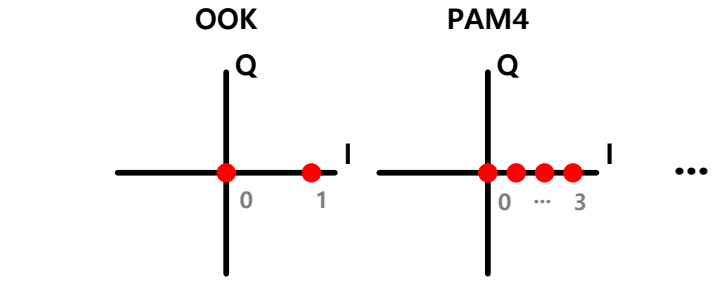

(a)

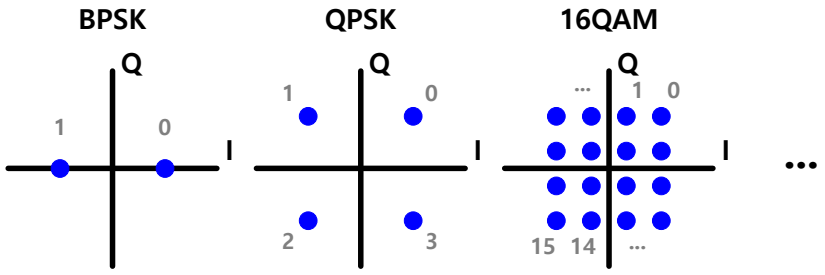

(b)

Fig. 1-9. Example constellations of (a) intensity modulation format such as on-off keying (OOK) and 4-level pulse amplitude modulation (PAM4), (b) coherent modulation format such as binary phase shift keying (BPSK), quadrature phase shift keying (QPSK) and quadrature amplitude modulation (QAM) (I: in-phase, Q: quadrature).

A modulator is a device that converts data into a physical signal, and it is a key hardware component that determines and influences on the overall performance of a transmitter or transceiver [8], [10], [21].

Various optical modulation formats have been developed and implemented over time to modulate different characteristics of optical signals such as intensity, phase, polarization and optical mode based on the type of input data. Fig. 1-9 shows two major streams in digital modulation formats to achieve higher data capacity in transceivers. Fig. 1-9(a) shows modulation formats that modulate the intensity of optical signals, such as on-off keying (OOK) and 4-level pulse amplitude modulation (PAM4) [11], while Fig. 1-9(b) shows coherent modulation formats that modulate the phase or phase/intensity of optical signals, including binary phase shift keying (BPSK), quadrature phase shift keying (QPSK), and quadrature amplitude modulation (QAM) [28].

Fig. 1-10(a) shows conventional receiver architectures for the intensity modulation (IM) such as OOK and PAM4 which perform direct detection (DD) by measuring the optical signal's intensity using a photodiode and a receiver (Rx) front-end electronic integrated circuit (EIC) composed of trans-impedance amplifiers (TIAs) [29], etc. In contrast, coherent modulation formats such as QPSK and QAM use conventional coherent receiver architectures, as in Fig. 1-10(b), consisting of optical hybrids, photodiodes, and Rx front-end EICs for in-phase (I) and quadrature (Q) channels [28].

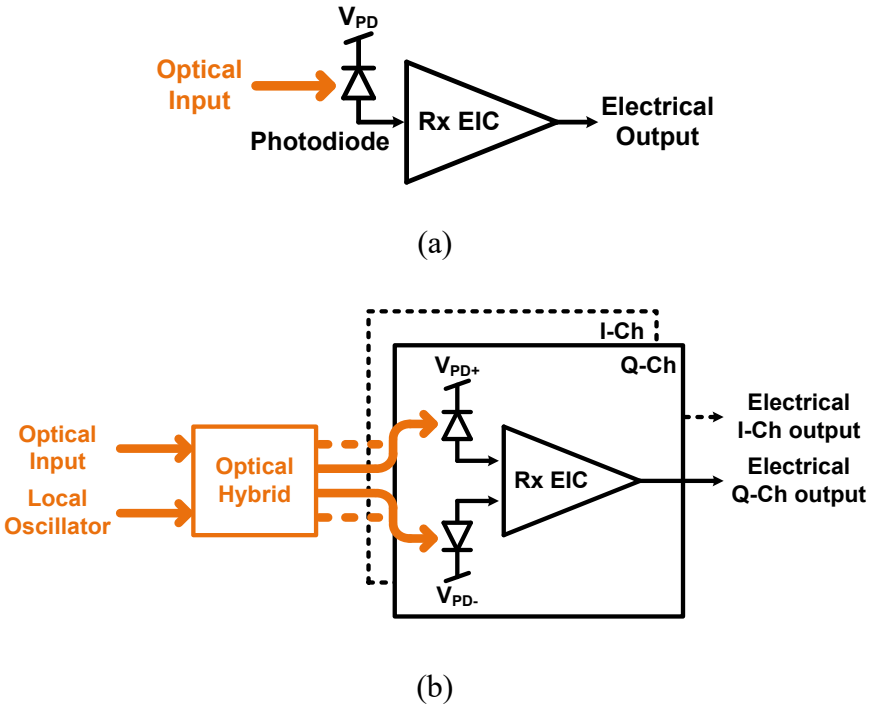

Fig. 1-10. Conventional receiver architecture for (a) intensity modulation / direct detection (IM/DD), (b) coherent modulation.

One notable aspect of conventional coherent receivers is the presence of a local oscillator (LO) for the demodulation. This allows coherent optical receivers to have a lower sensitivity requirement compared to direct detection receivers due to the additional signal power gain from the LO [30]. However, the presence of a free-running LO introduces signal impairments during transmission such as carrier phase noise which consequently requires the recovery using digital signal processing (DSP), and this, in turn, leads to higher power

consumption in DSP blocks [31]. On the other hand, DD receivers have a relatively simpler structure compared to coherent receivers and have lower power consumption due to their simpler DSP algorithm requirements [30].

To increase the data capacity of transceivers, in the case of IM/DD formats, it is necessary to directly scale the bandwidth of individual components such as modulators, modulator driver electronics, receivers as well as the entire system, while in the case of the coherent, data capacity scaling is relatively easy to achieve thanks to higher-order modulation and polarization multiplexing at the same component bandwidth, albeit at the cost of optical signal-to-noise ratio (OSNR) [32].

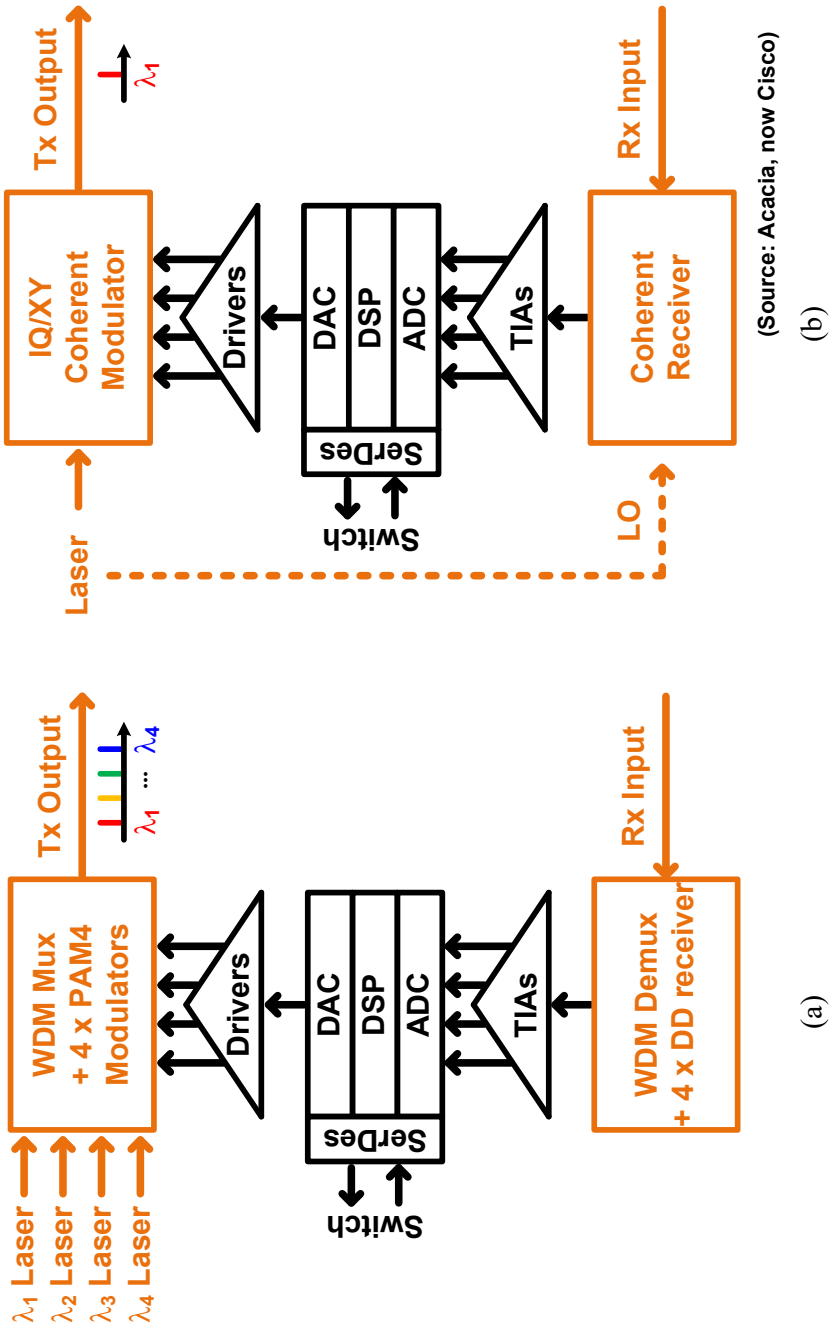

Fig. 1-11. Proposed 800G solution transceiver structure for (a) intensity modulation / direct detection (IM/DD), (b) coherent modulation [33].

Fig. 1-11 illustrates the structures of a commercial IM/DD transceiver and a coherent transceiver proposed for an 800G solution to scale the data capacity [33]. The IM/DD transceiver in Fig. 1-11(a) has been based on a wavelength division multiplexing (WDM) scheme to increase data aggregate along with the baud rate of the system raised. The data aggregate has been increased by using one to four or eight wavelengths. For this, WDM multiplexers (Mux) and demultiplexers (Demux) have been included as essential components, and each lane includes lasers, 200-Gbps (100-Gbaud) PAM4 modulators, DD receivers, driver electronics and trans-impedance amplifiers (TIAs) in the transceivers. Additionally, the analog-to-digital or digital-to-analog converters (ADC/DAC), DSP block and serializer/de-serializer (SerDes) perform specific functions necessary for the operation of the transceiver. However, increasing the number of wavelengths in IM/DD transceivers has eventually raised costs for lane-specific components and pushed wavelength deviations further away from the zero-dispersion range.

The coherent transceiver in Fig. 1-11(b), on the other hand, uses a single wavelength to achieve capacity scaling through polarization multiplexing (X/Y-polarization) and higher-order modulation (16QAM). The transceiver consists of a coherent IQ/XY modulator and a coherent

receiver, and it also includes sub-blocks such as driver, TIA, DSP, DAC and ADC. Compared to IM/DD, coherent transceivers have the advantages of reduced hardware costs for lasers and less concern about wavelength allocation.

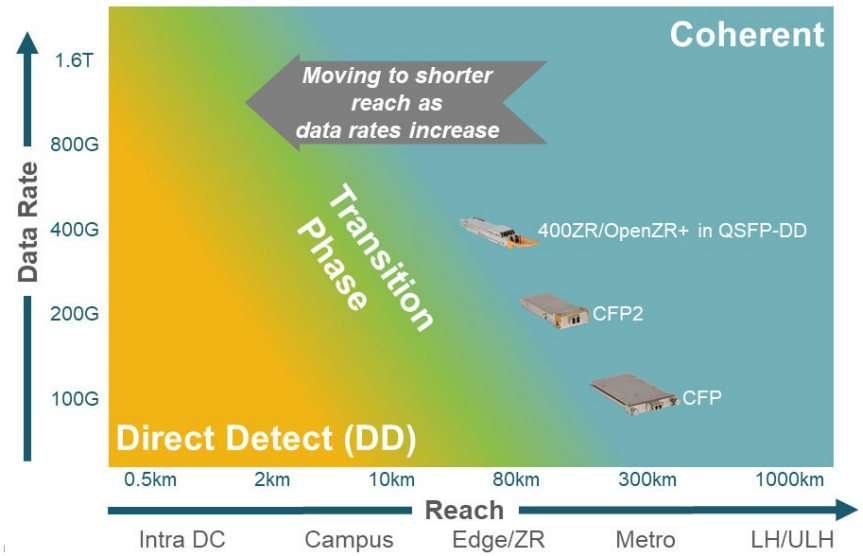

Fig. 1-12. Modulation formats for required transmission distances and data rates. Coherent optical transceiver moving toward short reach as data rates increase [33].

Fig. 1-12 shows the transition phase of modulation formats corresponding to distance (reach) and data rate. Currently, IM/DD link dominates short-reach DCI where the cost and power are inevitable consideration factors thanks to its advantages of simpler modulator and

receiver structure and lower DSP power consumption [6], [10,11], [30], [34]. However, as data rate requirements increase, IM/DD links may not guarantee the required performance due to such problems as an optical multipath interference [35] and a SNR limitation [29]. Consequently, coherent links, which have been primarily used for long-haul (LH) and metro applications where performance and robustness of hardware take priority over cost, are expected to approach short-reach DCIs.

Furthermore, DSP functions, which are essential in LH and metro applications, can be simplified for short-reach DCI because chromatic dispersion (CD) and polarization mode dispersion (PMD) are less critical factors in the short-reach transmission. The implementation of low-power, high-capacity coherent transceivers for short-reach DCI, referred to as "Coherent-Lite" [30], [33], [36], is expected, leveraging simplified coherent receivers, e.g., Kramers-Kronig receivers [37] and Stokes vector receivers [38] or simplified DSP front, e.g., optical phase-locked loop (OPLL) [39] and all-analog equalization [40]. In addition, numerous optical transceiver manufacturers attempt to achieve low-cost, low-power, and high-volume production through CPO-based coherent optical transceivers and switching networks, which align with the global trend in optical DCI [41,42].

1.4. Research Goals

As described above, with the ever-increasing demand for data traffic, broader and more extensive applications of coherent transceivers are expected, and high integration density, high transmission capacity and low power consumption are required for coherent transmitters and receivers as well. Mach-Zehnder IQ modulators, mainly implemented in the conventional coherent transmitters, have a large device footprint, making them inadequate to meet the compactness significant for future DCI applications. In this regard, this study targets to integrate Si photonic coherent IQ modulators with Si ring modulators (RMs) based on ring resonators, offering high compactness, integrity and energy efficiency. Fig. 1-13 illustrates the structure of a coherent transmitter based on a ring-modulator-assisted Mach-Zehnder interferometer (RaMZI). The optical input is split into each arm of MZI, and single-quadrature RMs are integrated into each arm of MZI to operate as I-channel and Q-channel, respectively. The signals are then combined with a 90-degree phase shift using the integrated optical hybrid, eventually generating the IQ modulated signals.

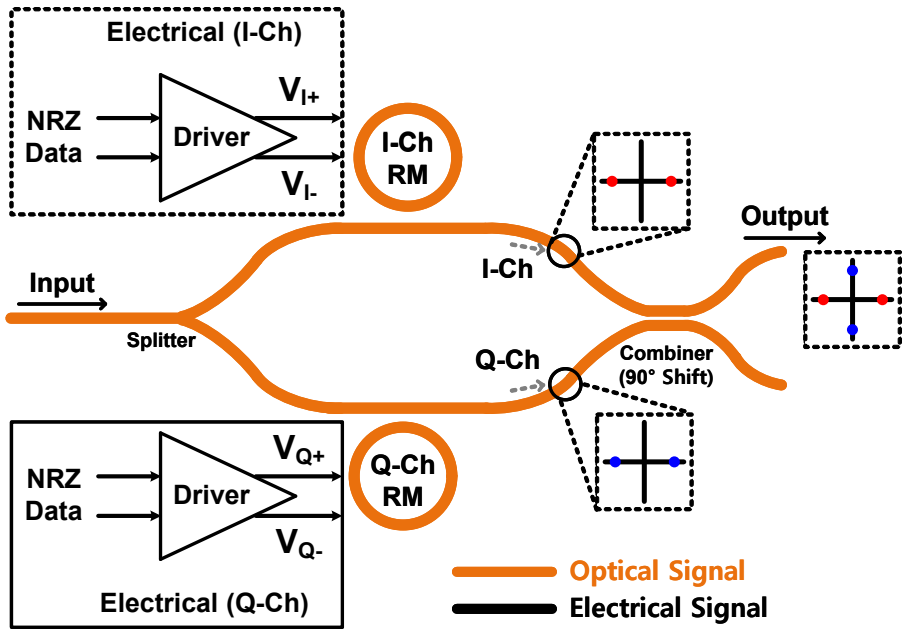

Fig. 1-13. Schematic of proposed coherent transmitter based on ring modulators.

The operation of Si photonic IQ modulators requires driver electronics capable of providing high driving voltages and data rates. Through IHP's Si photonic BiCMOS process [22], which allows the co-integration of high-performance SiGe hetero-bipolar transistors (HBT) and CMOS electronics as well as photonic integrated circuits as in Fig. 1-14, the Si photonic BiCMOS coherent QPSK transmitter based on RMs is realized as monolithic Si electronic-photonic integrated circuits (EPICs). For this, the device characteristics of RMs, including insertion loss, driving voltage, intensity and phase modulation behavior, are characterized and optimized for the implementation of highly efficient

and highly compact coherent transmitters. In addition, the performance of the realized Si photonic BiCMOS coherent transmitter is evaluated with a coherent receiver implemented within same photonic BiCMOS process for a 28-Gbaud QPSK signal and a single polarization, confirming the potential of coherent EPIC transceiver sub-assembly for emerging and increasing applications of coherent optical modulation.

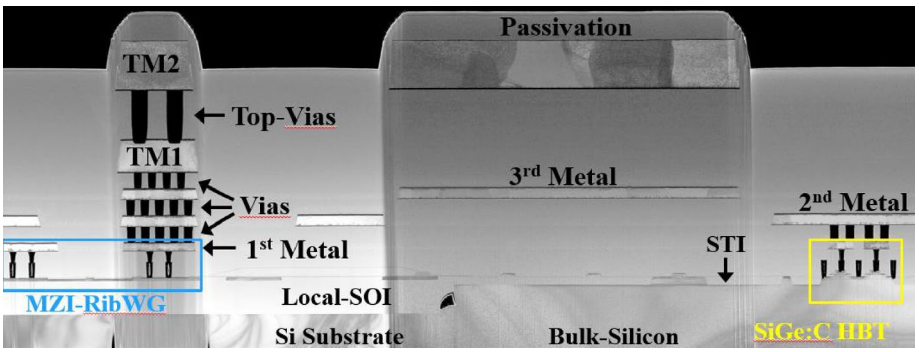

(a)

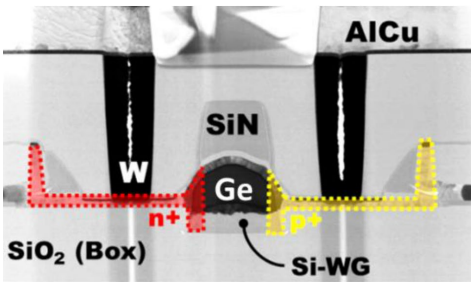

(b)

Fig. 1-14. IHP's Si photonic BiCMOS process: cross-sectional micro photo of (a) entire process, (b) Ge-on-Si photodiode [22].

1.5. Outline of the Dissertation

This dissertation is focused on the realization of the monolithic Si coherent transmitter EPIC with ring modulators (RMs) through the co-integration of photonic components and driver electronics. The primary contribution of this research comes from the compact device footprint and high energy efficiency of RMs. To achieve this, the modulation characteristics of RMs are comprehensively investigated and optimized as an individual single-quadrature modulator. Then, descriptions of entire structure of monolithic coherent transmitter as well as the RM driver electronics for desired driving voltage and data rate are given. Furthermore, the performance measurements of the transmitter with the coherent receiver fabricated within the same photonic BiCMOS process are introduced. To have a better performance of coherent modulator based on the RM, further investigation on optimization is carried out.

Chapter 2 of the dissertation gives the overview of the Si optical modulators. Characteristics of various modulators such as Mach-Zehnder modulators (MZMs), ring modulators (RMs), electro-absorption modulators (EAMs), MOS-capacitor-based modulators and thermal modulators are introduced. Especially, the advantages of RMs which are essential building blocks of this research to realize the

coherent transmitter are explained.

Chapter 3 describes the fundamental operation principle of the RMs based on a round-trip theory (RTT) and a coupled-mode theory (CMT). In addition, the electrical characteristics of the RMs are introduced. The modulation linearity of RMs is investigated to verify the CMT-based time-domain to frequency-domain numerical analysis technique, to understand the linear operation point (input wavelength and power for RMs) and to explore the possibility of expanding the RM-based higher-order coherent modulation format, which requires a high modulation linearity.

Chapter 4 introduces the device structure and optical and electronic components of the Si photonic BiCMOS coherent transmitter as well as the optimized results of the RMs for phase modulation. For this, the modulation frequency responses of the single-quadrature RMs is characterized based on the CMT-based model described in Chapter 3. The phase modulation performance optimization of the RMs is given in terms of dynamic insertion loss, V_{π}, 3-dB modulation bandwidth and Q factor. The BiCMOS RM driver electronic circuit is explained, and the post-layout simulated results are given.

Chapter 5 gives the measured results of the fabricated coherent transmitter EPIC based on the RMs, which is evaluated with the

coherent receiver EPIC realized within same photonic BiCMOS process. Due to process variation of the coherent IQ modulators, the alignment technique of the resonances of two RMs and the phase mismatch compensation of Mach-Zehnder interferometer (MZI) are explained. The receiver EPIC is briefly introduced, and the measurement setups are described. The measured bit-error rate, constellation and re-sampled eye diagram are shown, which confirms the successful operation for 25-Gbaud and 28-Gbaud QPSK signals based on all-silicon monolithic coherent transceiver sub-assembly realized with the RMs.

Chapter 6 provides simulation results with a wider model parameter range and an improved modulation efficiency assumed to achieve improved coherent modulators/transmitters based on the RMs. With these, the single RM for single-quadrature modulator is analyzed to obtain enhanced phase-modulation performance within the trade-off relationship among their performance metrics, dynamic insertion loss, V_{π}, 3-dB modulation bandwidth and Q factor. Then, an exploration of an alternative driving scheme, such as the push-pull configuration and architecture, is explained, followed by an analysis of the resulting performance.

Finally, Chapter 7 concludes the dissertation.

2. Si Optical Modulators

Optical modulators are devices that convert physical properties of optical signals, such as intensity and phase, based on given input data. For example, to put it simply, an optical modulator is a device capable of converting given bit patterns, typically denoting 0s and 1s, into corresponding electric field (E-field) patterns. Criteria for high-performance modulators include easily distinguishable output signals according to input data, the ability for fast transmission within a short data period, low loss of the signal, low power consumption and a small device footprint [8].

There are two primary methods for optical modulation: direct modulation of the laser and external modulation through an optical modulator. Direct modulation with lasers is an inefficient way because of the performance dependence on the structure of lasers. In addition, Si's indirect bandgap leads to difficulties in achieving highly efficient lasers in Si. Therefore, optical modulation in Si PIC often requires external Si optical modulators [21], [23,24]. Si is transparent at telecommunication wavelengths of 1550 nm (C-band) and 1310 nm (O-band) and allows the low-loss implementation of passive components such as waveguides thanks to the high index contrast with SiO_2 [7],

[21-24]. However, pure silicon exhibits relatively weak E-field-based E/O effects, e.g., Pockels, Kerr, and Franz-Keldysh effects, compared to compound semiconductor materials such as lithium niobate and III-V materials. Consequently, implementing the modulator based on pure Si's E/O effects results in highly inefficient modulation characteristics.

To solve this issue, the approach involves implanting impurities such as boron and phosphorus into Si to form diode structure. These diodes induce depletion, accumulation or absorption of free carriers, and finally, the optical absorption and refraction properties are changed by the free-carrier effects for the given input signal. This approach is known as a free-carrier-effects-based Si optical modulator. Representative examples of such optical modulators include Mach-Zehnder modulators (MZMs), electro-absorption modulators (EAMs) and ring modulators (RMs). Over time, the performance of these multi-physics-involved optical modulators has improved by engineering better utilization of free-carrier effects [8] and optimizing the structures of the modulators [10,11], [21], [23,24], [31]. To provide a basis for better understanding of Si photonic coherent transmitters, this chapter briefly introduces Si optical modulators such as MZM and EAM, as well as the RM.

2.1. Si Mach-Zehnder Modulators (MZMs)

Mach-Zehnder modulators (MZMs) are commonly used optical modulators in various applications of modulators and transmitters. Many foundries provide Si MZMs as a part of PDKs in Si photonic MPW services [21,24], also allowing further optimization of Si MZMs within the design diversity of the process. For fiber-optic communications, MZMs have been usually implemented using lithium niobate (LN) materials [43], and MZMs with LN-on-Si for high-speed and highly linear operation have also been reported [44]. In addition, there are continuous efforts for MZMs using III-V semiconductors with improved the E/O effect [45].

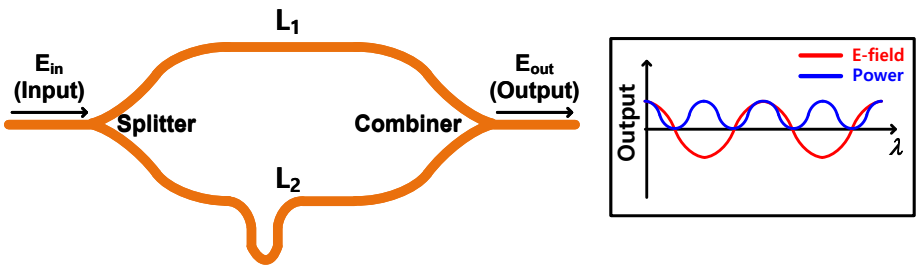

Fig. 2-1. Schematic of Mach-Zehnder interferometer (MZI) and its transmission characteristic.

Fig. 2-1 shows the structure of the Mach-Zehnder interferometer (MZI) which is fundamental block of Mach-Zehnder modulators. The input optical signal is split into two waveguides, each with a length of L_1 and L_2, propagating through each arm and then recombined into a single optical signal. The combined E-field can have a phase difference due to the different lengths of the two arms, resulting in an interference pattern in the output optical spectrum as shown in the inset of Fig. 2-1. Assuming no propagation loss in waveguides, the relationship between the input and output optical E-fields is given as [46]

$$\frac{E_{out}}{E_{in}} = \frac{1}{\sqrt{2}}\left(\exp(-j\frac{2\pi}{\lambda} n_{eff,upper} L_1) + \exp(-j\frac{2\pi}{\lambda} n_{eff,lower} L_2) \right). \quad (2.1)$$

In Eq. (2.1), $n_{eff,upper}$ and $n_{eff,lower}$ represent the effective refractive indices of the upper and lower arm of the MZI, respectively. L_1 and L_2 represent the path lengths of each arm. The transmission (T) of the MZI's output and input can be calculated from Eq. (2.1) is given as

$$T = \frac{P_{out}}{P_{\text{in}}} = \frac{1}{2}\left(1 + \cos(\frac{2\pi}{\lambda}\Delta(n_{eff} L)) \right), \quad (2.2)$$

$$\Delta n_{eff} L = n_{eff,upper} L_1 - n_{eff,lower} L_2 . \quad (2.3)$$

The MZI has cosine-dependent transmission in terms of wavelength for the given value of $\Delta n_{eff}L$, as in Eq. (2.2). Both the output E-field and the output power with cosine dependence can be observed in the inset of Fig. 2-1. The MZMs can modulate optical signals by changing the $\Delta n_{eff}L$ value through E/O effects, either in a single arm or both arms of the MZI, based on the applied voltage (E-field). LN materials have significant refractive index change with the applied voltage, which allows sufficient optical modulation based solely on the $\Delta n_{eff}L$ change which direct modulation of LN material such as Pockels effect provides [43]. In contrast, pure Si-based MZMs, with its limited change of the optical properties from the applied E-field, can result in the insufficient performance from their direct modulation.

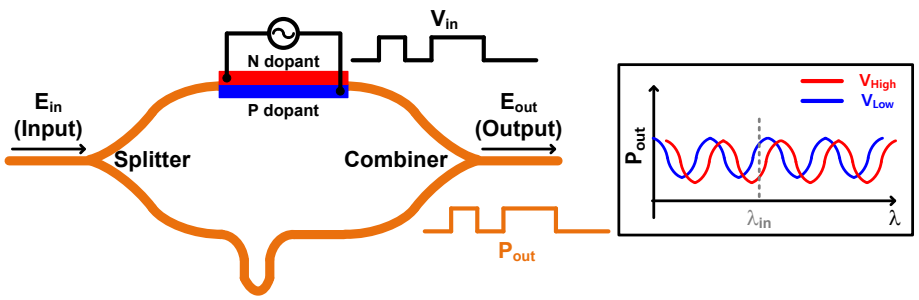

Fig. 2-2. Schematic of Mach-Zehnder modulator (MZM) based on MZI and p-n diode and its transmission characteristic for different applied voltages.

To solve this issue, the carriers are implanted into a single arm (or both arms) of the MZI, and various types of diodes such as p-n or p-i-n can be realized. The carrier distribution in the junction is changed as the voltage (V_{in}) is applied, and consequently, these free carriers induce the change in the optical absorption coefficient and refractive index, known as free-carrier plasma dispersion effects [47]. These types of Si optical modulators are known as free-carrier-effects-based Si optical modulators [8], and these modulators based on $\Delta n_{eff}L$ enable relatively more sufficient modulation than the pure silicon modulators do.

$$\Delta\alpha\ [\mathrm{cm}^{-1}] = 8.88\times10^{-21}\Delta N^{1.167} + 5.84\times10^{-20}\Delta P^{1.109}, \qquad (2.4)$$

$$-\Delta n = 5.40\times10^{-22}\Delta N^{1.011} + 1.53\times10^{-18}\Delta P^{0.838}. \qquad (2.5)$$

Eq. (2.4) and (2.5) respectively represent changes in the optical absorption coefficient ($\Delta\alpha$) in cm^{-1} and refractive index (Δn) of bulk Si in terms of changes in free carrier concentration, ΔP for free holes and ΔN for free electrons both units are given cm^{-3} [47]. As can be seen in the inset of Fig. 2-2, the MZI experiences the shift of its transmission characteristics as different voltages applied (V_{high} and V_{low}), and at the input optical wavelength (λ_{in}), the optical signal can be modulated, based on the change of optical properties in Eq. (2.4) and (2.5).

The performance metrics of MZMs, optical path length difference (L) and the voltage required to achieve a π-phase shift (V_π), have a trade-off relationship. In depletion-type MZMs, if L is reduced to decrease the device footprint, a larger voltage is required to obtain a π-phase shift, resulting in an increased V_π, and the opposite is also true. The value of $V_\pi L$ achievable for Si MZMs in Si photonics depends on the process conditions of each foundry service which cannot be easily accessible and controllable. Therefore, to operate the Si MZMs within a few volts, modulation efficiency must be increased, which requires the integration of diode regions into a few millimeters, eventually leading to an entire device footprint of several square millimeters [11], [21], [24].

Moreover, the voltage applied from the electrode exhibits microwave electrode characteristics at high frequencies, so careful and precise radio frequency (RF) design including impedance matching, group velocity matching, etc., has a great importance. The E/O modulation characteristics of MZMs is greatly influenced by the electrical characteristics of traveling-wave electrodes [48,49]. Also, the modulation linearity of Si MZMs shows lower modulation linearity performance [50] due to their inherent cosine dependent transmission and nonlinear diode characteristics for free carrier effects, compared to

LN-based MZMs.

Si MZIs/MZMs have been frequently used in Si photonic optical switches, filters, modulators and transmitters. To overcome the performance limitations of Si MZMs in current Si photonic processes, the research based on hybrid integration of Si with III-V semiconductor materials [45] or the material properties engineering such as strain and stress [51] to enhance the plasma dispersion effect has been reported.

However, due to the device footprint, travelling-wave electrode characteristics and modulation linearity, the Si MZMs will not be a suitable solution for future applications, especially in Si photonic coherent IQ modulators and CPO-based coherent transceivers, which are expected to be a big trend for wider and broader transmission distances of coherent transceivers.

2.2. Electro-Absorption Modulators (EAMs)

Another approach to optical modulators is electro-absorption modulators (EAMs) which modulate optical signals by changing the optical absorption coefficients. EAMs enable low-power, high-speed optical modulation by inducing significant variations in output optical power based on the applied voltage. These modulators are being developed with the Si photonic processes and hybrid integration approaches.

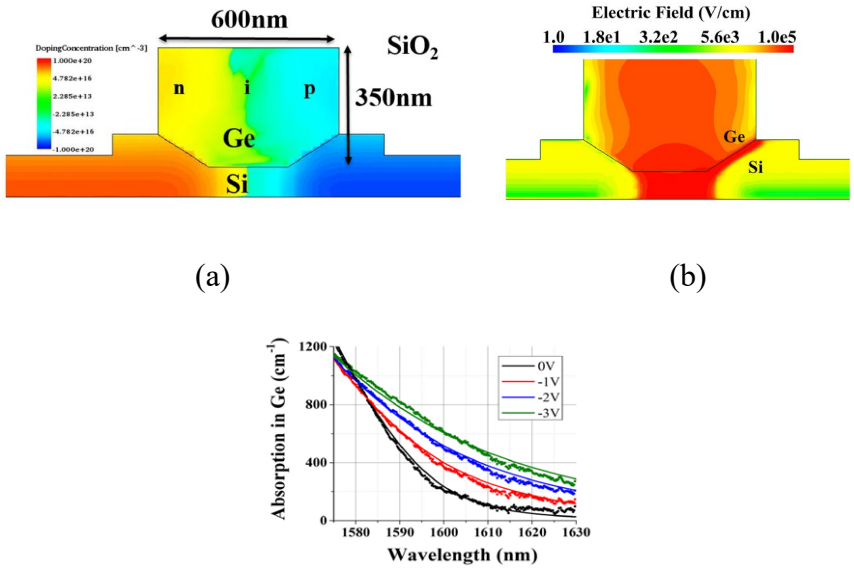

Fig. 2-3. Ge-on-Si electro-absorption modulator (EAM): (a) Ge-on-Si's cross-section and doping concentration, (b) E-field distribution at -2V and (c) absorption coefficient of Ge for different bias voltages [52].

Fig. 2-3 shows the integrated Ge-on-Si EAMs using the strong Franz-Keldysh effect within Si photonic platform with a 130-nm CMOS toolset [52]. Fig. 2-3(a) illustrates the cross-section and doping concentration of Ge on a 220-nm SOI waveguide and a lateral p-i-n diode as well. Fig. 2-3(b) shows the distribution of the E-field when -2 V voltage is applied. The reported Ge EAMs, thanks to the significant change in Ge absorption coefficients around 1610-nm wavelength as shown in Fig. 2-3(c), demonstrated high energy efficiency of 12.8 fJ/bit with a 2 $V_{peak\text{-}to\text{-}peak}$ driving voltage in 56-Gb/s NRZ-OOK operation, consuming approximately 1.2 mW. In addition, the sub-picosecond speed characteristics of the Franz-Keldysh effect resulted in a reported 3-dB E/O modulation bandwidth exceeding 50 GHz.

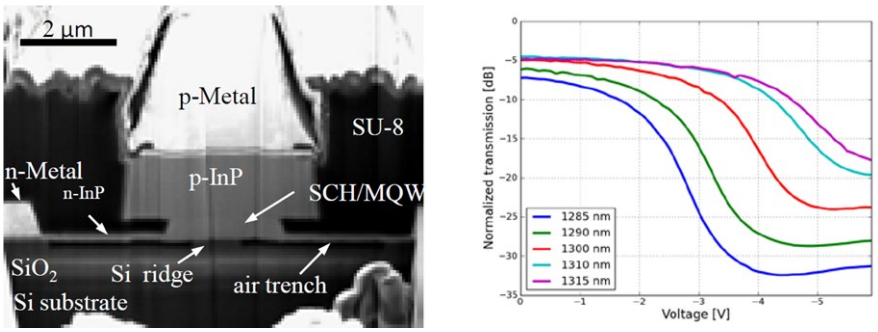

(a) (b)

Fig. 2-4. Hybrid Si optical EAM based on III-V epitaxy stacks on SOI: (a) cross-section of proposed structure and (b) normalized transmission in terms of applied voltages and wavelengths [53].

Hybrid Si optical EAMs based on the transfer of III-V epitaxy stacks onto SOI has also been reported [53]. Fig. 2-4(a) shows the cross-section of InGaAs multiple quantum wells (MQW), which enables the tuning of the optical absorption coefficient using the quantum-confined Stark effect (QCSE). Fig. 2-4(b) shows changes in optical transmission around 1310-nm wavelength based on applied voltage, influenced by MQW-based QCSE. The 3-dB E/O modulation bandwidth of EAMs is mainly influenced by microwave electrodes. Therefore, E/O bandwidth exceeding 67 GHz is achieved by the careful and precise co-planar waveguide (CPW) design. Successful 50-Gb/s NRZ-OOK operation with a dynamic extinction ratio of 9.6 dB using a 2.2 $V_{peak\text{-}to\text{-}peak}$ driving voltage has been reported [53].

EAMs have the powerful capability to produce high-performance optical modulators with some additional fabrication process steps which lead to additional costs. However, since the EAMs depend on optical absorption coefficients for their operation, they are not suitable modulators as a coherent IQ modulator that requires the sufficient phase modulation [21].

2.3. MOS-Capacitor and Thermal Modulators

There are alternative approaches to optical modulators such as MOS-capacitor based modulators and thermal modulators.

MOS-capacitor modulators exploits carrier accumulation in a MOS-capacitor structure for the change of optical properties, replacing the weak plasma dispersion effect. A MOS-capacitor modulator composed of p-type poly-Si, gate-oxide and n-type SOI demonstrated 28-Gbps NRZ-OOK operation with a 1 $V_{peak\text{-}to\text{-}peak}$ driving voltage, achieving a 9-dB extinction ratio and $V_\pi L$ < 0.2 V.cm [54]. Furthermore, InGaAsP/Si hybrid MOS optical modulators by direct wafer bonding demonstrated successful 53-Gbaud PAM4 operation with a 13.8-dB outer extinction ratio and 0.047-V.cm $V_\pi L$ [55]. However, the MOS-capacitor-based optical modulators require the additional fabrication complexity to create a vertical structure consisting of metal-oxide-semiconductor region for the operation [54,55].

Thermal modulators, on the other hand, utilize the Si's refractive index change with respect to temperature through a thermo-optic phase shifter in a standard SOI process. A thermal modulator with a 61.6-μm length phase shifter has been reported with 130 kHz of 3-dB modulation bandwidth and 24.77 mW of P_π [56]. Thermal modulators

are not suitable modulator candidate for high-speed optical coherent IQ modulators due to the a few microseconds speed of thermo-optic response [56].

2.4. Si Ring Modulators

Among Si optical modulators, Si ring modulators (RMs) based on the ring resonator offer many advantages such as a small device footprint, large modulation bandwidth for depletion-type and high energy efficiency. The Si RMs have shown their potential to be integrated into hyperscale DCI IM/DD transceivers such as 256-Gb/s PAM4 modulator due to a high modulation bandwidth of the depletion-type RMs, along with hybrid-integrated III-V lasers [57].

Fig. 2-5 shows example device size comparison between Si RMs and Si MZMs [58]. The Si RMs are micrometer-scale devices composed of a small resonant cavity and routing waveguide, unlike Si MZMs with a millimeter-scale long p-n diode region and traveling-wave electrode. Thanks to small device footprint and high energy efficiency, the Si RMs are promising solutions for CPO-based hyperscale DCI due to the required high integration density and low power consumption [11].

Researches on integrating the RMs as key building blocks for coherent IQ modulators were reported a decade ago [59,60]. However, several limitations such as modulation characteristics dependence on input wavelength, high driving voltage, modulation nonlinearity,

optical power handling, thermal sensitivity and fabrication process variations have been identified.

Efficient implementation of coherent IQ modulators/transmitters based on the RMs requires accurate analysis and characterization of the aforementioned phenomena. The modulation characteristics of RMs depending on the operation wavelength have been modeled using small-signal and large-signal SPICE equivalent circuits [61,62] and Verilog-A model [63]. Self-heating effects due to optical power handling [64,65], and modulation nonlinearity [66] have also been characterized. Thermal sensitivity of RMs has been solved by real-time monitor and controller using a monolithically integrated temperature controller electronics [67,68] and process variations can be predicted accurately in the design stage through SPICE-based Monte-Carlo simulation techniques [69].

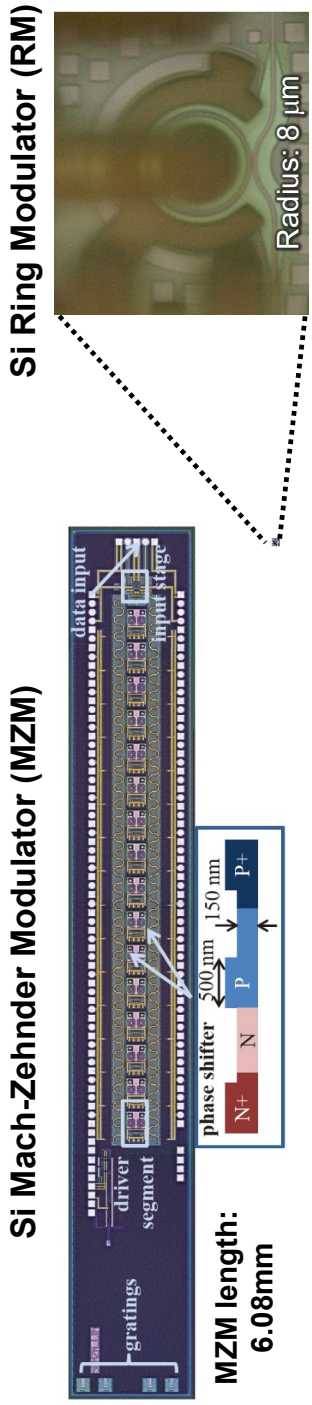

Fig. 2-5. Device footprint comparison of Si MZM [58] and Si RM.

2.5. Summary

Si optical modulators are essential devices for the applications of Si PIC for fiber-optic communication, but the pure Si's weak electro-optic effects have been overcome by implantation of dopants or hybrid integration with other semiconductor materials for better modulation efficiency. The MZMs are commonly used but have large device footprint or high driving voltages. The EAMs offer low-power, high-speed modulation by changing optical absorption coefficients, and the MOS-capacitor and the thermal modulators are also alternative approaches, but the EAMs and MOS-capacitor modulators cost additional fabrication steps and the thermal modulators have insufficient modulation bandwidth.

The Si RMs with their small device footprint and high efficiency provide a promising solution for coherent IQ modulators. However, the RMs have several drawbacks such as wavelength-dependent modulation characteristics, nonlinearity, optical power handling, thermal sensitivity and fabrication process variations. Accurate analysis and characterization are crucial for an efficient integration of the RMs into coherent IQ modulators/transmitters. For this, detailed modeling and characterization of Si RMs will be discussed.

3. Characterization of Si Ring Modulators

3.1. Operation Principle: Round-Trip Theory

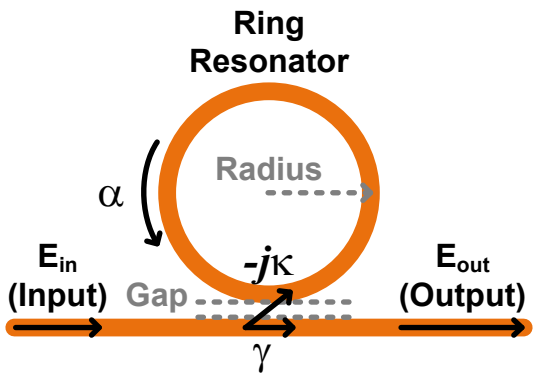

Fig. 3-1. Structure of ring resonator.

Fig. 3-1 shows the fundamental structure of Si ring resonator (RR) which is a base structure for the ring modulators (RMs). It consists of a ring waveguide as a resonant cavity and a bus waveguide as a routing waveguide for the optical signal. In the figure, α represents the remaining field ratio after a round trip, and γ represents the through coefficient in the directional coupler region. The field ratio of cross-coupling between the bus waveguide and the ring waveguide is given as κ, and in the figure, $-j\kappa$ implies a 90-degree ($\pi/2$) phase shift for a cross-coupling. The relation between γ and κ is given as $\gamma^2 + \kappa^2 = 1$,

and E_{in} and E_{out} represent the input and output E-fields, respectively. For a given waveguide width and height, α is mainly determined by the propagation loss and bending loss based on the radius of the ring waveguide, while γ and κ are mainly determined by the gap between the ring and bus waveguides.

The transmission characteristics of Si RRs are determined by two key parameters, α and γ, and can be explained from the round-trip theory (RTT) [70]. E_{out} can be expressed as a sum of (i) the component passing through the bus waveguide as γE_{in} and (ii) the component that is cross-coupled into the ring, travels inside the ring and then cross-coupled back to the bus waveguide. Because the light traveling in the ring waveguide keeps circulating before it becomes completely disappears, the cross-coupled components can be mathematically expressed as an infinite sum with the passing through components as,

$$\begin{aligned} E_{out} &= \gamma E_{in} - (\alpha e^{-j\phi})\kappa^2 E_{in} - (\alpha e^{-j\phi})^2 \gamma \kappa^2 E_{in} - (\alpha e^{-j\phi})^3 \gamma^2 \kappa^2 E_{in} - \cdots \\ &= \gamma E_{in} - \kappa^2 \sum_{n=1}^{\infty} \alpha^n \gamma^{n-1} e^{-n\phi} E_{in} \end{aligned} . \quad (3.1)$$

From Eq. (3.1), the relation between E_{in} and E_{out} can be expressed as

$$\frac{E_{out}}{E_{in}} = \frac{\gamma - \alpha e^{-j\phi}}{1 - \alpha\gamma e^{-j\phi}} . \quad (3.2)$$

From Eq. (3.2), transmission (T), the relation between input and output optical power, can be expressed as

$$T = \left| \frac{E_{out}}{E_{in}} \right|^2 = \frac{\alpha^2 - 2\alpha\gamma\cos(\phi) + \gamma^2}{1 - 2\alpha\gamma\cos(\phi) + (\alpha\gamma)^2}, \tag{3.3}$$

where $\phi = 2\pi n_{eff} L/\lambda$, and L is the circumference of the ring waveguide and n_{eff} is the effective refractive index at the resonance wavelength. The Si RR shows the resonance behavior when the terms inside the Σ in Eq. (3.1) which denote the field traveling inside the ring accumulate with the in-phase condition (integer multiples of 2π). Due to twice of cross-coupling, a 180-degree (π) phase shift occurs, resulting in notch filter characteristics at the resonance wavelength. The resonance condition can be derived from this in-phase condition as

$$m\lambda_{res} = n_{eff} L, \tag{3.4}$$

where m is an integer denoting the mode number, and λ_{res} is the resonance wavelength.

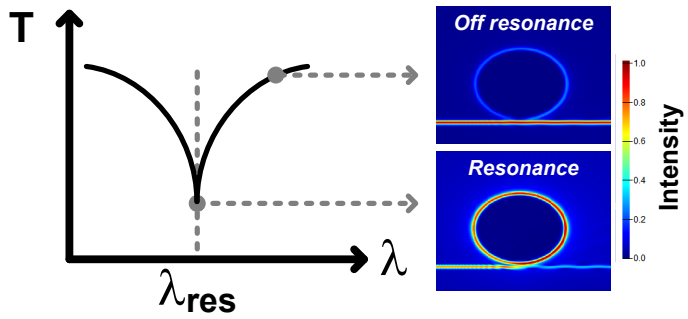

(a)

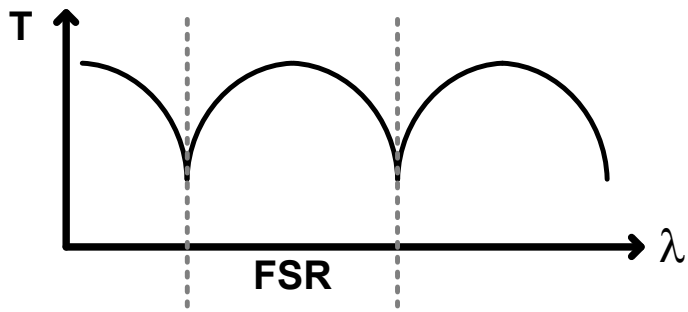

(b)

Fig. 3-2. (a) Transmission spectrum of RR and field distribution at resonance wavelength and at off-resonance wavelength, (b) broadband transmission spectrum of RR.

Fig. 3-2(a) presents the transmission spectrum of the RR that can be calculated using Eq. (3.3). In the inset of the figure, the field profiles at λ_{res} (resonance) and far point from λ_{res} (off-resonance) are given by simulation using Ansys Lumerical FDTD. At the resonance, a significant accumulation of field intensity is observed inside the ring

due to the in-phase condition, while a small field intensity is observed at the output because the 180-degree phase shift causes a reduction of output power. In contrast, at the off resonance, a smaller field intensity is observed inside the ring, while a larger output field intensity is observed at the output.

As Eq. (3.4) implies, the Fig. 3-2(b) shows the repetitive resonances of the Si RRs for the corresponding integer mode number *m*. The spacing between these repetitive resonances is referred to as the free-spectral range (FSR), given as,

$$FSR = \frac{\lambda^2}{n_g L}, \tag{3.5}$$

where n_g represents the group index of the RR. Moreover, the quality factor (*Q*-factor), which denotes a ratio of energy stored in the ring to energy loss of the ring due to round trip and cross-coupling and indicates a sharpness of the notch, is given as follows.

$$Q = \frac{\pi n_g L \sqrt{\gamma\alpha}}{\lambda_{res}(1-\gamma\alpha)}. \tag{3.6}$$

Due to the notch filter characteristics resulting from the resonance, the Si RRs are implemented as filters required in various systems such as optical receivers [71] and optical WDM receivers [72].

For the modulation operation of Si RMs, dopants are implanted into the circumference of the ring to form a lateral p-n diode, as shown in Fig. 3-3(a). By applying a voltage (V_{in}) through electrical pads and interconnects, the carrier concentration changes, inducing the free-carrier plasma dispersion effect which changes the absorption coefficient and refractive index of the optical mode, and finally the output optical power changes corresponding to V_{in}. Fig. 3-3(b) illustrates the structure of the lateral p-n diode implemented in the ring.

All the RMs in this dissertation are fabricated by IHP's Si photonics/photonic BiCMOS technology. The Si waveguide has a rib waveguide structure with 500-nm width, 220-nm thickness and 100-nm slab thickness. Nominal peak carrier concentrations for p-region and n-region are 7 x 10^{17} cm^{-3} and 3 x 10^{18} cm^{-3}, respectively. Silicon oxide (SiO_2) lies below the Si waveguide as a 2-μm buried oxide (BOX) and also exists above the Si waveguide, and N+ and P+ dopants and metal layers are used for ohmic contacts to apply the electrical signal. Unless specified otherwise, the waveguide geometry such as waveguide width, thickness and slab thickness and nominal peak carrier concentrations

are consistent in the latter description about the RMs.

Fig. 3-3(c) and (d) show the p-n diode and optical mode overlap when the reverse bias voltages, V_{low} and V_{high}, are applied. Optical mode has been calculated by Ansys Lumerical Finite Differential Eigenmode solver with the carrier distribution of the p-n diode calculated from device simulation by Ansys Lumerical CHARGE solver. When a reverse bias of V_{in} is increased from V_{low} to V_{high}, the depletion width (W_D) of the p-n diode increases. This change of carrier concentration induces the plasma dispersion effect, changing the absorption coefficient and refractive index of the overlapped optical mode, as described in Eq. (2.4) and (2.5). This also means that the parameters, α and n_{eff}, used to describe the Si RR varies, leading to the red shift of λ_{res} from Eq. (3.4). Thus, the transmission of the Si RM moves as voltage applied, allowing the modulation of the optical signal at the given operation wavelength (λ_{in}), as shown in Fig. 3-3(e). To describe the λ_{in} relative to the λ_{res}, detuning (D_ω) is defined as how much the angular frequency of the input light is detuned from the resonant angular frequency, $D_\omega = |\omega_{in} - \omega_{res}|$. Similarly, a wavelength detuning is given as $D_\lambda = |\lambda_{in} - \lambda_{res}|$.

Besides the lateral p-n diodes, various diode structures such as lateral p-i-n diodes [73] and L-shaped p-n diodes [74] can be

implemented in the circumference of the ring. The p-i-n diode, operating as a carrier injection type in the forward bias region, provides a greater plasma dispersion effect compared to the reverse-bias depletion-type p-n diode, resulting in a high modulation depth even with low driving voltage. However, p-i-n diodes have a smaller modulation bandwidth due to carrier lifetime limitations, making the modulator have insufficient bandwidth for high-speed operation. Furthermore, L-shaped p-n diodes, optimized so that overlap between carrier concentration change and optical mode is maximized, exhibit higher modulation efficiency than lateral p-n diodes but introduce additional fabrication complexity which cannot be easily implemented in the standard Si PIC foundry.

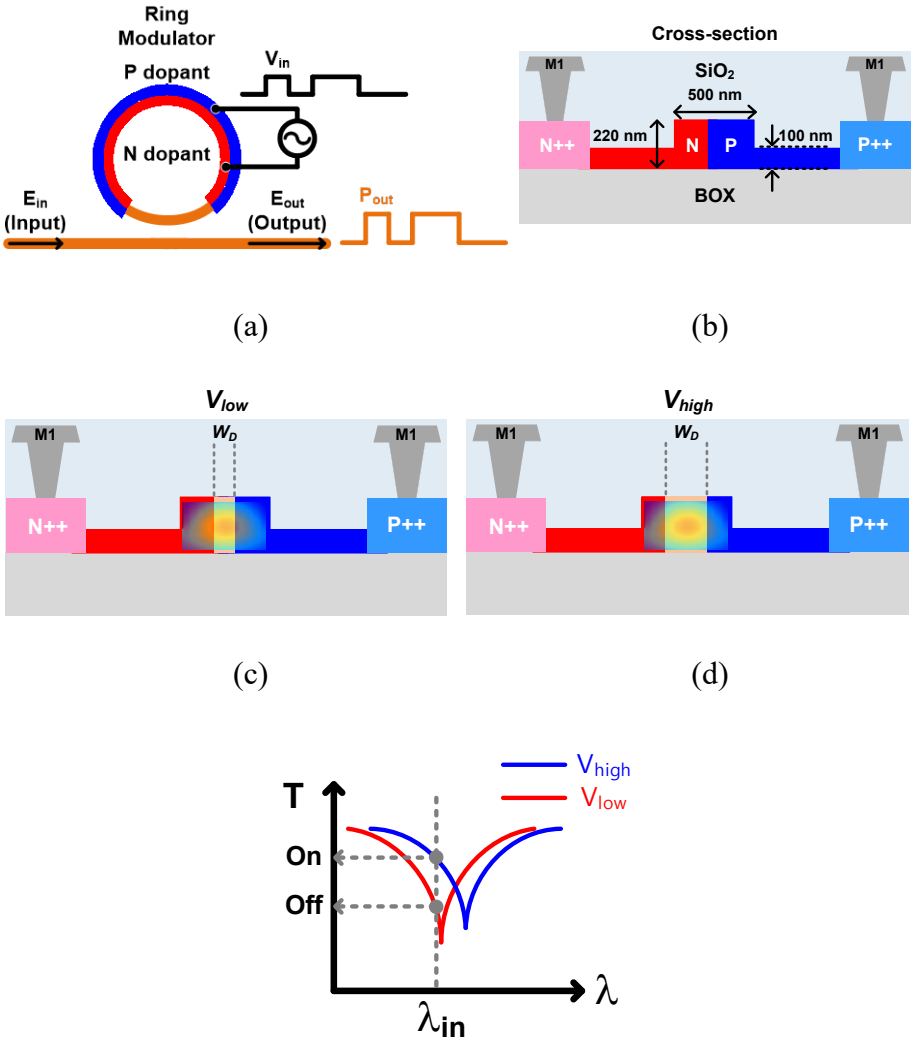

Fig. 3-3. (a) A lateral p-n diode in Si ring modulator, (b) cross-section of the diode. Overlapped optical mode for (c) V_{low} and (d) V_{high}. (e) Transmission spectra for different bias voltages.

3.2. Operation Principle: Coupled-Mode Theory

In the previous chapter, the Si RMs are described by the round-trip theory (RTT). However, the RTT requires the integral of series term in Eq. (3.2) with respect to time in order to describe the time-domain behavior of the RMs, which demands a numerical complexity. To compactly model the lossy resonant cavity of RMs with a reduced number of parameters in the time domain, the coupled-mode theory (CMT) can be used [63], [75]. The time-domain behavior of the RM can be expressed as follows.

$$\frac{d}{dt}a(t) = (j\omega_{res} - \frac{1}{\tau})a(t) - j\mu E_{in}(t), \tag{3.7}$$

$$E_{out}(t) = E_{in}(t) - j\mu a(t). \tag{3.8}$$

In Eq. (3.7), $a(t)$ represents the energy amplitude traveling in the ring waveguide, and τ is the decay time constant of the energy amplitude. ω_{res} is calculated as $2\pi mc/n_{eff}L$, given by Eq (3.4), where c denotes the speed of light in a vacuum. The total decay time constant, τ, is determined as

$$\frac{1}{\tau} = \frac{1}{\tau_l} + \frac{1}{\tau_e}, \tag{3.9}$$

where τ_l represents the decay time constant for the round-trip loss in the ring, and τ_e represents the decay time constant for the cross-coupling loss between the ring and bus waveguides. In Eq. (3.7) and (3.8), μ is the mutual coupling coefficient between the ring and bus waveguides, given as $\mu^2 = 2/\tau_e$.

Eq. (3.7) implies that the derivative of $a(t)$ with respect to the time consists of three components: (i) the resonant component of $a(t)$ with $j\omega_{res}$, (ii) the decaying component of $a(t)$ due to the round-trip and cross-coupling loss of the ring with $-1/\tau$, and (iii) the cross-coupled component of E_{in} to the ring with $-j\mu$. In addition, Eq. (3.8) implies that E_{out} consists of two components: (i) the through-coupled component of E_{in} and (ii) the cross-coupled component of $a(t)$ with $-j\mu$. Once the optical parameters from CMT model are determined, the time-domain modulation characteristics of the RMs can be described by numerically solving Eq. (3.7) and (3.8) when the RM is modulated with any kind of time-domain signal. For example, the time-domain behavioral model for RMs has been developed in Verilog-A [63], and large-signal equivalent circuit for RMs has been developed in SPICE [62], to simulate the time-domain response within standard IC tools.

With the steady-state assumption, $da(t)/dt = j\omega a(t)$, the transmission characteristic of the RM as in Eq. (3.3) is given as,

$$T = \left|\frac{E_{out}}{E_{in}}\right|^2 = \left|\frac{j(\omega-\omega_{res})+\frac{1}{\tau_l}-\frac{1}{\tau_e}}{j(\omega-\omega_{res})+\frac{1}{\tau_l}+\frac{1}{\tau_e}}\right|^2 . \tag{3.10}$$

The CMT parameters, τ_l and τ_e, representing RM's loss due to the ring waveguide and cross-coupling loss, respectively, have the following relationship with RTT parameters, α and γ which are discussed in the previous chapter:

$$\tau_l = \frac{2n_{eff}L}{(1-\alpha^2)c},\ \tau_e = \frac{2n_{eff}L}{(1-\gamma^2)c}. \tag{3.11}$$

Using governing equation of CMT, Eq. (3.7) and (3.8), as well as the refractive index perturbation method due to applied voltage (dn_{eff}/dV_j), the small-signal electro-optic (E/O) frequency response of RMs in the s-domain is given as follows [61].

$$\Delta_o(s) = \frac{P_{out} / P_{in}(s)}{V_j(s)} = \frac{4}{n_{eff}} \cdot \frac{dn_{eff}}{dV_j} \cdot \frac{\omega_{res} D_\omega / \tau_e}{D_\omega{}^2 + 1/\tau^2} \cdot \frac{s + 2/\tau_l}{s^2 + (2/\tau)s + D_\omega{}^2 + 1/\tau^2} \cdot \quad (3.12)$$

In Eq. (3.12), Δ_o represents the small-signal E/O response, and V_j and P_{out}/P_{in} refer to the voltage applied to the RM's p-n diode and the optical transmission, respectively. As shown in Eq. (3.12), the RM is a 2-pole, 1-zero system, and the relative positions of the pole and zero are determined by the values of model parameters τ_l and τ_e, as well as the value of D_ω. This implies that the modulation frequency of the RMs varies with geometry parameters such as the radius and coupling gap and operation condition such as input wavelength (λ_{in}) [61,62], and also suggests opportunities for optimization in terms of the RM's structure and operational conditions [64], [66].

3.3. RMs for phase modulation

To realize coherent IQ modulators/transmitters based on RMs, the fundamental operation and characteristics of phase modulated RMs are introduced. As in Fig. 1-13, the proposed QPSK modulator/transmitter consists of two single-quadrature RMs into each arm of the RaMZI structure, so the requirements for the single-quadrature RMs are the same intensity represented by insertion loss (IL) and a π-phase shift with a certain value of applied voltage called V_π.

A single RM exhibits three types of coupling depending on the coupling strength between the ring waveguide and the bus waveguide [70]. Fig. 3-4 shows the transmission and phase spectra based on the types of coupling that RMs can have. In the case of over-coupled RMs ($\tau_l > \tau_e$ or $\alpha > \gamma$), the RM shows 2π-phase shift around the resonance, and the required π-phase shift and the same intensity for phase modulation can be obtained with a certain value of the V_π. For critical-coupled RMs ($\tau_l = \tau_e$ or $\alpha = \gamma$), the RM shows more abrupt 2π-phase shift around the resonance than over-coupled RMs, enabling the π-phase shift with a lower V_π. However, due to a high Q factor of the critical-coupled RMs, the minimum of transmission is smaller than the over-coupled RMs, leading to higher IL at the operation point. Under-

coupled RMs ($\tau_l < \tau_e$ or $\alpha < \gamma$), on the other hand, do not have a 2π-phase shift around the resonance. Therefore, the under-coupled RMs are not appropriate candidates for a single-quadrature RM in the proposed structure in Fig. 1-13.

Fig. 3-5 illustrates the transmission spectra of the RM when bias voltages V_{low}, V_{dc} and V_{high} are applied with corresponding resonance wavelengths, λ_{low}, λ_{dc} and λ_{high}, respectively. Here, $V_{high} - V_{low}$ equals to V_π, and V_{dc} equals to $(V_{high} + V_{low})/2$. The RM achieves π-phase modulation at the wavelength where the two transmissions for V_{low} and V_{high} intersect, and this wavelength is the operation wavelength (λ_{in}). When the high-speed modulation signal is applied, the dynamic IL at λ_{in} can be determined at the intersection wavelength, λ_{in}. When only DC electrical signal is applied, the DC IL can be found in the transmission for V_{dc} at λ_{in}.

Due to the nonlinearity of RM model parameters [66], τ_l, τ_e and n_{eff}, in terms of bias voltage, λ_{in} and λ_{dc} are not exactly same. However, the difference between λ_{in} and λ_{dc} is extremely small, e.g., with $D\lambda$ being within a few picometers. This implies that the frequency response of phase modulated RMs cannot be accurately modeled using Eq. (3.12). There are two reasons for this: (i) both $D\omega$ and $D\lambda$ have the values close to zero, resulting in Eq. (3.12) approaching zero, and (ii) Eq. (3.12)

describes the response of transmitted power for intensity modulated RMs. As a result, it is necessary to develop and characterize a suitable model for the frequency response of phase modulated RMs in order to optimize the device performance of RMs for coherent IQ modulators.

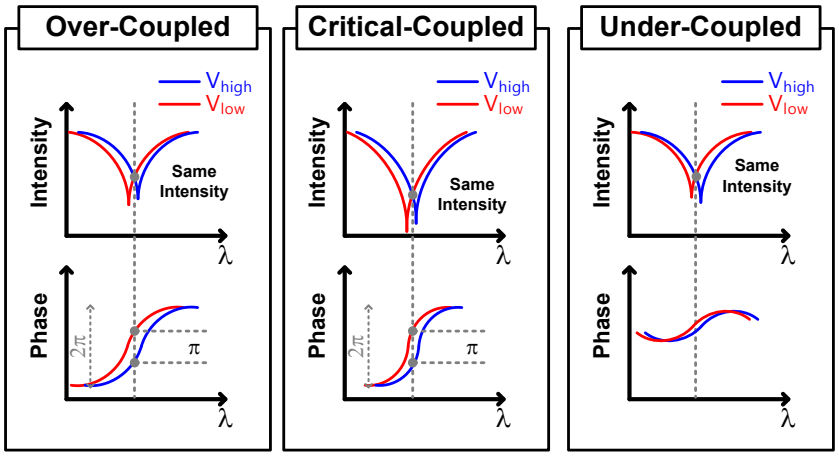

Fig. 3-4. Types of coupling of Si RMs.

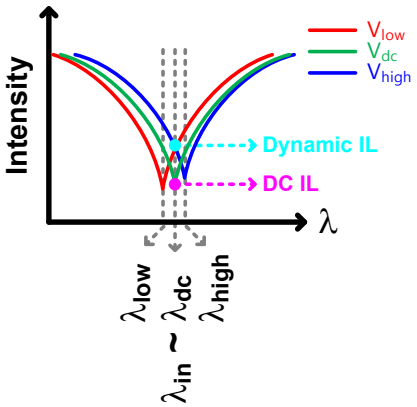

Fig. 3-5. Transmission spectra of the phase-modulated RM for V_{low}, V_{dc} and V_{high} and operation wavelength (λ_{in}).

3.4. Electrical Characteristics of RMs

In addition to the CMT model which characterizes the modulation properties of RMs such as Eq. (3.7) - (3.12), the entire electro-optic modulation characteristics are influenced by the electrical components of metal interconnects and the p-n diode of the RMs. Therefore, it is crucial to consider the electrical characteristics of RMs for the precise characterization of RMs in phase modulation applications.

Fig. 3-6(a) depicts the cross-section of the p-n diode composed of the series resistance for p-region (R_P) and n-region (R_N) and junction capacitance (C_j). The total series resistance of the diode is given as R_s, the sum of R_P and R_N. Fig. 3-6(b) shows the equivalent circuit with lumped RLC elements for electrical part of RMs. In the frequency range in this research, the electrical components of RMs can be approximated as lumped electrical RLC elements [61,62]. The electrical components of RMs also consist of parasitic components due to the electrical pads and interconnects, but the analysis is primarily focused on the influence of R_s and C_j to account for RM's electrical RC bandwidth because parasitic components have a negligible impact on the overall response [62]. Furthermore, C_j is a bias-voltage-dependent parameter, affected by W_D (depletion width) and carrier concentration

in the p-n diode, while R_s is assumed to be bias-voltage-independent. The 3-dB RC bandwidth of RM is dominantly determined by both R_s and C_j values, and due to the bias-voltage dependency of C_j, the RC bandwidth also exhibits bias voltage dependency.

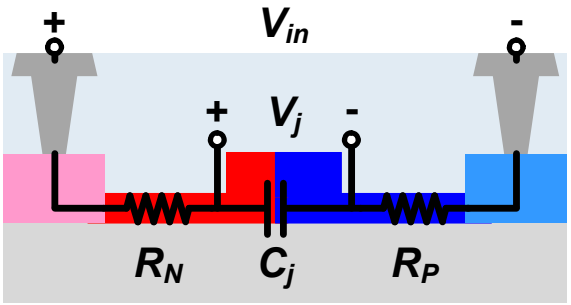

(a)

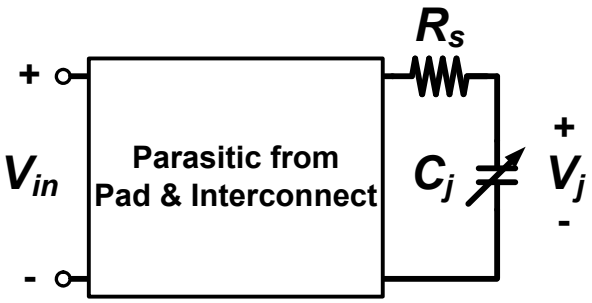

(b)

Fig. 3-6. (a) Electrical components of the p-n diode of RM, (b) equivalent circuit for electrical parts of RM.

3.5. Modulation Linearity of RMs [1]

The modulation linearity of the Si RMs is characterized using a CMT time-domain model [66]. The purposes of this investigation are (i) to verify the accuracy of the CMT model, (ii) to determine the most linear operation points of the RMs in terms of input optical wavelength (λ_{in}) and optical power (P_{in}) and (iii) to explore the potential of expanding the RM-based higher-order coherent modulation format such as QAM [59].

3.5.1 Parameter Extraction

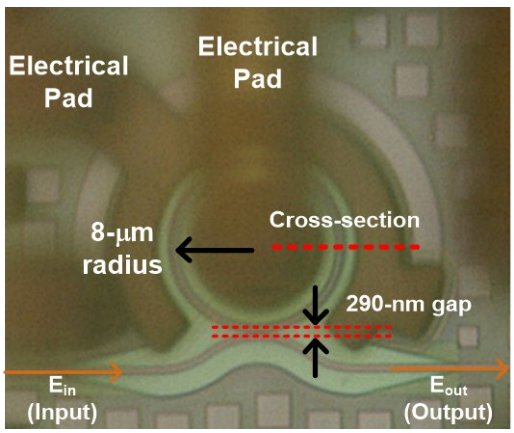

Fig. 3-7. Micro photograph of the RM for the investigation.

[1] © 2021 IEEE. Reprinted with permission from "Y. Jo *et al.*, Modulation Linearity Characterization of Si Ring Modulators, *Journal of Lightwave Technology*, Dec. 2021"

Fig. 3-7 presents a microphotograph of the RM, which has been used for the modulation linearity analysis, with an 8-μm radius and a 290-nm coupling gap. The CMT optical parameters described earlier are obtained from the optical transmission spectra measured at different reverse bias voltages, by numerically fitting the measured transmission to the steady-state transmission equation given as Eq. (3.10) using least root-mean-square fitting. Fig. 3-8(a) shows the measured and fitted transmission spectra, and Fig. 3-8(b) and (c) show the extracted parameter values of n_{eff}, τ_l and τ_e.

Furthermore, the electrical parameters, R_s and C_j, are obtained from the electrical reflection coefficient (S_{11}) measured at different reverse bias voltages, by fitting the measured S_{11} to the response of the equivalent circuit shown in Fig. 3-6 using least root-mean-square fitting. Fig. 3-9(a) and (b) show the measured and fitted magnitude and phase of S_{11} for the RM, respectively. Fig. 3-9(c) shows the bias-voltage-dependent parameter, C_j, with respect to reverse bias voltage. R_s is assumed to be bias-voltage-independent, and the extracted value of R_s is 240 ohms. The RM has been placed on a temperature-controlled stage whose temperature is maintained at 25°C for all measurements in Fig. 3-8 and 3-9.

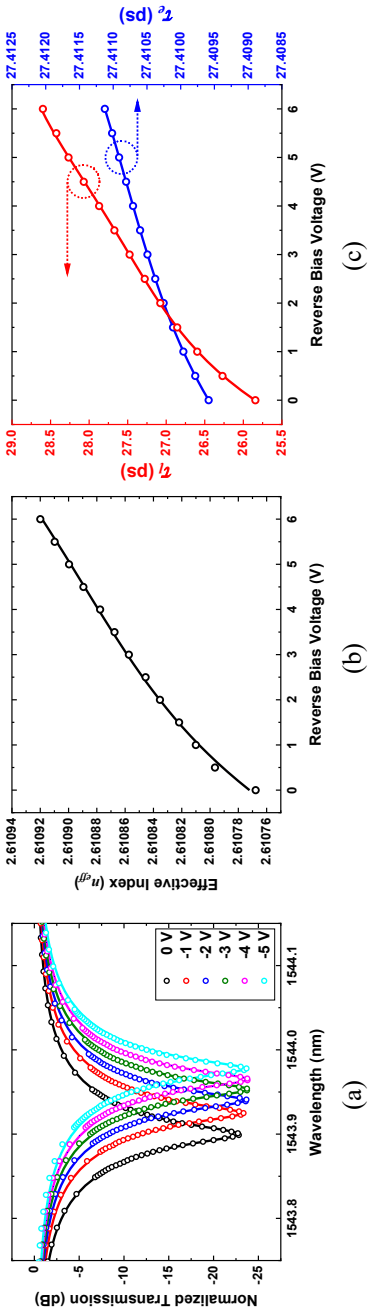

Fig. 3-8. (a) Measured and fitted optical transmission spectra when the RM is biased at different bias voltages, extracted values of (b) effective refractive index (n_{eff}) and (c) τ_l, τ_e.

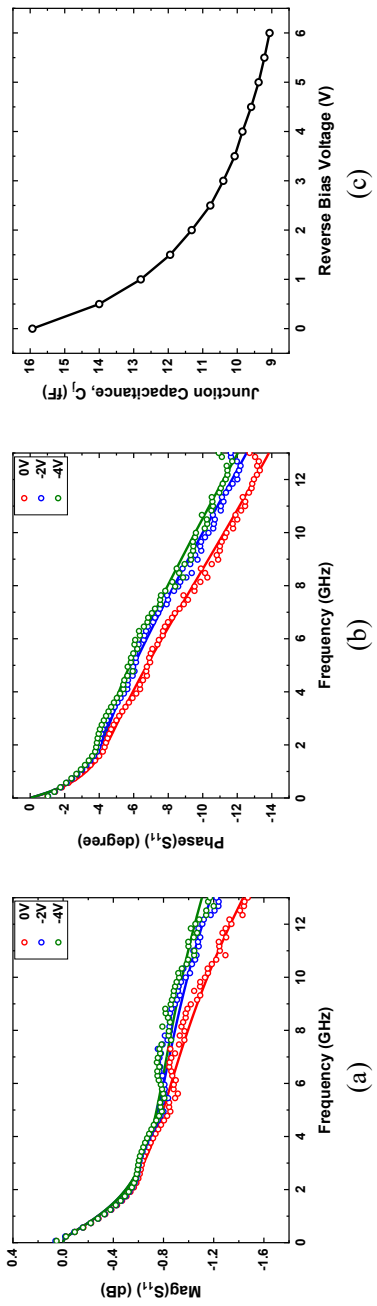

Fig. 3-9. Measured and fitted electrical reflection coefficient (S_{11}) when the RM is biased at different bias voltages: magnitude for (a) and phase for (b). Extracted values of C_j shown in (c).

3.5.2 Time-Domain to Frequency-Domain Analysis

Fig. 3-10 illustrates the block diagram for the modulation linearity modeling and simulation of the RM. To consider the influence of the RM's electrical components, the time-domain transient response between $V_{in}(t)$, the applied RF signal to the RM, and $V_j(t)$, the applied RF signal to the p-n diode is calculated from the equivalent circuit in Fig. 3-6 and the electrical parameters obtained from Fig. 3-9. The nonlinear capacitance, C_j, can be conveniently handled as a piecewise-linear voltage-controlled capacitor within Cadence Virtuoso. Then, the time-domain response of the RM, $E_{out}(t)$, can be simulated using the CMT model parameters obtained from Fig. 3-8 and the CMT model described in Eq. (3.7) and (3.8). By taking the fast Fourier transform (FFT) of the calculated $E_{out}(t)$, the modulation linearity in either the optical domain or electrical domain can be simulated.

For example, the magnitude of the Fourier transform of $E_{out}(t)$ represents the optical spectrum of the Si RM as $E_{out}(f)$. Fig. 3-11(a) shows the optical spectrum when the Si RM is modulated with 10-GHz RF signals at -2 V_{dc} bias voltage and a 2-$V_{peak\text{-}to\text{-}peak}$ amplitude. Here, λ_{in} is 40 pm smaller than λ_{res} for -2 V_{dc} bias voltage, as seen in the inset of Fig. 3-11(a). The optical spectrum in Fig. 3-11(a) also shows multiple

sideband peaks such as 1st-order lower sideband (LSB), 2nd-order LSB, 1st-order upper sideband (USB), and 2nd-order USB, separated by 10 GHz (80 pm) intervals. The background level can be attributed to truncation error resulting from FFT and simulation time step of $E_{out}(t)$.

Furthermore, the magnitude of the Fourier transform of $|E_{out}(t)|^2$ represents the electrical RF spectrum of the down-converted output signal through a photodetector (PD) as $I_{PD}(f)$. Fig. 3-11(b) shows the electrical RF spectrum when the Si RM is modulated with two-tone RF signals at -2 V_{dc} bias voltage, with frequencies of 9.9 GHz and 10.1 GHz, both having a 2-$V_{peak\text{-}to\text{-}peak}$ amplitude. The λ_{in} value is the same as in Fig. 3-11(a). In Fig. 3-11(b), two fundamental tone signals and third-order intermodulation distortion (IMD3) signals can be observed at 200 MHz intervals.

The 2nd-order (or higher-order) signals in Fig. 3-11(a) and the IMD3 signals in Fig. 3-11(b) are a result of the nonlinearity of the Si RM. By simulating the two-tone RF modulation analysis as in Fig. 3-11(b) for different RF powers, the performance metric of modulation linearity [16], [66], known as the spurious-free dynamic range (SFDR), can be determined.

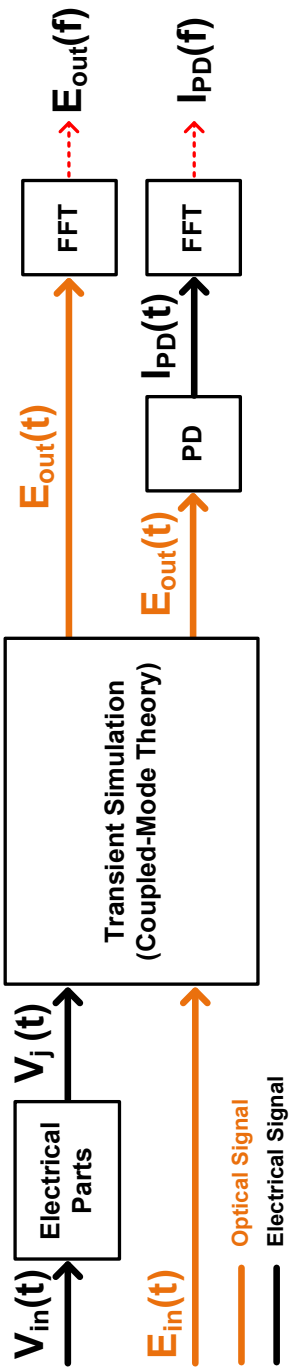

Fig. 3-10. Block diagram for modulation linearity characterization of RM.

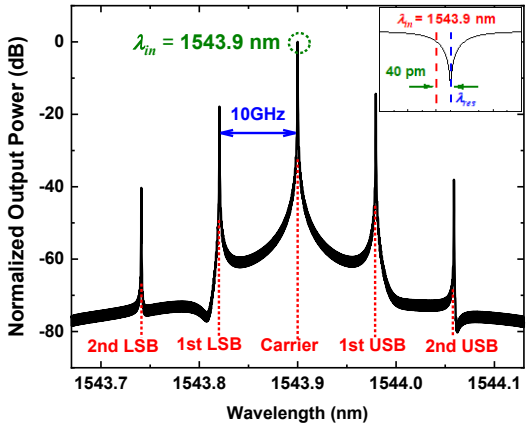

(a)

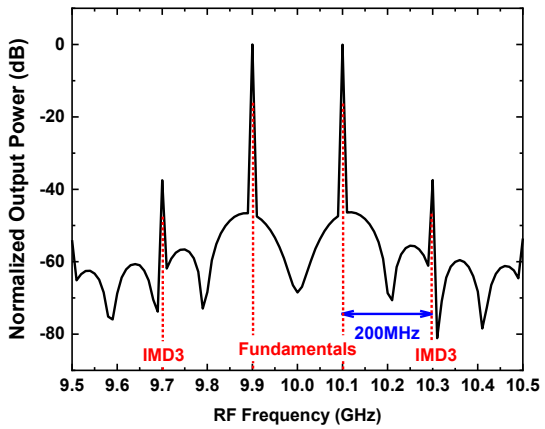

(b)

Fig. 3-11. (a) Simulated optical spectrum of the RM modulated with one-tone, 10-GHz RF signal and (b) simulated electrical RF spectrum of the RM modulated with two-tone, 9.9-GHz and 10.1-GHz RF signals. -2 V_{dc} of bias voltage and 1543.9 nm of λ_{in} are used for both cases, and the RF signal has 2-$V_{peak\text{-}to\text{-}peak}$ amplitude for both cases.

3.5.3 Self-Heating Effect

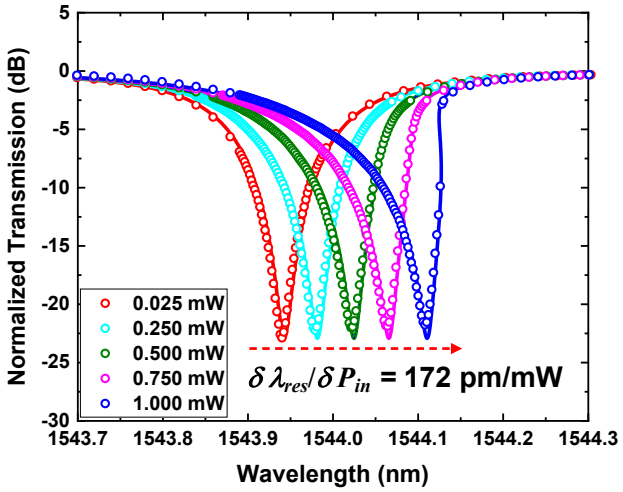

Fig. 3-12. Normalized transmission spectra measured at 5 different values of P_{in}, 0.025, 0.250, 0.500, 0.750 and 1.000 mW and extracted value of $\delta\lambda_{res}/\delta P_{in}$.

The Si RM shows asymmetric shift in transmission spectrum due to the self-heating effect with different values of P_{in} [64]. Fig. 3-12 shows normalized transmission spectra for five different P_{in} values, and the influence of the self-heating effect on transmission spectra is shown. λ_{res} linearly red shifts as P_{in} increases with 172 pm/mW of $\delta\lambda_{res}/\delta P_{in}$ which equals to 2.91 x 10^{-4} /mW of $\delta n_{eff}/\delta P_{in}$. $\delta n_{eff}/\delta P_{in}$ has two contributions: one from the increase due to self-heating and the other from the decrease due to dispersion. With the known values of

dispersion of Si and SiO_2 as well as the waveguide confinement factor, the amount of dispersion at the 1.55 μm wavelength of the given Si waveguide is calculated as -1.85 x 10^{-4} /mW [76]. From this, the purely self-heating-induced $\delta n_{eff}/\delta P_{in}$ can be decoupled as 4.76 x 10^{-4} /mW. As self-heating effect depends on the RM's Q factor, its influence on the modulation linearity performance is different in terms of model parameters as well as device geometry [64]. In addition, the Kerr effect and two-photon absorption effect in Si at 1.55 μm are 3–6 x 10^{-18} m^2/W [77,78] and 0.7 cm/GW [79], respectively, both of which can be considered negligible within the P_{in} range of this investigation.

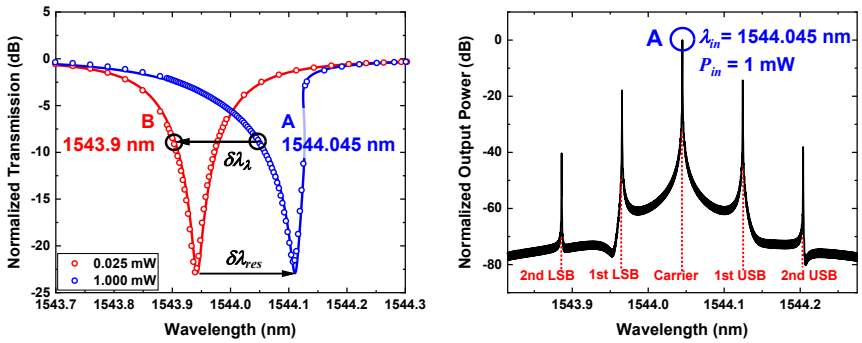

(a) (b)

Fig. 3-13. (a) Normalized transmission spectra for 0.025 mW and 1.000 mW of P_{in}. (b) optical spectrum of the RM for 10-GHz, 2-$V_{peak\text{-}to\text{-}peak}$ RF signal at point A.

The self-heating effect on RM causes an asymmetric shift in the transmission spectrum. The wavelength change due to the self-heating effect ($\delta\lambda_\lambda$) at any wavelengths near resonance can be numerically determined as

$$\delta\lambda_\lambda = \delta n_{eff} \frac{L}{m} \left| \frac{\frac{1}{\tau}}{j(\omega - \omega_{res}) + \frac{1}{\tau}} \right|^2 , \tag{3.13}$$

where δn_{eff} represents the difference in effective index at resonance for high and low P_{in} values, and τ, ω, and ω_{res} are values for low P_{in} value.

The self-heating effect only affects the steady-state characteristics of the RM but has no influence on dynamic modulation characteristics of RMs [66]. Therefore, the modulation linearity analysis with both λ_{in} and P_{in} considered under the self-heating effect can be performed based on the calculated modulation characteristics as in Fig. 3.10 with model parameters at low P_{in}, which means without the self-heating effect. For example, the blue curve in Fig. 3-13(a) represents the transmission spectrum at 1.000 mW of P_{in}, where point A corresponds to 1544.045 nm of λ_{in}. By substituting the model parameter values and δn_{eff} into Eq. (3.13), the amount of shift due to the self-heating effect can be

determined as 145 pm, and from this value, the λ_{in} without self-heating effect corresponding to point A is found as point B (1543.9 nm of λ_{in}) in the red curve of Fig. 3-13(a) which represents the transmission spectrum at 0.025 mW of P_{in}. In other words, the analysis of dynamic modulation characteristics of the RM at point A can be performed under the assumption that the calculated modulation characteristics without self-heating effect at the point B is shifted as much as the amount determined by Eq. (3.13). Furthermore, it's worth noting that modulation characteristics at the same normalized transmission points are identical. Fig. 3-13(b) shows the optical spectrum at point A obtained through this technique. Except for 145 pm of wavelength difference determined by Eq. (3.13), the optical spectrum is identical to that in Fig. 3-11(a) which corresponds to the point B in Fig. 3-13(a).

3.5.4 Measurement of Modulation Linearity of RMs

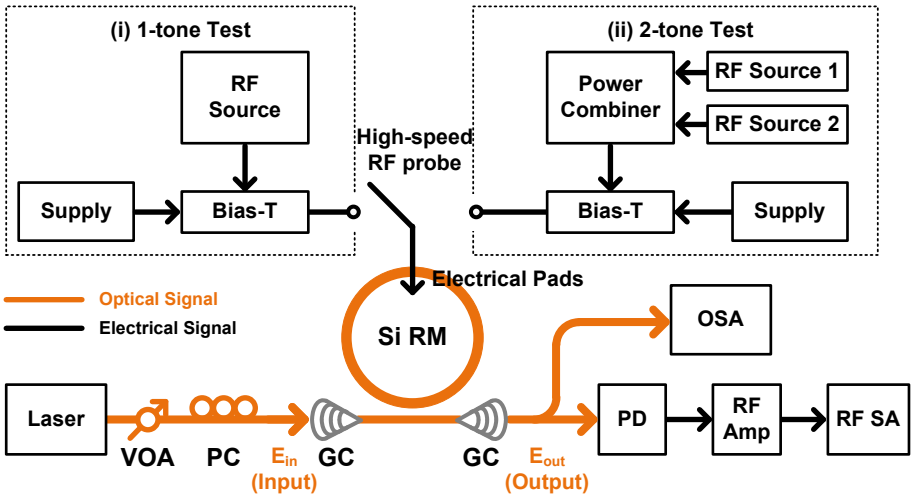

Fig. 3-14. Measurement setup for modulation linearity characterization of RMs.

Fig. 3-14 shows the measurement setup for RM's modulation linearity analysis. The optical signal is supplied to the RM from the tunable laser source (TLS), the variable optical attenuator (VOA) and the polarization controller (PC) through a pair of on-chip grating couplers (GCs) as an optical I/O. For the 1-tone measurement, the 10-GHz, 2 $V_{peak\text{-}to\text{-}peak}$ RF signal and the -2 V_{dc} bias voltage are supplied to the device through a bias-T. For the 2-tone measurement, 9.9-GHz and 10.1-GHz RF signals with 2 $V_{peak\text{-}to\text{-}peak}$ are power-combined and supplied to the device. An optical spectrum analyzer (OSA) is used to

obtain the optical spectrum as in Fig. 3-11(a), and the photodetector (PD), the RF amplifier (RF Amp) and the RF spectrum analyzer (RF SA) are used to obtain the RF spectrum as in Fig. 3-11(b).

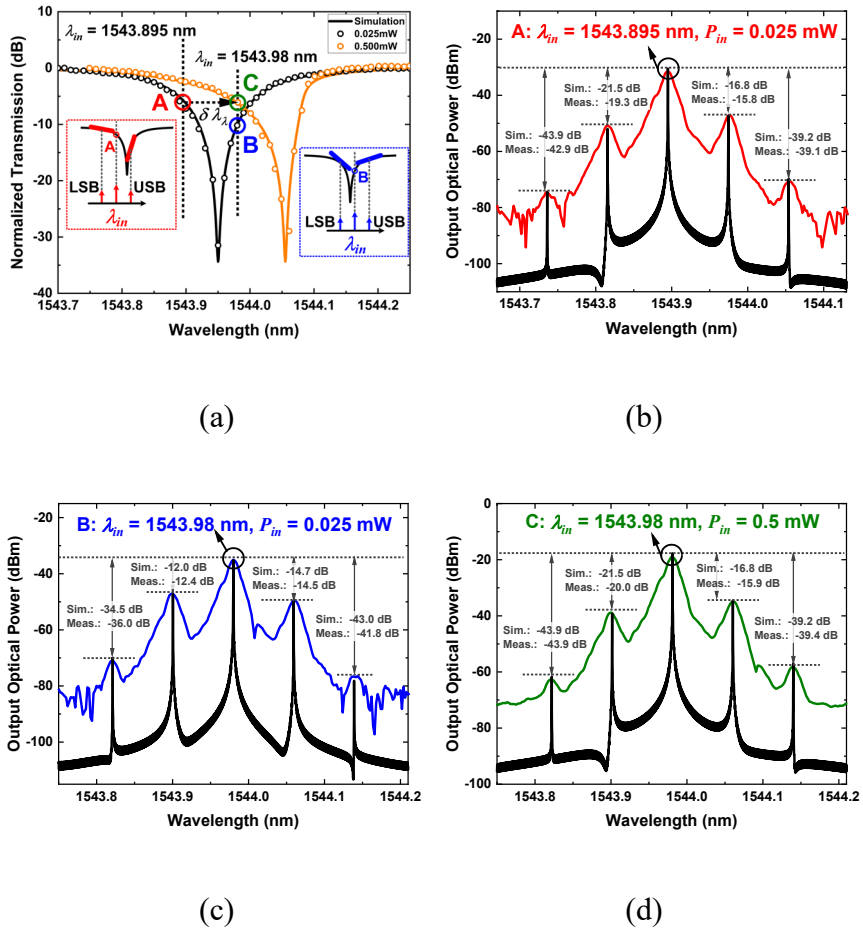

Fig. 3-15. (a) Normalized transmission spectra for 0.025 mW and 0.5 mW of P_{in}. Measured and simulated optical spectra when the RM is modulated with 10-GHz, $2V_{peak\text{-}to\text{-}peak}$ RF signal for (b) point A, (c) point B and (d) point C in (a).

Fig. 3-15(a) shows transmission spectra at 0.025 mW and 0.5 mW of P_{in} values, both of which are from Fig. 3-12, to describe the optical spectrum in terms of P_{in} and λ_{in} when Si RM is modulated with a 10-GHz, 2 $V_{peak\text{-}to\text{-}peak}$ RF signal. In cases such as the point A, where λ_{in} is smaller than λ_{res}, the LSB has a smaller slope magnitude in the transmission spectrum than that of the USB, resulting in a smaller peak optical power value for LSB. In contrast, at the point B, where λ_{in} is larger than λ_{res}, the LSB has a larger slope magnitude in the transmission spectrum than that of the USB, resulting in a larger peak optical power value for LSB. These opposing behaviors are graphically represented in the inset of Fig. 3-15(a).

Fig. 3-15(b), (c), and (d) respectively show the measured and simulated optical spectra for the point A (λ_{in} = 1543.895 nm, P_{in} = 0.025 mW), the point B (λ_{in} = 1543.98 nm, P_{in} = 0.025 mW) and the point C (λ_{in} = 1543.98 nm, P_{in} = 0.5 mW), as shown in Fig. 3-15(a). As explained in the previous chapter, the simulated optical spectrum for the point C, as shown in Fig. 3-15(d), can be obtained by shifting the simulated optical spectrum at the point A using Eq. (3.13) and model parameters measured at low P_{in}. The measured ratios of sideband peaks to the carrier in Fig. 3-15(b), (c) and (d) agree well with the simulation results, verifying the accuracy of the CMT-based numerical analysis of

the RM's modulation linearity and self-heating effect characterization technique, regardless of the value of λ_{in} and P_{in}. Furthermore, the description in Fig. 3-15(a) regarding the relation of relative slope magnitudes of the LSB and USB and corresponding peak optical powers can be observed in Fig. 3-15(b) with USB having a larger peak optical power at the point A and in Fig. 3-15(c) with LSB having a larger peak optical power at the point B.

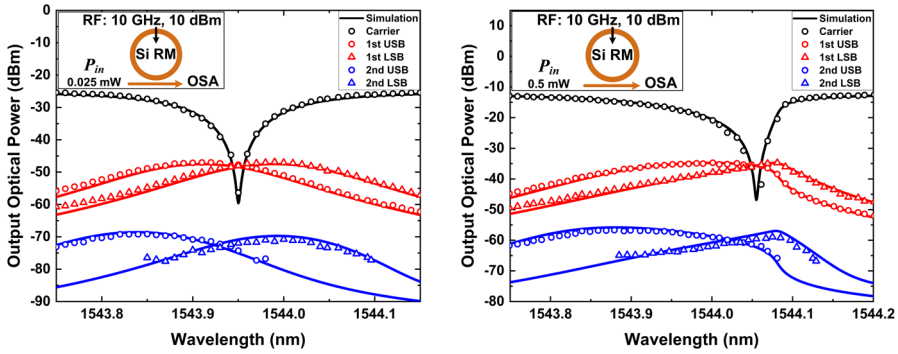

(a) (b)

Fig. 3-16. The measured and simulated peak optical powers of carrier, 1st-order and 2nd-order sidebands in terms of λ_{in} when the RM is modulated with 10-GHz, $2V_{peak\text{-}to\text{-}peak}$ RF signal for (a) 0.025 mW and (b) 0.5 mW of P_{in}.

Fig. 3-16(a) and (b) show the measured and simulated peak optical powers of the carrier, 1st-order and 2nd-order sidebands in terms of λ_{in},

for P_{in} values of 0.025 mW and 0.5 mW, respectively. It is evident that RM's modulation linearity is highly sensitive to the values of λ_{in} and P_{in}. The careful selection of these operating points is particularly crucial in applications involving linear modulation of the Si RMs because of the trade-off between maximizing the 1st-order signal and minimizing the 2nd-order signal, which makes achieving the optimum for both challenging, as demonstrated in Fig. 3-16.

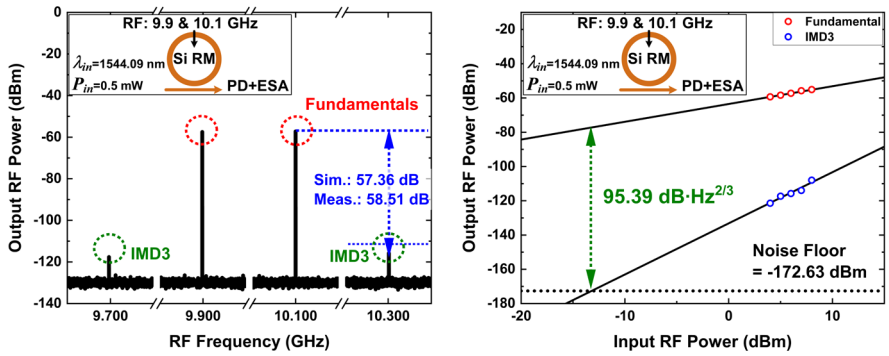

(a) (b)

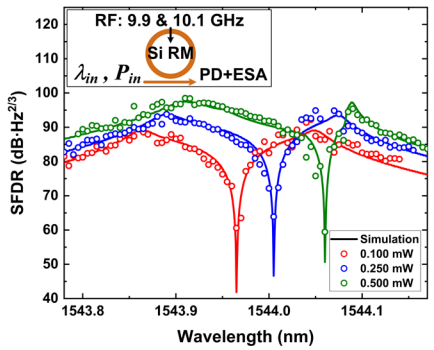

(c)

Fig. 3-17. (a) Measured RF spectrum of the RM modulated with 9.9-GHz, 10.1-GHz and 1.25 $V_{peak\text{-}to\text{-}peak}$ of RF signals at 1544.09 nm of λ_{in} and 0.5 mW of P_{in}. (b) Measured peak RF powers of fundamental and IMD3 signals with different input RF powers and SFDR value at the same point in (a). (c) Measured and simulated SFDR of the RM with different P_{in} of RM, 0.100, 0.250 and 0.500 mW.

For the measurement of RF spectrum, a sufficient RF power must be provided to the RF SA. A large P_{in} is supplied to the PD to increase

the output photocurrent, and the photocurrent is amplified through the RF amplifier to provide the detectable signal power to the RF SA. The PD and RF amplifier used in this investigation have a responsivity of 0.63 A/W and 1-dB gain compression power larger than 10 dBm, respectively. The values of P_{in} and the RF amplifier gain are carefully selected to ensure that the PD and the RF amplifier do not affect the modulation linearity measurement of the RM. Fig. 3-17(a) shows the RF spectrum when the Si RM is modulated by two-tone RF signals with 9.9 GHz and 10.1 GHz whose amplitude is 1.25 $V_{peak\text{-}to\text{-}peak}$. Here, P_{in} has a value of 0.5 mW, and λ_{in} is 1544.09 nm, which is 30 pm larger than λ_{res}. The measured ratio of the fundamental to the IMD3 is 58.51 dB, close to the simulated value of 57.36 dB.

For the characterization of SFDR, the peak RF powers of the fundamental and IMD3 signals are measured for different RF power values of two-tone signals. The measured are shown in Fig. 3-17(b), using the same values of P_{in} and λ_{in} as in Fig. 3-17(a). The SFDR represents the relative magnitude of the fundamentals, which can be guaranteed when the IMD3 signals are equal to the noise floor, so the noise of the entire measurement setup must be characterized. The contributions to the noise in the radio-over-fiber (RoF) link include relative intensity noise (RIN), shot noise and thermal noise [80]. First,

the RIN of the TLS is approximately -140 dB/Hz, and the load impedances for the PD and the RF amplifier are both 50 ohms. The bandwidth for noise calculation is assumed to be 1 Hz. In the link loss/gain calculation, the insertion loss of the Si RM for each λ_{in} is considered, along with the coupling loss due to a pair of GCs and waveguide loss. With an insertion loss due to waveguides and grating couplers of 14.4 dB, the optical power of the TLS is controlled with the VOA to deliver 0.5 mW of P_{in} to the RM. The insertion loss of the RM at the same P_{in} and λ_{in} as in Fig. 3-17(a) is 1.9 dB, resulting in an input power of -12.1 dBm delivered to the photodetector and leading to 0.039 mA of photocurrent. At this point, the shot noise and RIN noise are calculated as -182.11 dBm and -181.34 dBm, respectively, which is one order of magnitude smaller than the thermal noise of -173.85 dBm. Then, the noise floor is determined as -172.63 dBm, resulting in an SFDR of 95.39 dB·Hz$^{2/3}$. For cases where λ_{in} is closer to λ_{res}, the total noise is more dominated by thermal noise due to the increased insertion loss of the RM [81].

Fig. 3-17(c) presents the measured and simulated SFDR as a function of λ_{in} at three different P_{in} values. Due to the high insertion loss of the Si RM, the link noise is thermal noise limited, and the influence of P_{in} on the noise floor is negligible. Thus, as P_{in} increases,

the output power of the RM also increases, resulting in an increase in the SFDR. The asymmetric shift of the SFDR curve for large P_{in} values is also shown in Fig. 3-17(c). The simulated SFDR curves match well with the measured SFDR curves, confirming the accuracy of the characterization techniques proposed in this investigation.

Furthermore, careful selection of λ_{in} and P_{in} is required for a given Si RM to maximize its SFDR for linear applications. For example, the proposed coherent IQ modulators based on Si RMs in Fig. 1-13 have an operation wavelength (λ_{in}) very close to the resonance wavelength as shown in Fig. 3-5. As observed in the results of Fig. 3-17(c), this near resonance operation wavelength (λ_{in}) leads to significantly lower SFDR values, making it challenging to expand to higher-order coherent modulation formats such as 16 QAM and 64 QAM with the proposed structure [59].

3.6. Summary

The fundamental structure and operation principle of depletion-type Si RMs are described, which covers from the Si RR to the Si RM with the detailed explanation of modulation through the p-n diode in the circumference of the RMs. The RTT is used to understand the transmission characteristics based on their model parameters α and γ, and the CMT is introduced as a more simple and efficient way to describe the time-domain behavior and the frequency response of the RMs based on their model parameters such as τ_l, τ_e, and ω_{res}.

The phase modulation characteristics of the Si RMs are explained in terms of the three different types of coupling (over-coupled, critical-coupled and under-coupled) of Si RMs, with an emphasis on the potential use of the Si RMs for coherent IQ modulators/transmitters. In addition, the operation condition for the phase modulated RMs is described.

Besides the optical model parameters of the Si RMs, the electrical components such as R_s and C_j are introduced, and their influence on the entire E/O responses is also included in the characterization for the accuracy of the model.

The modulation linearity of Si RMs is analyzed using CMT-based

time-domain to frequency-domain numerical analysis. The purpose of this investigation is to confirm the CMT model's accuracy, to explore the linear operation point with respect to λ_{in} and P_{in} and to figure out the possibility of the higher-order coherent modulation based on the Si RMs. For this, the optical and electrical parameters are extracted from the measured optical transmission spectra and the electrical reflection coefficients. The self-heating effect on the RM's transmission characteristics is introduced. The one-tone RF modulated optical spectrum and peak optical powers are measured, and the two-tone RF modulated RF spectrum and peak RF power are also measured, both of which confirms the validity of the proposed characterization technique for the modulation linearity of the RMs. The careful selection of P_{in} and λ_{in} values is required for linear modulation applications. In addition, the implementation of the higher-order coherent modulation with suggested structure of the coherent IQ modulators based on the RMs is challenging due to near resonance operation properties of the phase modulated RMs.

4. Optimization of Coherent Transmitter EPIC [2]

4.1. Device Structure

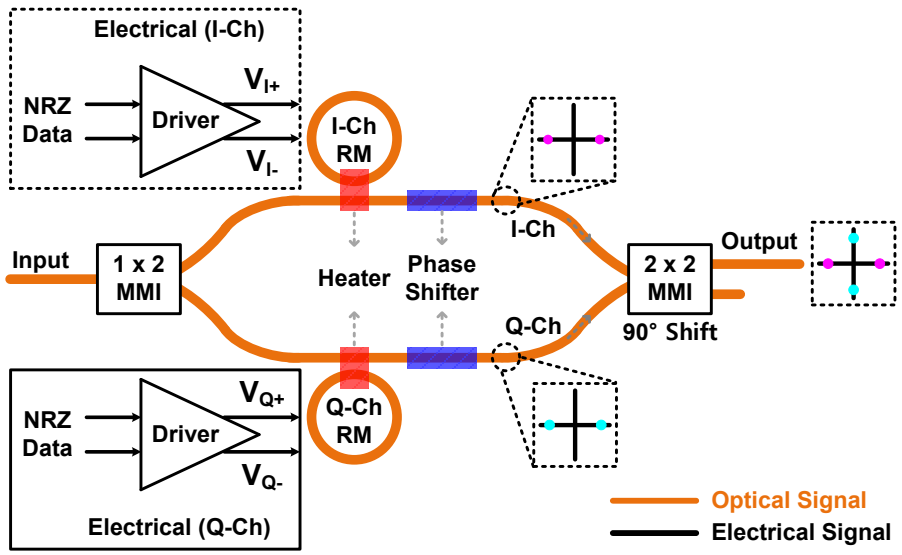

Fig. 4-1. Schematic of Si coherent transmitter EPIC based on RMs.

Fig. 4-1 shows the schematic of a coherent transmitter EPIC based on the RMs which can be designed and fabricated using IHP's Si

[2] © 2023 IEEE. Reprinted with permission from "Y. Jo *et al.*, A Si Photonic BiCMOS Coherent QPSK Transmitter Based on Parallel-Dual Ring Modulators, *2023 IEEE Silicon Photonics Conference (SiPhotonics)*, Washington, DC, USA, April 2023, pp. 1-2"

photonic BiCMOS process. It is briefly introduced in Fig. 1-13 and in [82], but the details of its individual components are provided, and the optimization results of the device performance are presented.

The photonic components of the coherent transmitter EPIC, a coherent IQ modulator, are mainly composed of the ring-assisted Mach-Zehnder interferometers (RaMZI). The input optical signal to the IQ modulator is split into a 50:50 ratio by a 1 x 2 multimode interferometer (MMI), with two identical single-quadrature RMs located in each arm of MZI to independently generate modulation signals for the I-channel and Q-channel. These independently generated I- and Q-channel signals are combined through a 2 x 2 MMI with a 90-degree phase difference to operate as the coherent IQ modulator.

Due to process variations in Si PIC technology [69], there are possibilities of having mismatch of the photonic components [82]. Firstly, two RMs may have different values of λ_{res}, and it causes the failure of coincidence of the phase modulation operation point (λ_{in}) described in Fig. 3-5. Secondly, the arm lengths of the MZI may have different values, and it introduces an unintended additional phase difference deviating from the desired phase difference, 90 degrees. Both result in the failure of operation as the coherent IQ modulators and make it challenging to generate the correct coherent IQ modulation

signals. To solve these problems, on-chip thermo-optic components are integrated. For the resonance mismatch of the RMs, heaters are integrated into each RM to align the λ_{res} values of the two RMs, and for the phase mismatch of the MZI, phase shifters are integrated into each arm of the MZI to compensate the phase difference due to the arm length difference.

The electronic circuit of the coherent transmitter EPIC is the RM driver electronics, which is designed to independently supply the electrical signal with the required voltage (V_π) for the 180-degree phase modulation to the two RMs at the target data rate. The I- and Q-channel RM drivers amplify high-speed input non-return-to-zero (NRZ) signals to the desired voltage and differentially deliver them to the RMs. These two channel RM driver electronics also operate independently. The output voltage of the driver electronics is limited to maximum 6 $V_{peak\text{-}to\text{-}peak,\ diff}$.

Realizing a high-performance coherent transmitter EPIC based on RMs requires optimizing the phase modulation performance of the photonic components, specifically the RMs, as well as the performance of the RM driver electronic circuits.

4.2. Phase Modulation Characteristics of the RMs

The performance metrics of the phase-modulated single-quadrature RMs include (i) the required voltage (V_π) for achieving 180-degree phase modulation, (ii) dynamic insertion loss (IL) at the operation wavelength (λ_{in}) as explained in Fig. 3-5 and Chapter 3.3, (iii) the 3-dB modulation bandwidth (BW) required to transmit the high-speed signals and (iv) Q factor of the RM. It is worth noting that the small-signal E/O frequency responses in Eq. (3.12) is not proper approach for the phase-modulated RMs because D_ω and D_λ values are close to zero due to near λ_{res} operation, and it is numerically modeled for the transmitted intensity of intensity-modulated RMs [61,62].

Thus, the time-domain to frequency-domain numerical analysis technique based on CMT in Chapter 3.5 is used to build an accurate and efficient model for the analysis of the phase modulation characteristics of RMs. RM's CMT optical model parameters such as τ_l, τ_e, and n_{eff}, as well as RM's electrical model parameters such as R_s and C_j, depend on the RM's structure. For instance, the value of τ_l depends on the radius of the RM, and τ_e depends on the coupling gap of the RM. Before analyzing the dependence of the RMs on their structure, an RM with a 16-μm radius and a 220-nm structure is considered as a sample of a

single-quadrature RM, denoted as "16_220." This device is designed based on a waveguide structure that is 500 nm wide and 220 nm thick, with a slab thickness of 100 nm as in Fig. 3-3. The nominal peak carrier concentrations for the p-region and n-region are 7 x 10^{17} cm^{-3} and 3 x 10^{18} cm^{-3}, respectively, as described in Chapter 3.1.

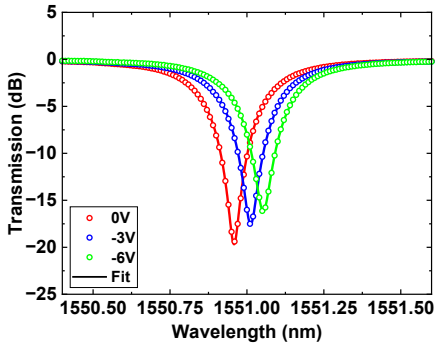

(a)

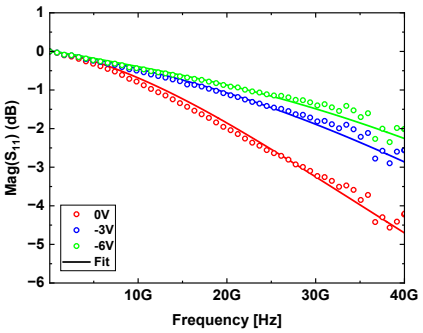

(b)

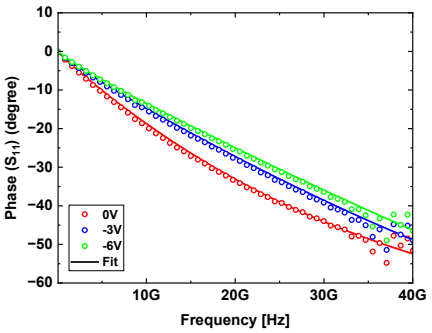

(c)

Fig. 4-2. Measurement and fitting to obtain the model parameters of the sample RM. Measured and fitted (a) optical transmission spectra, (b) magnitude and (c) phase of electrical S_{11} for different bias voltages.

Bias (V)	n_{eff}	τ_l (ps)	τ_e (ps)	R_s (Ω)	C_j (fF)
0	2.607275	21.4635	17.5920	105.7	34.96
-1	2.607314	22.0344	17.5922		30.58
-2	2.607340	22.4142	17.5924		28.00
-3	2.607366	22.6938	17.5926		26.21
-4	2.607389	23.0973	17.5927		24.84
-5	2.607412	23.3947	17.5929		23.74
-6	2.607435	23.7619	17.5930		22.81

Table 4-1. Extracted model parameters of the Si RM.

Fig. 4-2(a) shows the measured optical transmission spectra of the sample RM at different bias voltages. Using Eq. (3.10) and a least mean square fit, the model parameters, τ_l, τ_e, and n_{eff}, can be extracted. Fig. 4-2(b) and (c) respectively show the magnitude and phase of the electrical reflection coefficient (S_{11}) at different bias voltages. Using the equivalent circuit for the electrical parts of RMs and a least mean square fit, the model parameters, R_s and C_j, can be extracted. All the solid lines in Fig. 4-2 represent the fitting curves required for the model parameter extraction, and the extracted model parameters for the sample RM are presented in Table 4-1.

Analysis of the sample RM reveals that V_π of 5.7 V and λ_{in} of 1551.01 nm for BPSK modulation. An E/O modulation efficiency of

the sample RM is analyzed to be 15.1 pm/V of $\Delta\lambda_{res}$ from 0 V to V_π V, and optical loss of the sample RM is analyzed to be 35.86 dB/cm for 0 V and 32.54 dB/cm for V_π V. At this point, the dynamic IL of the RM is 10.0 dB. The "16_220" sample RM has 6,117 of quality (Q) factor.

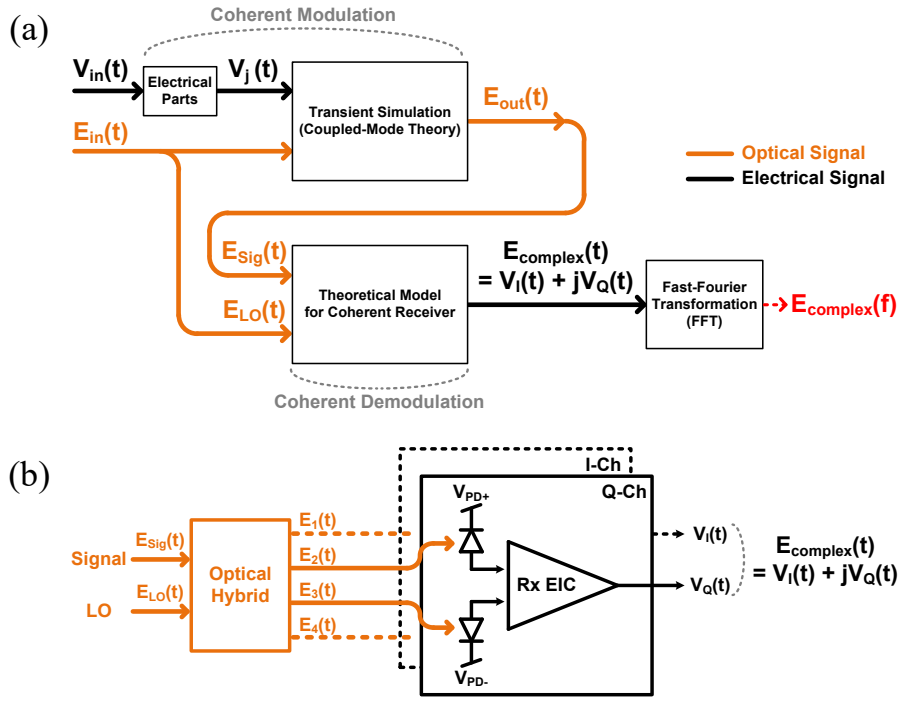

Fig. 4-3. (a) Conceptual diagram of coherent modulation and demodulation, (b) theoretical coherent receiver.

The phase modulation frequency response of the RM can be characterized by obtaining the time-domain complex signal of the RM using CMT-based techniques. For this, Fig. 4-3(a) and (b) show a

conceptual diagram of the coherent modulation and demodulation processes, and the theoretical coherent receiver architecture, respectively. With the given model parameters, the time-domain complex signal, $E_{out}(t)$, of the RM is numerically calculated for a given modulation angular frequency, ω_m, and then, the solution is supplied as the signal input to the theoretical coherent receiver. Additionally, $E_{in}(t)$, which is an optical input signal of the RM, is applied as the local oscillator (LO) input of the theoretical coherent receiver, using a homodyne reception scheme. The relations of the input and output signals for the optical hybrid in the theoretical coherent receiver, as shown in Fig. 4-3(b), are described as follows [28],

$$E_1 = \frac{1}{2}(E_{sig} + E_{LO}), \tag{4.1}$$

$$E_2 = \frac{1}{2}(E_{sig} + jE_{LO}), \tag{4.2}$$

$$E_3 = \frac{1}{2}(E_{sig} - jE_{LO}), \tag{4.3}$$

$$E_4 = \frac{1}{2}(E_{sig} - E_{LO}). \tag{4.4}$$

After down-converted by balanced photodiodes for each channel, resulting I- and Q-channel photocurrents (I_I and I_Q) are given as,

$$I_I(t) = I_1(t) - I_4(t) = R\sqrt{P_s P_{LO}}\cos(\theta_{sig}(t) - \theta_{LO}(t)), \quad (4.5)$$

$$I_Q(t) = I_2(t) - I_3(t) = R\sqrt{P_s P_{LO}}\sin(\theta_{sig}(t) - \theta_{LO}(t)), \quad (4.6)$$

where I_1, I_2, I_3 and I_4 respectively denote the photocurrents of each output port of the optical hybrid. R represents the responsivity of the photodiode, and P_s and P_{LO} represent the optical power of the signal and LO, respectively. θ_{sig} is the phase of the signal, and θ_{LO} is the phase of the LO. Considering the relativity of the phase, θ_{LO} is excluded, and considering the phase noise term, θ_n, the complex photocurrent $I_{complex}$ is given by,

$$I_{complex}(t) = I_I(t) + jI_Q(t) = R\sqrt{P_s P_{LO}}\exp\{j(\theta_s(t) + \theta_n(t))\}, \quad (4.7)$$

where θ_s refers to the modulated phase of the signal. Furthermore, the output photocurrents are amplified by the Rx EIC, which typically consists of TIAs and results in the output signals as voltage signals, V_I and V_Q. The time-domain complex signal, $I_{complex}(t)$, has a phase information of the modulated complex signal, and $E_{complex}(t)$, composed of V_I and V_Q, is equivalent to the RM's output signal, $E_{out}(t)$.

$$E_{complex}(t) = V_I(t) + jV_Q(t). \tag{4.8}$$

As discussed in Chapter 3.5, by taking the FFT of the calculated $E_{complex}(t)$, the complex modulation characteristics of the RM at ω_m can be simulated. With model parameters listed in Table 4-1 and the coherent modulation and demodulation, the complex E/O response of the sample RM can be determined for the frequency range of interest. To calculate single frequency point of E/O response as described, it takes 20 seconds for 100-ns waveform length and 2.5-fs time interval with AMD Ryzen 9 5900X, 64.0 GB RAM PC. The simulation time can be further reduced by decreasing the entire waveform length with smaller frequency resolution. For example, it takes 2 seconds for 10-ns waveform length and 2.5-fs time interval with 100-MHz frequency resolution.

However, for the measurement of the complex E/O response of RMs, it is essential to de-embed the influence of various instrumental components such as the coherent receiver and RF amplifier. Especially, unlike the theoretical coherent receiver, real-world coherent receivers have finite modulation bandwidths and problems including the optical hybrid's excess loss and phase mismatch, and Rx EIC's process variations leading to I- and Q-channel imbalance. Consequently,

characterization of the opto-electronic (O/E) response of the coherent receiver is crucial to obtain a more accurate measurement of the complex E/O frequency responses of RMs. Coherent receivers require a different approach unlike direct-detection receivers that can be measured using light-wave component analyzers (LCAs) and vector signal analyzers (VSAs). For coherent receivers, it is necessary to perform heterodyne measurements of the receiver's O/E response by supplying different laser sources into the two optical input signals of the coherent receiver [83].

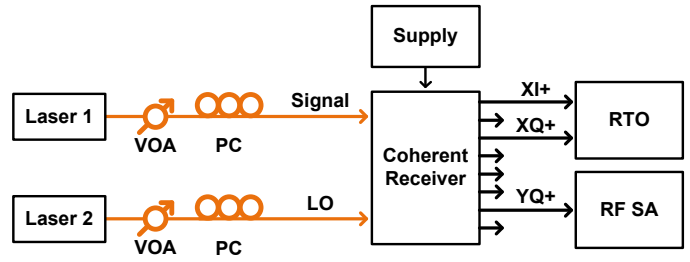

(a)

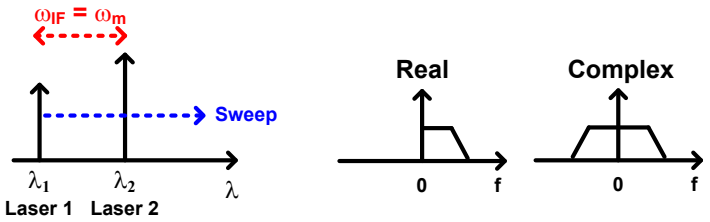

(b) (c)

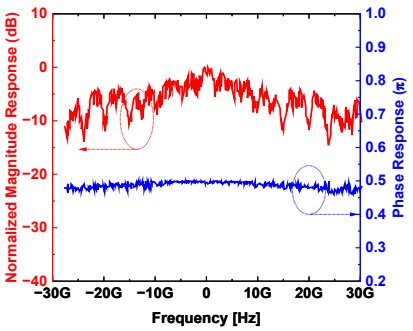

(d)

Fig. 4-4. (a) Heterodyne measurement setup for O/E responses of commercial coherent receiver, (b) conceptual diagram to explain the relation between intermediate frequency (ω_{IF}) and modulation frequency (ω_m), (c) difference in signal's spectra between real signal and complex signal and (d) the measured normalized magnitude and phase response of the commercial coherent receiver for de-embedding.

Fig. 4-4(a) shows the heterodyne measurement setup required for the coherent receiver. Commercial coherent receiver, Fujitsu FIM24902, has been used in the experiment, and its datasheet reveals a 3-dB modulation bandwidth of typically 40 GHz and phase imbalance within +/- 7.5 degrees. Laser 1, Agilent 81600A, has been used with an output power of +0 dBm, while Laser 2, Coherent-Solutions LaserMatrIQ-1004-1-FA, has been used with an output power of +10 dBm. Polarizations of both laser sources have been controlled to maximize X-polarization signal while minimizing Y-polarization signal. The receiver has differential output ports for the I and Q channels, but only I+ and Q+ channels have been used for the measurements, while the remaining channels have been terminated.

Fig. 4-4(b) shows a conceptual diagram illustrating the relative wavelengths of Laser 1 and 2. The wavelength difference of the two laser sources denoted as an intermediate frequency (ω_{IF}) equals to having the single-sideband modulation signal supplied to the coherent receiver with modulation frequency (ω_m). Fig. 4-4(c) shows the differences in the spectra between real and complex signals. The complex signal contains data in the negative frequency domain due to the presence of both real (I) and imaginary (Q) components. The time-domain output signal of the coherent receiver, acquired from the RTO,

is FFT-ed to obtain the O/E response of the coherent receiver. Fig. 4-4(d) shows the measured normalized magnitude and phase response of the coherent receiver, and this can be used for de-embedding required to characterize the complex E/O response of RMs.

In addition to the homodyne reception scheme described in Eq. (4.5)-(4.8), the heterodyne reception scheme is used for the measurement of E/O response of the RM. This leads to an additional ω_{IF} term of $I_{complex}$ in Eq. (4.7) as follows.

$$I_{complex}(t) = R\sqrt{P_s P_{LO}}\exp\left\{j(\omega_{IF}t + \theta_s(t) + \theta_n(t))\right\}, \tag{4.9}$$

Due to the presence of the intermediate frequency components in the signal, the carrier frequency offset compensation [84] is included in the digital signal processing (DSP) algorithms.

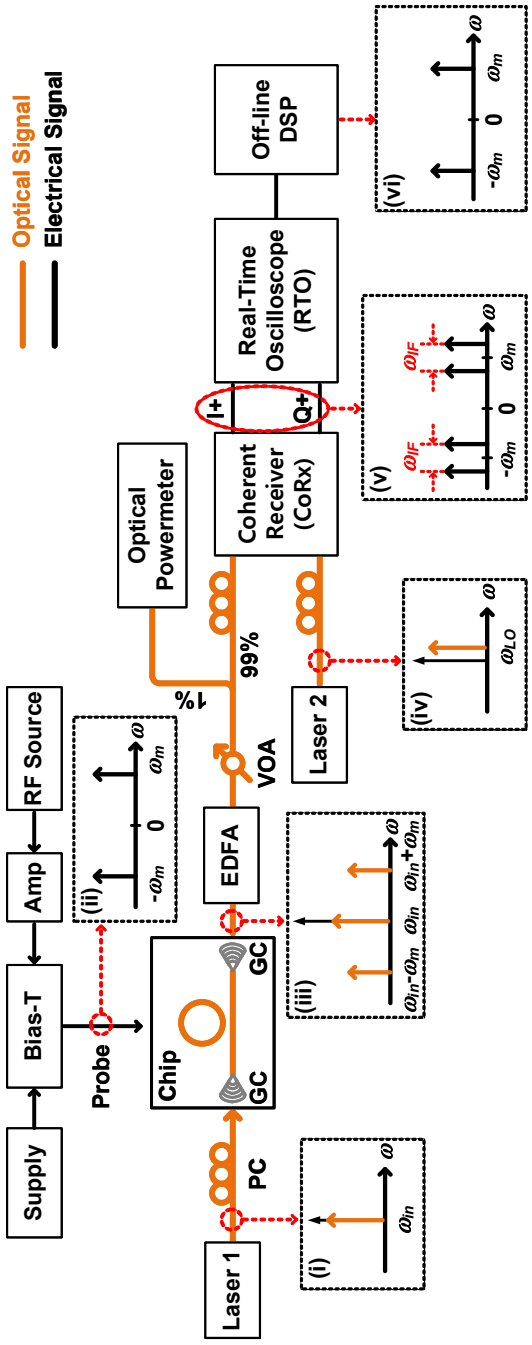

Fig. 4-5. Heterodyne measurement setup for complex E/O response of RMs. The dashed insets are optical or electrical spectrum for each stage.

Fig. 4-5 shows the measurement setup for the complex E/O response of RMs characterization, with dashed insets (i)-(vi) explaining the optical or electrical spectra at each stage. Firstly, the optical input signal of the RM at ω_{in} in (i) is modulated by the supplied modulated signal at ω_m in (ii) and converted to carrier and sideband signals in (iii). For measurements, RF signals with a 5.7 $V_{peak\text{-}to\text{-}peak}$ which equals to the V_π of the sample RM are applied to the RM with a bias voltage of a half of V_π. GCs are used as optical I/Os, and the polarization of both input and output signals of the RM is controlled to maximize the X-polarization signal. An EDFA amplifies the RM's output signal, and the power of the amplified signal is controlled with a VOA for the coherent receiver's input signal. The modulated output signal of the RM as well as the optical signal at ω_{LO} in (iv) is supplied to the signal port and LO port, respectively. The value of ω_{IF} is maintained below 300 MHz.

The obtained output signals of the coherent receiver in (v), I+ and Q+, pass through the off-line digital signal processing (DSP) algorithms, including carrier frequency offset compensation to remove the ω_{IF} component and digital bandpass filtering to reduce out-of-band noise, resulting in the recovered E-field as in (vi). The recovered E-field is then analyzed in the frequency domain by taking the FFT, and during this process, the responses of the RF amplifier, cables, probes

and the heterodyne-measured O/E frequency response described in Fig. 4-4 have been all de-embedded [82,83].

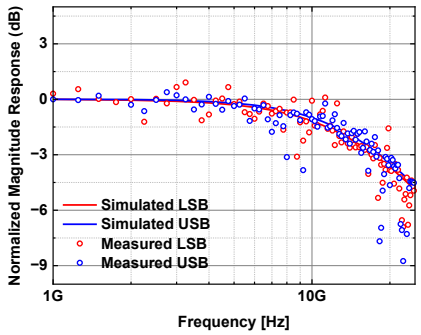

(a)

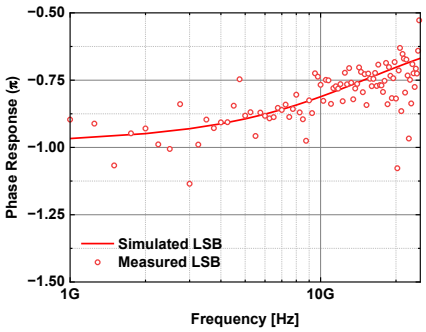

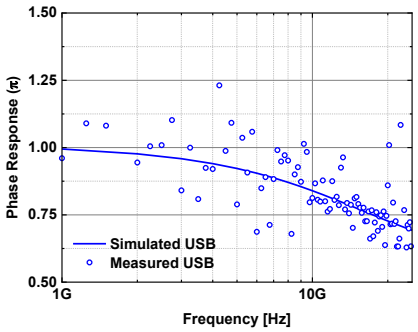

(b) (c)

Fig. 4-6. Measured and simulated complex E/O frequency response of the sample RM, “16_220”, (a) normalized magnitude response for LSB and USB, phase response for (b) LSB and (c) USB.

Fig. 4-6 provides the measured and simulated complex E/O response of the sample RM, "16_220." The model parameters in Table

4-1, obtained from Fig. 4-2, are used in the simulation. Although the measured responses contain a certain amount of error, the overall measured responses agree well with the simulated, confirming the validity of the proposed characterization method. A correlation between the measured and the simulated is calculated as 0.70. The deviation comes from insufficient de-embedding of the equipment used in the characterization, composed of reflections of high-speed signals and randomness of the noise.

An important observation is as follows. As explained in Eq. (3.12), the small-signal response of the RM has a 2-pole, 1-zero system with pole (p) and zero (z) values given by,

$$p = -\frac{1}{\tau} \pm jD_{\omega}, \quad z = -\frac{2}{\tau_l}. \tag{4.10}$$

The phase modulation of the RM has distinctive characteristics: (i) D_{ω} is very close to 0 and (ii) the RM for phase modulation has an over-coupling condition ($\tau_l > \tau_e$) very close to a critical-coupling condition ($\tau_l = \tau_e$). Due to these phase modulation characteristics and Eq. (3.9), the positions of the poles and zeros in Eq. (4.10) are very close to each other. As a result, the frequency response of the RM, which has a 2-

pole, 1-zero system for intensity modulation, can be approximated as a 1-pole system for phase modulation for the described λ_{in}.

From Fig. 4-6(a), it can be observed that the measured 3-dB bandwidth of the E/O magnitude response for "16_220" is 18.5 GHz. Furthermore, at this 3-dB bandwidth frequency, Fig. 4-6(b) and (c) show that the phase response experiences an approximately $\pi/4$ reduction. This suggests phase modulation characteristics consistent with a 1-pole system, which exhibits a 3-dB attenuation of the magnitude response and a $\pi/4$ reduction in the phase response at the pole. Therefore, it is evident that characterizing the E/O response of the phase-modulated RM in terms of the magnitude response alone is sufficient.

4.3. Optimization of RMs for Phase Modulation

In addition to the sample RM, "16_220," the single-quadrature RMs with different model parameters, τ_l and τ_e, have been fabricated and examined to analyze the performance dependence on the RM structure, especially on the radius and the coupling gap. Fig. 4-7 presents the simulated distribution of dynamic IL, V_π, 3-dB E/O bandwidth and Q factor with respect to the model parameters, τ_l and τ_e. The figure also shows the measured results of 5 fabricated sample RMs, represented as circles located in their measured model parameters and performance metrics. Similar to "16_220," these sample RMs are labeled with their respective "radius" and "coupling gap" next to the circles.

Under-coupled RMs ($\tau_l < \tau_e$) have been excluded from the design range since a π-degree phase shift cannot be achieved. In contrast, critical-coupled RMs ($\tau_l = \tau_e$) have more abrupt 2π phase shift around the resonance wavelength compared to over-coupled RMs ($\tau_l > \tau_e$) as in Fig. 3-4. Due to the abrupt phase shift, the π phase shift can be achieved with a smaller V_π. Also, the critical-coupled RMs have higher Q factor compared to over-coupled RMs, which leads to a sharper resonance notch in their transmission spectra. Because of this, the dynamic IL of the critical-coupled RM is higher with Q-factor

increased, leading to a tight link power budget for a coherent transmission system. Fig. 4-7(a) and (b) clearly demonstrate that single-quadrature RMs approaching critical coupling have higher dynamic IL and smaller V_π, while the opposite trend is true for the RMs which are far from the critical coupling. For example, in Fig. 4-7, "16_240" is closer to the critical coupling than "16_220". This leads to higher insertion loss for "16_240" at the cost of achieving low V_π.

Additionally, the 3-dB E/O bandwidth in Fig. 4-7(c) is limited as the RM model parameters, τ_l and τ_e, become large because τ_l and τ_e also mean the time constants. Fig. 4-7(d) shows the values of the Q factor in terms of τ_l and τ_e, indicating that the RMs have high Q factors when the RM is designed near the critical coupling. The fabricated sample RMs have Q factors from 4,800 to 6,500, which are sufficient values for a few tens of GHz of 3-dB bandwidth.

Furthermore, the design limits shown in Fig. 4-7 indicate the smallest coupling gap allowed according to the design rule of the Si photonic BiCMOS process and the maximum peak-to-peak differential output voltage achievable in BiCMOS driver electronics.

The 3-dB electrical bandwidth of RMs does also have the dependence on the structure, only related to the RM's radius rather than the coupling gap of the directional coupler because the p-n diode of the

ring has the design variety only for the radius. Fig. 4-8 presents the 3-dB electrical bandwidth of RMs with 8, 12, and 16 μm radius at different reverse bias voltages, calculated based on the measured S_{11} from the fabricated sample RMs, and the figure reveals that the fabricated sample RMs have sufficient bandwidth to support the target baud rate of 28 Gbaud.

In summary, the single-quadrature RMs tend to have either (i) a large modulation bandwidth, high V_π and low dynamic IL with low Q factor or (ii) a small modulation bandwidth, low V_π and high dynamic IL with high Q factor. The electrical characteristics of single-quadrature RMs are sufficient for the transmission of 28-Gbaud signal. Based on these optimization results, the "16_220" RM has been integrated as a single-quadrature RM for the single-polarization, 28-Gbaud coherent QPSK transmitter EPIC. Detailed measured and simulated performance metrics for the decision to select the "16_220" RM are provided in Table 4-2.

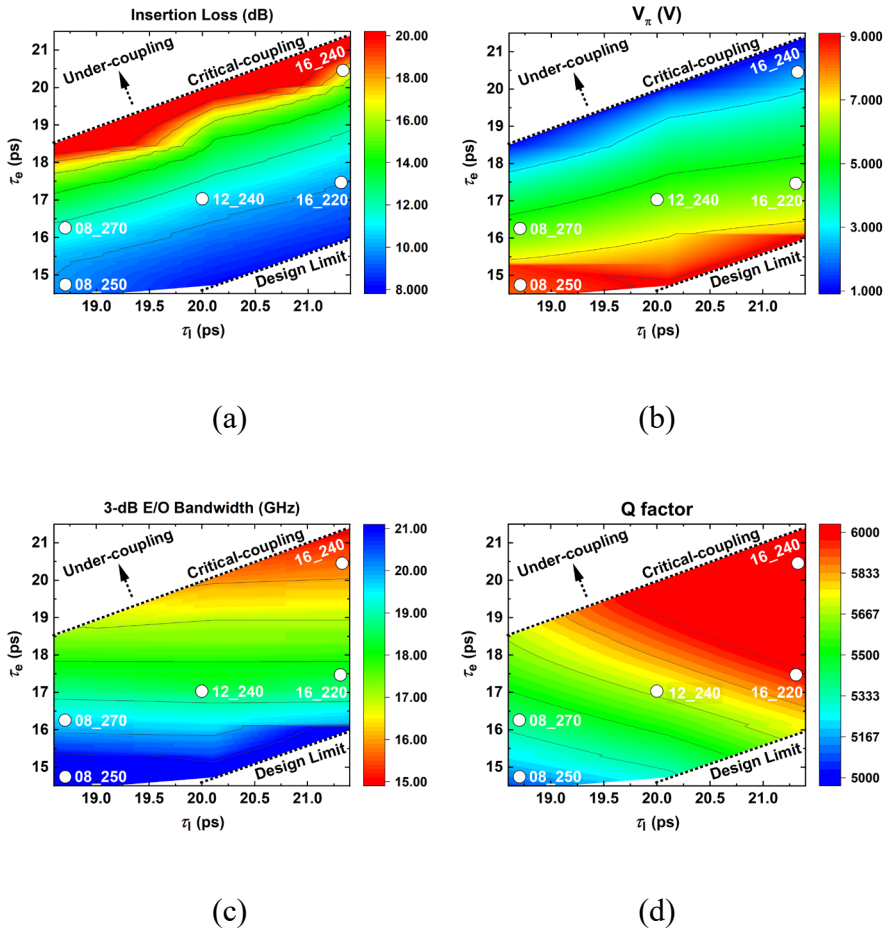

Fig. 4-7. Performance of single-quadrature RMs in terms of τ_l and τ_e at 0 V. (a) Dynamic insertion loss in dB, (b) V_π in V, (c) 3-dB E/O bandwidth in GHz and (d) Q factor. The circles indicate the measured result of the fabricated RMs.

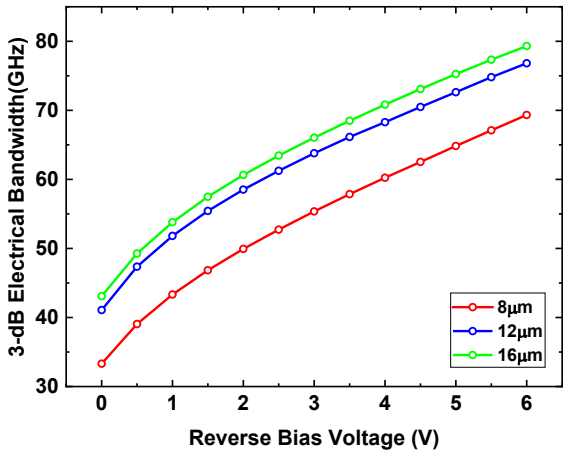

Fig. 4-8. Calculated 3-dB electrical bandwidth of RMs for 8μm, 12μm and 16 μm of radius. The bandwidths are calculated from the R_s and C_j values obtained from the measurements.

Radius [μm]		8	8	12	***16***	16
Coupling Gap [nm]		250	270	240	***220***	240
Device		08_250	08_270	12_240	***16_220***	16_240
V_π (V)	Measured	7.7	5.4	6	***5.7***	2.8
	Simulated	8.09	5.53	5.93	***5.65***	2.25
Dynamic insertion loss (dB)	Measured	10.63	11.92	10.63	***10.0***	15.66
	Simulated	9.7	11.7	10.6	***10.1***	16.6
3-dB bandwidth (GHz)	Measured	21.5	19.5	19.25	***18.5***	14.75
	Simulated	22	19.6	18.8	***18.2***	15.6
Q factor	Measured	4576	5121	5490	***5723***	6307
	Simulated	4802	5384	5684	***6117***	6469

Table 4-2. Measured and simulated V_π, dynamic insertion loss, 3-dB E/O bandwidth and Q factor for 5 different single-quadrature RMs.

4.4. RM Driver Electronic Circuit

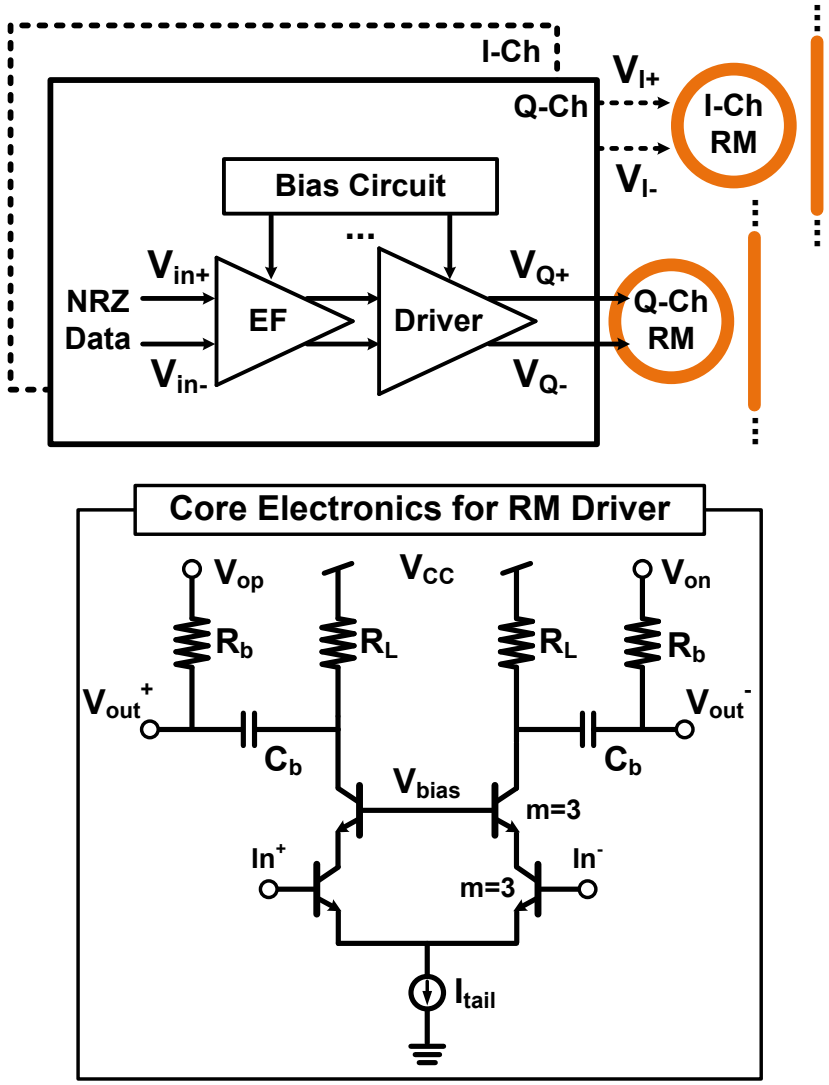

Fig. 4-9. (a) Block diagram of the RM driver electronic circuit, (b) schematic of driver core.

Fig. 4-9 shows the schematic of the RM driver electronic circuits based on BiCMOS process. Two sets of drivers are used to amplify the externally supplied high-speed NRZ data to provide the desired V_π to the individual RMs. These drivers independently modulate the I- and Q-channel single-quadrature RMs of the coherent IQ modulator based on RaMZI. Emitter followers (EF) are integrated to buffer the input electrical signal for the next stage. The driver core consists of a fully differential cascode structure, which can deliver a maximum 6 $V_{peak\text{-}to\text{-}peak,diff}$ to the RM without any breakdown of transistors. The bias voltages for the driver are provided by bias circuits composed of an operational transconductance amplifier and a replica circuit of the driver core. External bias voltages are supplied to the RMs from the output stage of the driver with a capacitive coupling.

Fig. 4-10 presents the post-layout simulated eye diagram for a 28-Gbps NRZ signal with a 5.7 $V_{peak\text{-}to\text{-}peak,diff}$ using the electrical parameters obtained from the optimized RM, "16_220", in Chapter 4.3.

Fig. 4-11 shows the fabricated coherent transmitter EPIC based on RaMZI, with a chip size of 1.36 mm x 0.78 mm (1.06 mm^2). The figure shows the co-integration of photonic components such as two waveguide paths for the interferometers, MMIs, thermo-optic elements and the RMs, as well as the electronic circuit for the RM driver.

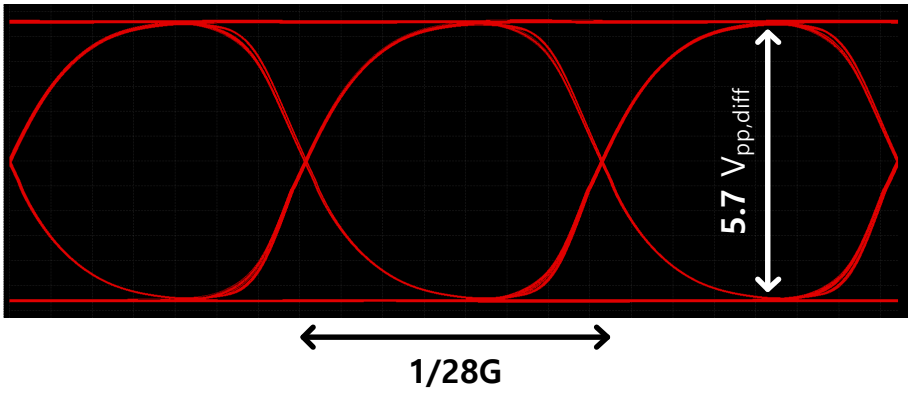

Fig. 4-10. Post-layout simulated eye diagram of the RM driver electronic circuit for 28-Gbps NRZ signal.

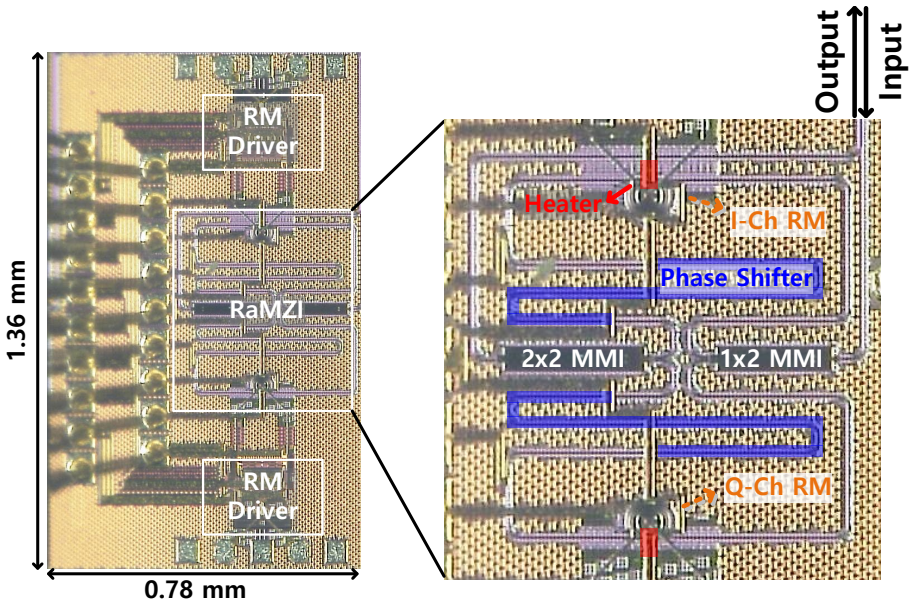

Fig. 4-11. Chip micro photograph of fabricated coherent transmitter EPIC based on RaMZI.

4.5. Summary

For the efficient co-integration of photonic components such as waveguide paths, MMIs, thermo-optic elements and RaMZI as well as the electronic driver BiCMOS circuit, the overview of the structures and individual components of the coherent transmitter EPIC based on the RaMZI are given.

Firstly, the single-quadrature RMs are characterized to achieve the efficient phase modulation for the coherent IQ modulation. For this, the CMT-based time-domain to frequency-domain numerical analysis is carried out with the measured model parameters, and experimentally verified. The detailed analysis of the complex E/O response of the single RM is described with the theoretical explanation about the coherent modulation and demodulation.

Then, the modulation performance of the RMs are optimized with their performance metrics, dynamic IL, V_π, 3-dB modulation bandwidth and Q factor to investigate the structure dependence on the performance. The trade-offs between dynamic IL, V_π, 3-dB modulation bandwidth and Q factor are explored, providing insights into the design of coherent IQ modulators for the desired phase modulation requirements. For this, the fabricated single-quadrature RMs are

measured and analyzed.

Furthermore, the schematic of the RM driver electronic circuits is explained, which is co-integrated to independently supply the required voltage with the desired data rate for phase modulated RMs. Also, the fabricated coherent transmitter EPIC is shown, demonstrating the co-integration of photonic and electronic components.

5. Measurement of the Coherent Transmitter EPIC with a Receiver EPIC

5.1. Alignments of Photonic Components in Transmitter EPIC

Fig. 5-1(a) illustrates the structures of the integrated heaters within the directional coupler, composed of N-type doped Si waveguides with an N+/N/N+ configuration as well as the phase shifters integrated into a bottom metal layer located at the top of each arm of the MZI. In Fig. 5-1(b), a conceptual diagram is provided to describe the compensation technique for the resonances of the two RMs and the phase mismatch of the MZI.

Due to process variations, the proposed coherent IQ modulators can have mismatch in the resonance wavelengths of the two RMs, λ_{res1} and λ_{res2}, as well as the phase mismatch (ϕ) of the MZI, which is required to be precisely 90 degrees. To solve these, the heater integrated in the RM1, assumed that its λ_{res} is on the left side of the RM2, is operated to make the value of λ_{res1} equal to λ_{res2}. Then, the phase shifter in one of the MZI arms is swept to identify the quadrature bias point where a 90-degree phase difference is achieved. This

iterative process determines the biases required for the heater and phase shifter to ensure that λ_{res1} and λ_{res2} match, and ϕ has the desired 90-degree phase difference. As explained, one of the heaters where the RM has the shorter resonance wavelength is operated, and one of the phase shifters is operated.

The measured performances of the thermo-optic components reveal that, to cover half of the FSR (FSR of 6.24 nm for "16_220"), 45.7 mW of power is required for the heater. In addition, to compensate for the 2π phase mismatch within the MZI, 57.9 mW of power is required for the phase shifter. The transmitter EPIC has been placed on a temperature-controlled stage whose temperature is maintained at 25°C for all measurements. The heaters and phase shifter locally heat to align the coherent IQ modulator for operation, and its temperature can reach up to 65°C without any breakdown of the device [65].

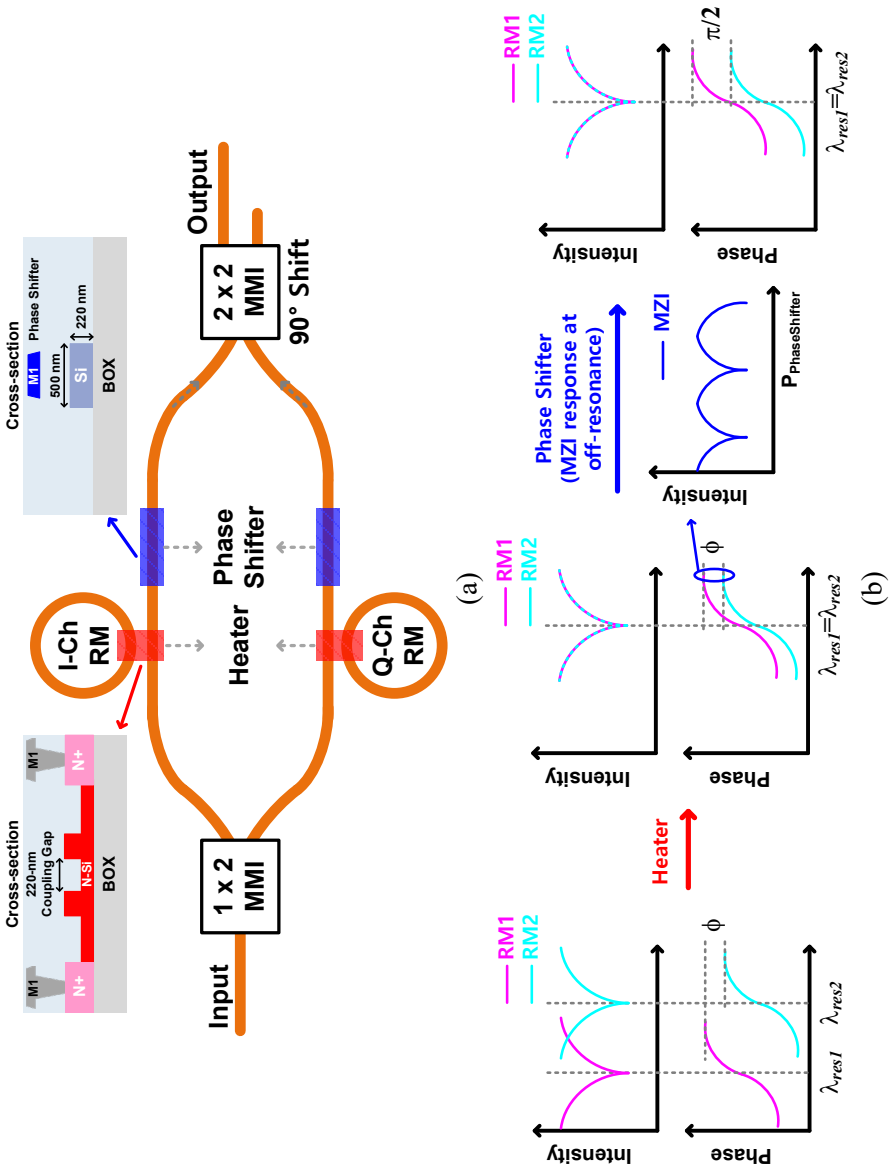

Fig. 5-1. (a) Cross-section diagram for integrated heater and phase shifter. (b) Conceptual diagram for alignments of the resonance of the two RMs and the phase of the MZI.

5.2. A Coherent Receiver EPIC

In Chapter 4, the commercial receiver has been used to characterize the phase modulation behavior of the RMs. However, the potential as an monolithic all-silicon transceiver sub-assembly EPIC based on the RMs is explored through co-measurements of the fabricated transmitter EPIC in Fig. 4-11 with the coherent receiver EPIC, also realized within the Si photonic BiCMOS process.

Fig. 5-2 presents the chip microphotograph and schematic of the fabricated Si photonic BiCMOS coherent receiver EPIC, with a chip size of 3.41 mm x 1.61 mm (5.49 mm^2) [83,85]. For optical I/O, a pair GCs is used, along with an additional pair of GCs integrated for optimized coupling efficiency monitoring. The optical quadrature hybrid is realized with a 4 x 4 MMI, which has a 189-μm length and 10-μm width [86]. The MMI's outputs are terminated with four single-ended Ge photodiodes (two pairs of balanced photodiodes), which are then connected to the Rx front-end EIC.

The electronic output stage circuit for each channel consists of a TIA, two stages of variable gain amplifiers (VGA), a 50-ohm output buffer, a gain control loop and a dc offset cancellation loop, providing differential outputs for both the I-channel and Q-channel signals. The

fully differential input transimpedance stage enables compensation for mismatches arising from the single-ended photodiodes through the dc offset cancellation loop. The electronic circuit design is based on the designs of the optical direct-detection receivers in [87] and optical coherent receivers in [88], both of which are fabricated by IHP's SiGe BiCMOS electronic IC process. Previously, the coherent receiver EPICs with similar design configurations have demonstrated a typical 3 dB O/E bandwidth of around 30 GHz. Further details can be found in [83], [85], [87,88].

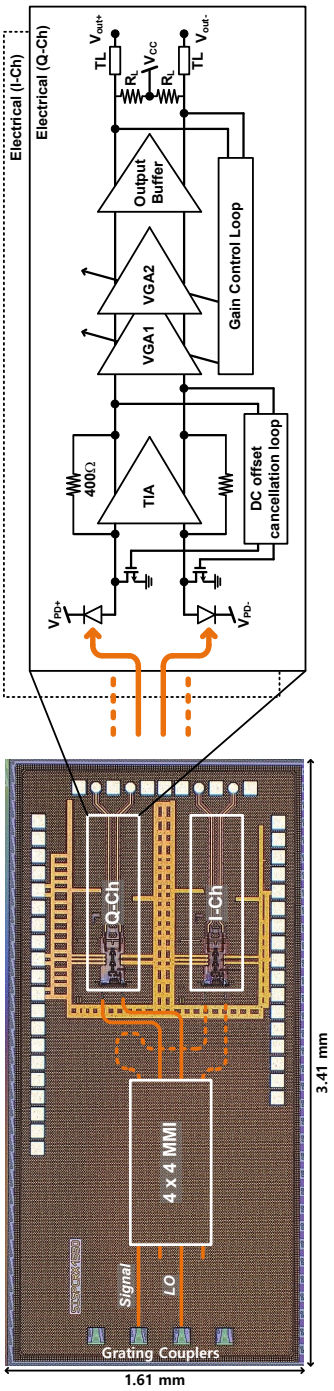

Fig. 5-2. Chip microphotograph and schematic of Si photonic BiCMOS coherent receiver EPIC.

5.3. Measurements of the Coherent Transceiver EPICs

Fig. 5-3(a) and (b) show the measurement setups for the bit-error rate (BER) of the coherent transceiver EPICs in terms of the received optical power (ROP) and the optical signal-to-noise ratio (OSNR).

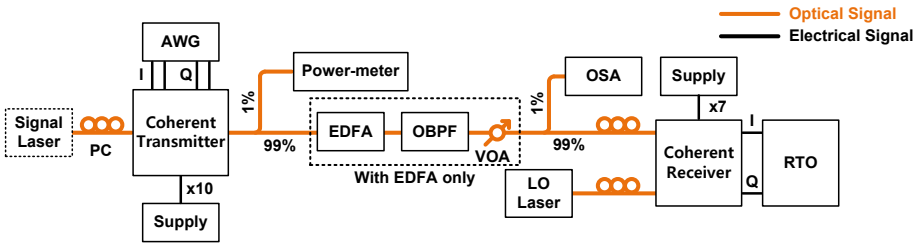

(a)

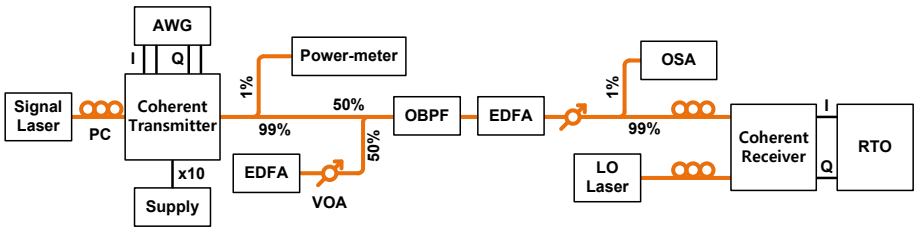

(b)

Fig. 5-3. Measurement setup for bit-error ratio (BER) of the coherent transceiver in terms of (a) receiver optical power (ROP) and (b) optical signal-to-noise ratio (OSNR).

An arbitrary waveform generator (AWG, Keysight M8199A, 256 Gsa/s) generates electrical 28-Gbaud QPSK signals, and these signals,

filtered with a root-raised cosine filter having a roll-off factor of 1.0, have amplitudes of 750 m$V_{peak\text{-}to\text{-}peak,diff}$ for the I-channel and 850 m$V_{peak\text{-}to\text{-}peak,diff}$ for the Q-channel. The electrical QPSK signals are fed to the coherent transmitter EPIC through a pair of GSGSG RF probes so that the required V_π of 5.7 $V_{peak\text{-}to\text{-}peak}$ is delivered to the RMs after amplified by the driver electronics. The transmitter EPIC chip is mounted on an FR4 printed circuit board (PCB), which provides the necessary biases for the BiCMOS RM driver circuits and optical components as well. The biases for the receiver EPIC are directly supplied from the DC probes.

For measurements with respect to the ROPs, the output optical signal of the transmitter EPIC is fed to the receiver EPIC after amplified by the EDFA and filtered by an optical bandpass filter (OBPF) whose bandwidth is set to be 0.8 nm. The VOA is used to control the ROP for the receiver. To examine the possibility of inter-chip connection of these transmitter EPIC and receiver EPIC, the entire transceiver EPICs are also tested without the EDFA. For the setup without the EDFA, the EDFA, OBPF and VOA which are denoted as "with EDFA only" in the Fig. 5-3(a) are removed.

For measurements with respect to the OSNR, an additional EDFA and VOA are added to the fiber-optic setup between the transmitter and

the receiver to adjust the noise levels for different OSNR values. The receiver is changed to a commercial coherent receiver (Fraunhofer CRF-70-EH). The measurement setups in Fig. 5-3(b) have different configurations for the receiver such as the presence of the power supply for the receiver EPIC and the on-wafer RF probes. The OSA monitors the spectrum of the QPSK signals from the transmitter and measures the OSNR, while an optical power meter tracks the split output power of the transmitter.

The optical signal input for the transmitter and for the receiver are provided by laser sources. Two types of signal lasers are used to demonstrate the potential implementation of the coherent transceiver sub-assembly for high-speed DCI. One is an external cavity laser (ECL, Agilent 81960A) whose linewidth is 100 kHz, and the other is a C-band single-mode vertical cavity surface emission laser (VCSEL) supplied by VERTILAS GmbH., Germany, provided for research purposes.

Fig. 5-4(a) shows a microphotograph of the VCSEL, and the lensed-fiber setup is used to obtain the output optical signal from the VCSEL. The VCSEL used in this measurement typically exhibits an intrinsic linewidth of 6~7 MHz, measured using a delayed self-heterodyne technique, and its power-current-voltage (P-I-V) characteristics are shown in Fig. 5-4(b). A temperature-controlled probe

stage is additionally used to manage the VCSEL's wavelength. Detailed information and characterization for the VCSEL can be found in [89].

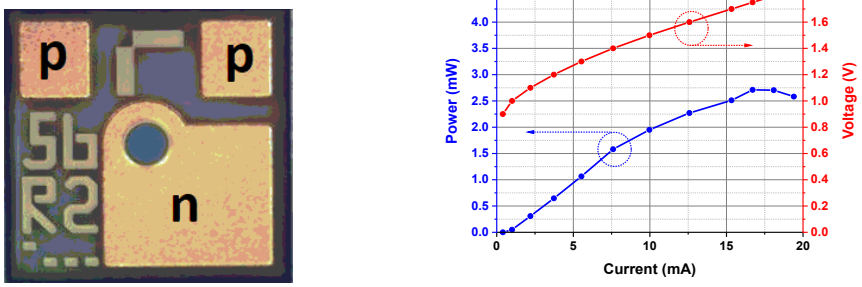

(a) (b)

Fig. 5-4. (a) Micro photograph of a vertical cavity surface emission laser (VCSEL), (b) power-current-voltage (P-I-V) curve of the VCSEL.

The output power and linewidth specifications of the LO have influences on the entire transceiver link performances such as a required sensitivity to the receiver and a block length of DSP algorithm [90]. For the LO laser source, an ECL (Keysight 81608A) whose linewidth is < 10 kHz is used with an output power of +8 dBm for the receiver during measurements.

The signal laser source has an optical power of +3 dBm for the case of ECL and an optical power of +2.1 dBm for the case of VCSEL. For the case of VCSEL, +2.1 dBm of output optical power is de-embedded

values, including losses from the lensed-fiber coupling and PC.

The entire insertion loss of the transmitter is 27.8 dB, including a 12.5 dB coupling loss for the pair of GCs on the transmitter side. The coupling losses for the receiver are 3.8 dB for each GC. Fiber loss between the VOA output and the receiver input as well as fiber array loss is de-embedded in the latter description for the ROP. Polarization for each GC is optimized to maximize output power for single polarization operation.

As described in Chapter 3.5.3, the RMs have a sensitivity to the input power known as the self-heating effect [64], which results in difficult power handling. The actual input power to the RMs is analyzed to be -6.25 dBm because of (i) coupling loss from one GC (6.25 dB), (ii) temporal 3-dB loss from 1 x 2 MMI at the input side of the RaMZI although the signal is combined again at the output side of the RaMZI. With this input power, the RM does not go into a bi-stable operation region. Even though there exists an asymmetric shift in the transmission spectrum, it can be recovered by adaptive equalization in the DSP algorithms.

The receiver's output signals (I+ and Q+) are acquired by RF probes and the RTO (Tektronix DPO77002SX, 200Gsa/s, 70GHz). The other output channels (I- and Q-) are terminated with 50-ohm loads. The

RTO's bandwidth is limited to 32 GHz for 28-Gbaud operation and 28 GHz for 25-Gbaud operation. An off-line DSP is carried out using a communication analyzer tool (Tektronix OM1106) for the RTO, which includes clock recovery, root-raised cosine filtering, carrier phase estimation [91] and least-mean-square adaptive equalization using the constant modulus algorithm [92].

The coherent transmitter EPIC consumes 986.3 mW of power for 28-Gbaud QPSK operation, including the power consumption of the heater (6.4 mW) and the phase shifter (11.4 mW) for the coherent IQ modulator. Bias voltages for the heater and the phase shifter are determined as described in Chapter 5.1. The coherent receiver EPIC consumes 518 mW for 28-Gbaud operation.

Fig. 5-5(a) and (b) respectively show the measured BER as functions of the ROP and the OSNR for 25-Gbaud and 28-Gbaud QPSK signals. In Fig. 5-5(a), both the coherent transmitter EPIC and the receiver EPIC are used in the measurements. The achieved BER performances are below the forward-error correction (FEC) limit with 3.8×10^{-3} of BER threshold, demonstrating the successful operation of the coherent transceiver sub-assembly based on ring modulators within the photonic BiCMOS process for both 25 Gbaud and 28 Gbaud QPSK operations.

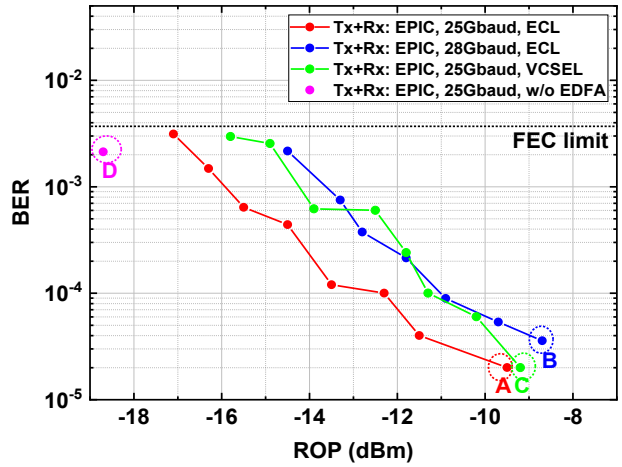

(a)

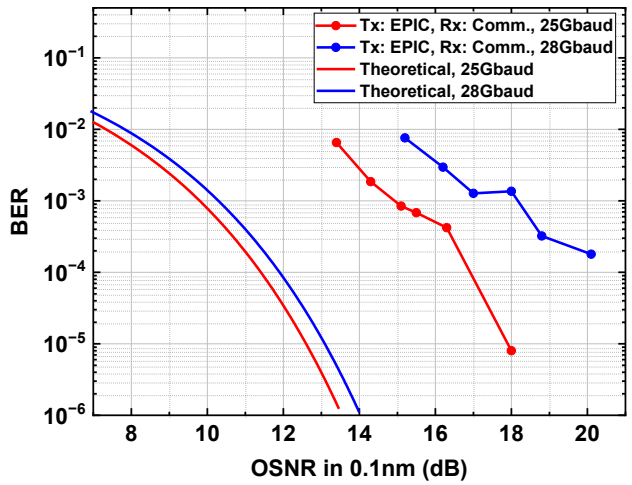

(b)

Fig. 5-5. Measured BER in terms of (a) ROP and (b) OSNR. For ROP measurements, both transmitter EPIC and receiver EPIC are used. For OSNR measurements, a commercial receiver is used. The points A, B, C and D in (a) are example data sets for the next figure.

The ROP penalty observed between 25-Gbaud and 28-Gbaud operations, both of which are measured with an ECL, is found to be 2.0 dB. This penalty is primarily due to the bandwidth limitation of the transmitter EPIC, which is limited by the E/O response of the RM. Additionally, the measured BER using the C-band single-mode VCSEL as a signal laser source shows successful 25-Gbaud operation with a similar penalty to the penalty between 25-Gbaud and 28-Gbaud operation with the ECL. This is due to the phase noise and wavelength fluctuation of the VCSEL [89], which is critical to the RM's stable operation.

In the figure, the measured BER without the use of the EDFA can be found, confirming the possibility of inter-chip connection of the monolithic coherent EPIC transceiver sub-assembly. Although the transmitter and receiver share the same photonic BiCMOS process technology, in this research, they are realized in the separate dies, which requires the use of EDFA due to the tight link power budget resulting from the coupling loss of GCs and fiber loss. Therefore, if the transmitter and receiver are co-integrated on a single die, the overall transceiver performance can be further improved as much as the improved margin in the link power budget.

In Fig. 5-5(b), the BER performance of the coherent transmitter

EPIC is evaluated with the commercial coherent receiver in terms of OSNR in a 0.1 nm noise bandwidth, and theoretical BER values are also provided. The degradation of the transmitter EPIC is attributed to the thermal and wavelength sensitivity of the ring modulator, as described in [59,60].

Fig. 5-6 presents the recovered constellations and both channel's eye diagrams for points A, B, C and D of Fig. 5-5(a) as examples. All the data are color-coded based on their relative bin count, and the eye diagrams are re-sampled results. Data capacity can be further increased using 2-D grating couplers [93] for dual-polarizations, as already demonstrated in the receiver EPIC with the same technology [85].

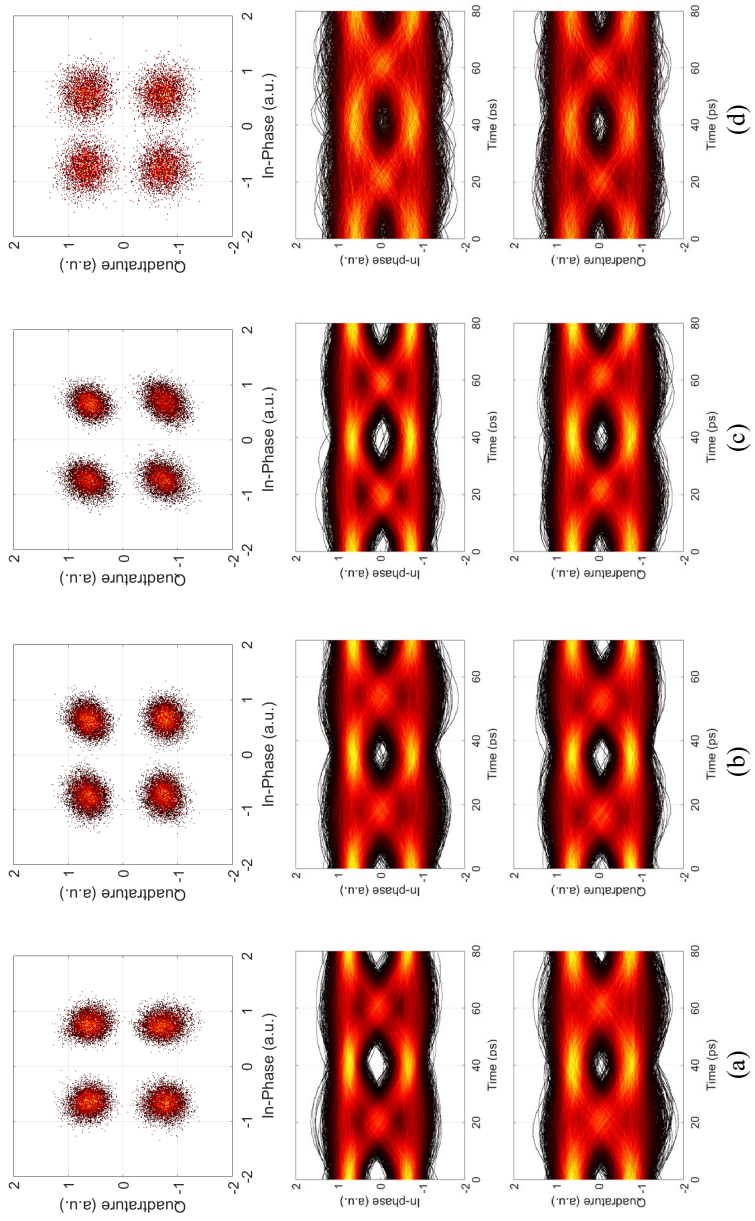

Fig. 5-6. Recovered constellations and eye diagrams for I-channel and Q-channel for the point (a) A, (b) B, (c) C and (d) D in Fig. 5-5(a) as examples. The eye diagrams have been resampled, and the data are color-coded to their relative bin count.

5.4. Performance Comparison

There have been many research efforts to integrate the Si RMs into coherent IQ modulators/transmitters. Table 5-1 presents reported coherent IQ modulators based on RMs.

In [59,60], a single-polarization QPSK modulator has been reported using the RaMZI structure for 28 Gbaud operation. However, it has a higher V_π of 6 V and a larger device footprint of 0.625 mm^2 compared to the coherent IQ modulator presented in this study. In [94], an ultra-compact coherent IQ modulator based on a push-pull configuration of a racetrack-RaMZI has been demonstrated single-polarization, a 124-Gbaud 4-level amplitude shift keying (ASK) within 0.03 mm^2. Nevertheless, the chip size excludes routing optical waveguides, and the modulator shows a higher V_π of 7.5 V and a higher insertion loss of approximately 18 dB. Another study, [95], reports a travelling wave Mach-Zehnder (TWMZ) racetrack ring modulator for 90-Gbaud dual-polarization (DP) probabilistically shaped (PS) 64-QAM operation. This modulator utilizes a coupling modulation in the directional coupler region, and it is hybrid-integrated with SiGe RF driver EIC through flip-chip ball grid array (BGA). However, due to its large TWMZ electrode-based design, the modulator occupies a footprint of 0.3 mm^2.

Furthermore, the transmitter in [95] demonstrated a higher V_π of 14 V and a higher insertion loss of 40.7 dB (including fiber-to-chip coupling loss). Notably, none of the previous reports provides precise and efficient characterization of RMs for phase modulation or detailed insights into design optimization.

Table 5-2 shows the performance comparison between the coherent transmitter and receiver EPICs in this study and other research regarding O-band transceiver links for intra-DC applications [96-98]. The transmitter has been realized through a hybrid integration with an MZM-based coherent IQ modulator and 90-nm BiCMOS driver electronics. Similarly, the receiver has been developed through a hybrid integration with a receiver PIC and a receiver EIC, which include an analog equalization based on an optical Costas phase-locked loop (PLL), distinct from off-line-DSP-based adaptive equalization. The demonstrated baud rate is 56-Gbaud DP-QPSK operation for the entire transceiver link and 64-Gbaud DP-QPSK operation for the transmitter only. Notably, the transmitter in [96-98] occupies 41.1 mm^2 due to its realization via "hybrid integration" and "MZM," while the coherent transmitter EPIC in this research is significantly smaller, occupying only 1.06 mm^2.

The coherent transmitter EPIC is further compared with a

commercial coherent IQ modulator [99]. This commercial modulator, fabricated using lithium niobate, demonstrates 64-Gbaud DP-QPSK operation for a 200-Gbps data rate and DP-16QAM operation for a 400-Gbps data rate. While numerous other commercial coherent IQ modulators exist, the majority are based on lithium niobate, which results in a larger device footprint.

	12' OL + 13'OFC [59,60]	23' SiPhotonics [94]	23' ECOC [95]	This Work
Process	Si Photonics	Si Photonics	Si Photonics + SiGe RF driver	**Si Photonic BiCMOS**
Wavelength	1550 nm	1550 nm	1550 nm	**1550nm**
Modulation Format	Single-pol. QPSK	Single-pol. 4-ASK	Dual-pol. 64-QAM	**Single-pol. QPSK**
Architecture	Modulator	Modulator	Transmitter	**Transmitter**
Demonstrated baud-rate	28-Gbaud	124-Gbaud	90-Gbaud	**28 Gbaud**
Electro-optic efficiency	~ 12 pm/V	~ 31.8 pm/V	N/A	**15.1 pm/V**
V_π	6 V	7.5 V	14 V	**5.7 V**
Insertion loss	10.5 dB (w/o coupling loss)	~ 18 dB (w/o coupling loss)	~ 40.7 dB (w/ coupling loss)	**15.3 dB (w/o coup. loss) 27.8 dB (w/ coup. loss)**
Driver Integration	X	X	O (Hybrid, flip-chip BGA)	**O (Monolithic)**
Device Structure	Ring-assisted MZI	Racetrack Ring-assisted MZI	MZ-assisted racetrack ring modulator	**Ring-assisted MZI**
Chip Size	0.625 mm^2	0.03 mm^2 (w/o routing waveguide)	Modulator: 0.3 mm^2 Driver: N/A	**Modulator: 0.16 mm^2 Tx: 1.06 mm^2**
Power Consumption	N/A	N/A	N/A	**986.3 mW (TO tuning 17.8 mW)**

Table 5-1. Performance comparison of the RM-based coherent IQ modulators/transmitters.

	23' JLT [96-98]	This Work
Process	Tx EIC: GF 9HP 90nm BiCMOS Rx EIC: GF 8XP 130nm BiCMOS PIC: Intel's Si Photonics	**IHP's Si Photonic BiCMOS**
Wavelength	1310 nm	**1550nm**
Modulation Format	Dual-pol. QPSK	**Single-pol. QPSK**
Architecture	Transceiver sub-assembly w/ analog equalization	**Transceiver sub-assembly**
Demonstrated baud-rate	Full transceiver: 56 Gbaud (Tx only: 64 Gbaud)	**Full transceiver: 28 Gbaud**
Driver Integration	O (Hybrid)	**O (Monolithic)**
Device Structure	MZM	**Ring-assisted MZI**
Chip Size	Tx: 41.4 mm^2 (*) Rx EIC: 5.2 mm^2 Rx PIC: N/A	**Tx: 1.06 mm^2 Rx: 5.49 mm^2**
Power Consumption	Tx: 1,200 mW Rx: 900mW	**Tx: 986.3 mW Rx: 518 mW**
Energy Efficiency	9.5 pJ/bit	**26.9 pJ/bit**

(*) Tx PIC includes semiconductor optical amplifier (SOA)

Table 5-2. Performance comparison of coherent transceiver sub-assembly.

	Coherent IQ Modulator Fujitsu FTM7992HM [99]	This Work
Process	Lithium Niobate	**IHP's Si Photonic BiCMOS**
Wavelength	1550 nm	**1550nm**
Modulation Format	Dual-pol. QPSK, Dual-pol. xQAM	**Single-pol. QPSK**
Architecture	Modulator	**Transmitter**
Maximum Baud-rate	64 Gbaud	**28 Gbaud**
Driving Voltage	N/A	**5.7 $V_{peak\text{-}to\text{-}peak}$**
Device Structure	MZM	**Ring-assisted MZI**
Device Footprint	81.7 x 12.5 x 6.5 mm^3	**1.06 mm^2**
Power Consumption	N/A	**986.3 mW**

Table 5-3. Performance comparison of the transmitter EPIC with a commercial coherent IQ modulator [99].

5.5. Summary

The detailed information about the measurements of the coherent transmitter EPIC with the coherent receiver EPIC is given. Due to the process variation in coherent IQ modulators based on the RaMZI, the heaters and phase shifters are integrated on the chip. The biases for these heaters and phase shifter are found by observing the measured transmission spectra to achieve the coincidence of resonance wavelengths of the two RMs and the 90-degree phase difference of the MZI.

To examine the potential of an all-silicon monolithic coherent transceiver based on EPIC, the fabricated transmitter EPIC is evaluated with a coherent receiver EPIC which has been realized within same photonic BiCMOS technology. The receiver EPIC includes optical components such as 4 x 4 MMI, Ge photodiodes as well as high-speed BiCMOS receiver front-end electronics such as TIAs, VGAs, output buffers and dc offset cancellation loops. The coherent transmitter EPIC consumes 986.3 mW for 28-Gbaud QPSK, while the coherent receiver EPIC consumes 518 mW for 28-Gbaud operation.

The coherent transceiver EPICs are measured together for 25-Gbaud and 28-Gbaud QPSK operation. The measured results of BER

with respect to ROP and OSNR are given, along with the recovered QPSK constellations and re-sampled eye diagrams. The proposed coherent transceiver sub-assembly has a potential for further improvements in integrated photonic BiCMOS technology. To assess the potential for high-speed DCI applications, another type of optical laser source, VCSEL, is used instead of the ECL for the signal source. In addition, the transceiver EPIC is measured for the case without using EDFA, showing the possibility of the inter-chip connection of the entire transceiver within a single die for the better performance with a more enough link power budget. The measured BER values are below the FEC limit, which confirms the successful operation for 25-Gbaud and 28-Gbaud QPSK signals for all the measurement configurations.

The demonstrated device is compared with the previously reported coherent IQ modulators/transmitter, coherent transceiver sub-assembly and commercial coherent modulator.

6. Discussion for Further Optimization

6.1. Further Optimization of Single RMs

The trade-offs in the phase modulation performance of single RMs for the single-quadrature modulators are discussed in Chapter 4.3, indicating that the RMs can have (i) a large modulation bandwidth, high V_π and low dynamic IL with a low Q factor, or (ii) a small modulation bandwidth, low V_π and high dynamic IL with a high Q factor as in Fig. 4-7. To achieve further optimized performances, such as low V_π, low dynamic IL or a larger modulation bandwidth, an analysis on the model parameters of single RMs is carried out regarding their impact on the design trade-offs.

Fig. 6-1 shows the design ranges of model parameters, τ_l and τ_e, based on the structure parameters of RMs such as radius and coupling gap. To obtain these, the device simulation has been carried out using Ansys Lumerical DEVICE, MODE and FDTD. The parameter ranges shown in the design optimization in Chapter 4.3 consider the maximum output voltage (6 $V_{peak\text{-}to\text{-}peak}$) of the BiCMOS driver electronics as the design limit. As shown in Fig. 6-1, for the given radius of RM, the value of τ_l is determined, and for the smaller coupling gap design, the

lower τ_e can be obtained. This implies the potential for further RM optimization towards a larger modulation bandwidth, lower dynamic IL and lower Q factor, as seen in Fig. 4-7, but at the same time, it also implies a significantly higher V_π reaching 9 $V_{peak\text{-}to\text{-}peak}$.

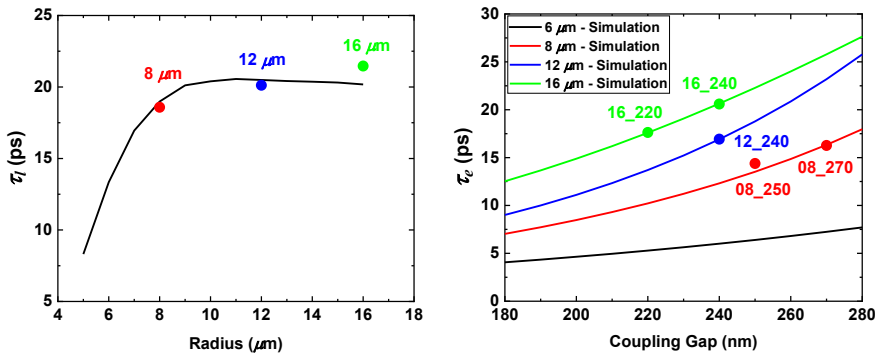

(a) (b)

Fig. 6-1. Design ranges of the RM's model parameters: (a) τ_l vs radius and (b) τ_e vs coupling gap, radius. Colored dots indicate the measured sample RMs in Chapter 4.3.

Then, the trade-offs in RM model parameters over a wider range must be explored beyond the limit of the driver electronics' maximum output peak-to-peak voltage. Fig. 6-2 shows the 3-dB E/O bandwidth, dynamic insertion loss, and Q factor in terms of the wider range of RM's model parameters. The data presented in Fig. 6-2 is the simulated result using the characterization and optimization method demonstrated

in Chapter 4. "Design limit" denotes the model parameter range achievable with the 6 $V_{peak\text{-}to\text{-}peak}$ limit, emphasized previously. The results within a wider model parameter range in Fig. 6-2 indicate the possibility of designing RMs for a larger modulation bandwidth (~ 35 GHz), lower dynamic IL (~ 5 dB) and lower Q factor (~ 3300), compared to Fig. 4-7.

Particularly, a higher 3-dB bandwidth can be obtained with smaller values of τ_l and τ_e at the same driving voltages, as the bandwidth is less limited with smaller values of these time constants. Similarly, a lower Q factor is achievable with smaller τ_l and τ_e values, indicating higher loss. Decreasing τ_e causes the RM to move away from critical coupling, resulting in a smaller dynamic insertion loss. As illustrated in Fig. 6-1, smaller values of τ_l and τ_e are related to smaller radius and coupling gap, respectively. However, the lines indicating 9- and 12-$V_{peak\text{-}to\text{-}peak}$ levels imply a need for significantly higher driving voltages to achieve V_π.

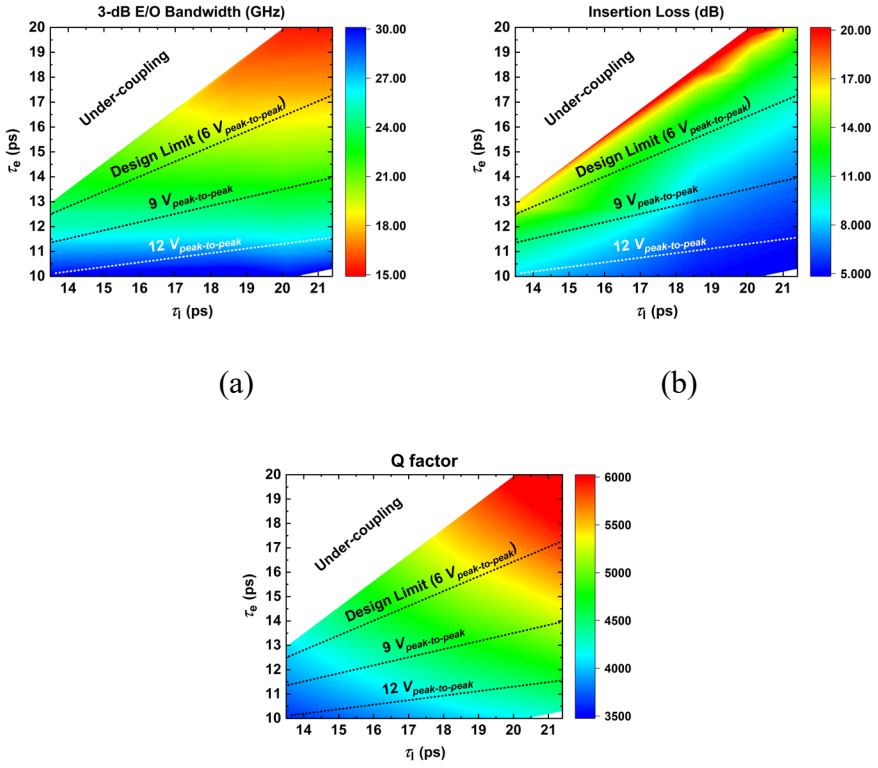

Fig. 6-2. Further optimization of single RM's performance for wider ranges of τ_l and τ_e at 0 V. (a) 3-dB E/O bandwidth in GHz, (b) dynamic insertion loss in dB and (c) Q factor. The lines in the figure show the required driving voltages in $V_{peak\text{-}to\text{-}peak}$.

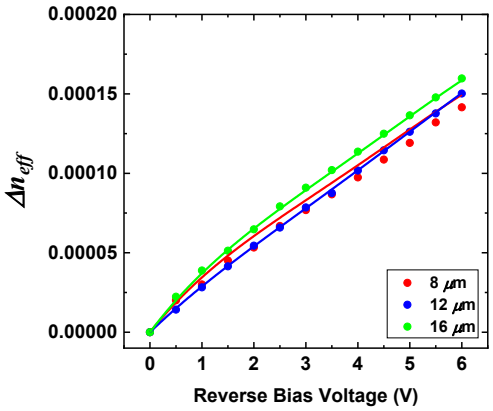

Fig. 6-3. Measured and fitted electro-optic efficiency (Δn_{eff} vs reverse bias voltage) of the RMs for 8-, 12- and 16-μm radius.

Fig. 6-3 shows the measured and fitted electro-optic (E/O) efficiency of the fabricated sample RMs, represented as Δn_{eff} versus the reverse bias voltage. For instance, 16-μm radius RMs have a corresponding value of 15.1 pm/V for $\Delta\lambda_{res}$/V from 0 V to 6 V. The free-carrier-based Si optical modulators shows low E/O efficiency for a high reverse bias due to the p-n diode's nonlinear effect. Thus, achieving a high V_{π}, such as 12 $V_{peak\text{-}to\text{-}peak}$ as in Fig. 6-2 or 14 $V_{peak\text{-}to\text{-}peak}$ in [95], would not only be challenging for the devices but also impose high power consumption burdens on electronic driver ICs or external electrical amplifiers.

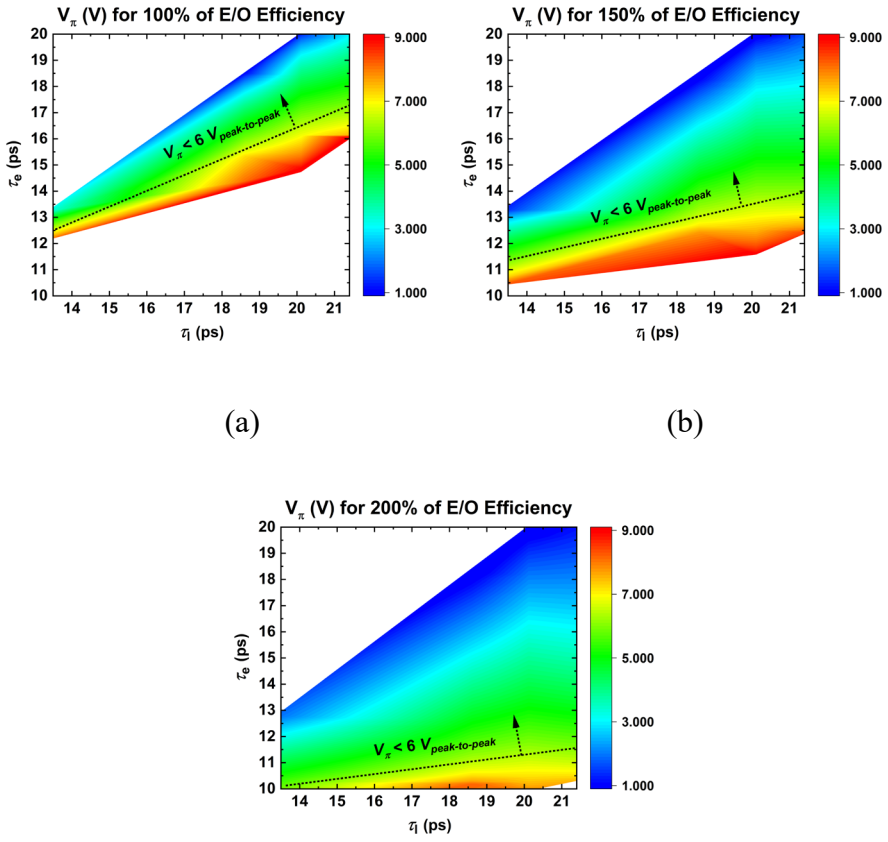

(a) (b)

(c)

Fig. 6-4. Required V_π for the single RMs when the E/O efficiency is assumed to be (a) 100%, (b) 150% and (c) 200% of the measured and fitted results in Fig. 6-3.

Fig. 6-4 shows the simulated V_π in terms of the wider range of RM's model parameters, with 150% and 200% of E/O efficiencies assumed, and it also shows the case of 100% from Fig. 4-7(b) for comparison. The E/O efficiency curves are derived from Fig. 6-3 for the behavioral

simulations. The case of E/O efficiency of 200% indicates that a wider design range of RM model parameters can be covered with lower driving voltages. For instance, when the 200% of E/O efficiency is assumed, the 16-μm radius RMs can have 30.2 pm/V for a resonance modulation efficiency which is a similar value of [94] in Table 5-1. Then, the RMs within the model parameter ranges of 12 $V_{peak\text{-}to\text{-}peak}$ in Fig. 6-2 can be realized with 6 $V_{peak\text{-}to\text{-}peak}$, potentially resulting in higher E/O bandwidth and lower insertion loss than the optimized results in Chapter 4.

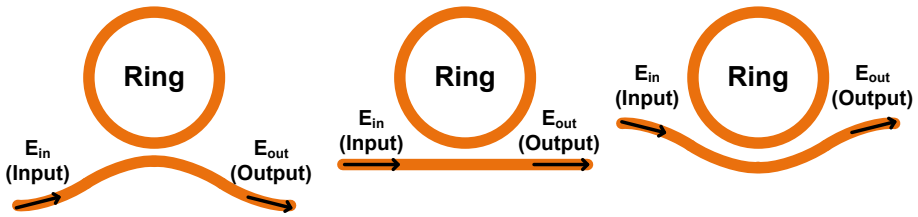

(a) (b) (c)

Fig. 6-5. Different and possible designs of the directional coupler for the RMs, (a) convex to the ring, (b) straight and (c) concave to the ring.

The improved E/O efficiency of the p-n diode is feasible through optical mode overlap optimization such as L-shaped junction [74], and ion implantation engineering for higher carrier concentration. However,

this has a possibility of changing the optical loss coefficient which results in change of the RM's model parameters, τ_l (α). Thus, for the similar desired performance, τ_e (γ) may need potential design compensation procedures by controlling the coupling gap in directional coupler design or the waveguide shape of directional couplers such as straight or concave, convex to the RMs as shown in Fig. 6-5. Furthermore, the RC bandwidth of RMs can have different aspects due to the p-n diode optimization unlike discussed in Chapter 3.4 and 4.3, and in this case, the carrier concentration and physical dimension of the waveguide slab region can be controlled to prevent a decrease in the RC bandwidth.

6.2. Alternatives for Single-Quadrature Modulators

In the previous chapter, the phase-modulation performance of a single RM has been further optimized by considering a wider range of model parameters and better E/O efficiency of the p-n diode of RMs. However, the optimized 3-dB E/O bandwidth remains around 35 GHz due to the single RM's near-zero detuning operation, as illustrated in Fig. 3-5, where the bandwidth of RM is highly limited. Achieving a 3-dB E/O bandwidth exceeding 35 GHz is challenging with near-zero detuning operation. Therefore, an alternative driving scheme for the RaMZI is analyzed to enhance the phase modulation performance for a single-quadrature modulator.

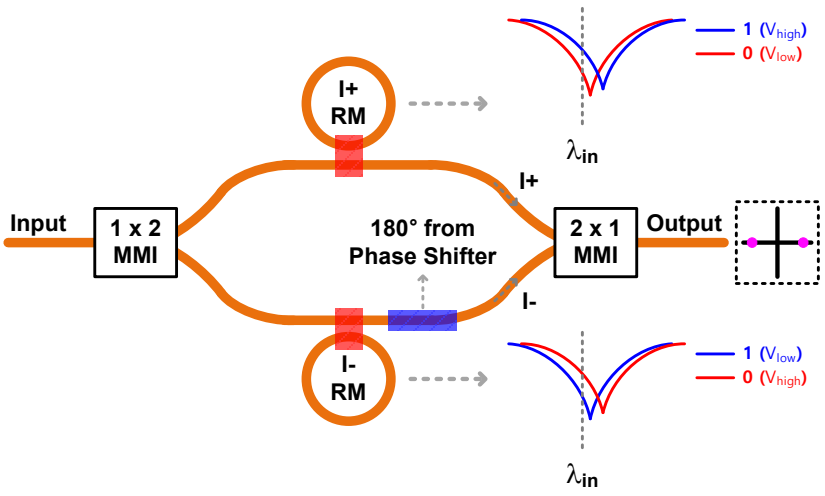

Fig. 6-6. Push-pull configuration of the RaMZI for a single-quadrature modulator.

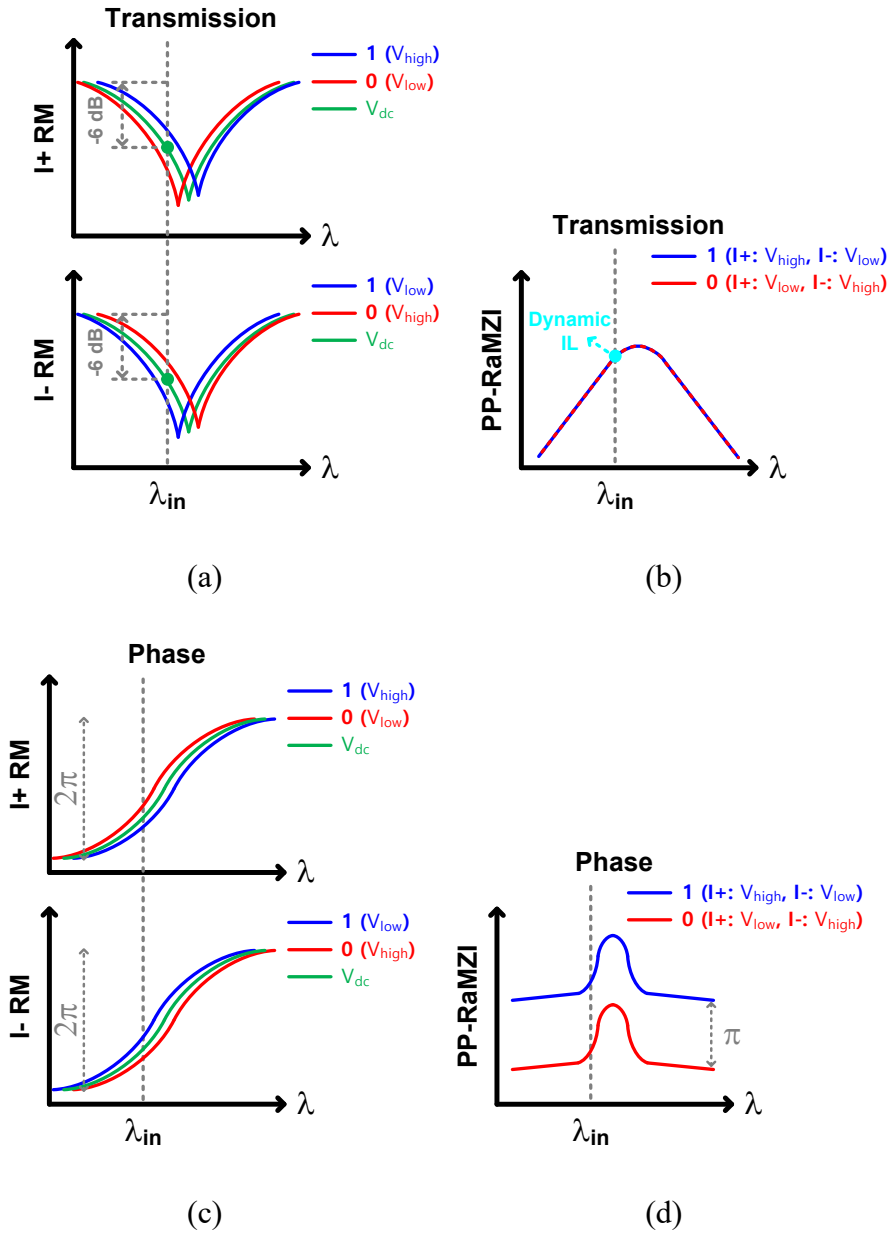

Fig. 6-7. Operation principle of PP-RaMZI, (a) transmission of I+ and I- RMs, (b) transmission of the PP-RaMZI (c) phase of I+ and I- RMs and (d) phase of the PP-RaMZI.

Fig. 6-6 illustrates a push-pull configuration of RaMZI (PP-RaMZI) integrating two RMs in each arm of the MZI. The physical structure is similar to the RM-based coherent IQ modulators in Fig. 4-1, yet different in that the upper RM and lower RM represent I+ and I- signals, respectively. For instance, when the I+ RM is supplied with V_{low} for bit 0 and V_{high} for bit 1, the inverse signal of them is supplied to the I- RM. In the PP-RaMZI configuration, a π-phase shift is introduced by the phase shifter integrated into one of the MZI's arms. Thanks to the π-phase shift originating from the phase shifter, the single-quadrature modulator gains a degree of freedom (V_{π}) among the trade-off relations, previously represented by V_{π}, insertion loss, and 3-dB bandwidth. Additionally, the single RM, operating as a single-quadrature modulator, suffers from bandwidth limitations due to near-zero detuning operation as depicted in Fig. 3-5. However, the PP-RaMZI offers the possibility to choose detuning far from the resonance, enabling a larger modulation bandwidth.

Fig. 6-7 illustrates the detailed operation principle of the PP-RaMZI. In Fig. 6-7(a), the transmission spectra for I+ and I- RMs are given. These RMs operate with a push-pull configuration based on given bit data. The operation wavelength (λ_{in}) is determined to have a DC insertion loss of 6 dB, as this point is known to offer optimal high-

speed modulation characteristics in many previous reports [57,74]. Fig. 6-7(b) illustrates the transmission of the entire PP-RaMZI for 0 and 1 operations. Due to the π-phase shift, the transmission spectra have different shapes from notch filter characteristics. The figure implies that insertion loss can have different values in terms of λ_{in}. Fig. 6-7(c) illustrates the phase spectra for I+ and I- RMs with the push-pull operation, and the resulting phase spectra for the PP-RaMZI are shown in Fig. 6-7(d), confirming the acquisition of the π-phase shift by the integrated phase shifter.

For a comprehensive analysis, the performance of the PP-RaMZI is simulated using the model parameters of the "16_220" RM integrated into the coherent transmitter EPIC in this research. A driving voltage of 2 $V_{peak\text{-}to\text{-}peak}$ is supplied to each RM, which is equivalent to a total of 4 $V_{peak\text{-}to\text{-}peak}$ for the PP-RaMZI. The simulated results of the PP-RaMZI, along with those of the single RM for comparison, are presented in Fig. 6-8. Fig. 6-8(a) shows the transmission spectra of the PP-RaMZI which has a dynamic insertion loss of 12.0 dB at λ_{in}. In contrast, the dynamic insertion loss for the single RM is 10.0 dB where two transmissions cross. Fig. 6-8(b) shows the phase difference spectra for the PP-RaMZI and the single RM. The PP-RaMZI's phase difference is flatter than that of the single RM, owing to the π-phase shift from the phase shifter

rather than the device itself, enabling more tolerant phase modulation operation at the input wavelength, λ_{in}.

Fig. 6-8(c) presents the simulated E/O responses of the PP-RaMZI and the single RM. Despite a slight peaking in the response, the PP-RaMZI shows a larger bandwidth of 28.0 GHz compared to the 18.2 GHz bandwidth of the single "16_220" RM. The bandwidth of RMs can be further increased by adjusting λ_{in} to move farther from the resonance, resulting in a lower DC insertion loss. Fig. 6-8(d) shows the simulated E/O responses when λ_{in} values for the PP-RaMZI are set to have DC insertion losses of 3 dB and 6 dB. As a result, the bandwidth increases to 41.4 GHz for a 3-dB DC insertion loss. However, the dynamic insertion loss is also increased to 15.4 dB because of decreased output optical modulation amplitude for λ_{in} far from the resonance. Even though there is more peaking in the response, this characteristic can be helpful in compensating the potential RC bandwidth limitation of RM for high-speed operation.

By integrating the PP-RaMZI as a single-quadrature modulator, the performance such as driving voltages and 3-dB modulation bandwidth can be improved at the cost of the increased dynaminc insertion loss. The performance of the PP-RaMZI and single RM is summarized in Table 6-1.

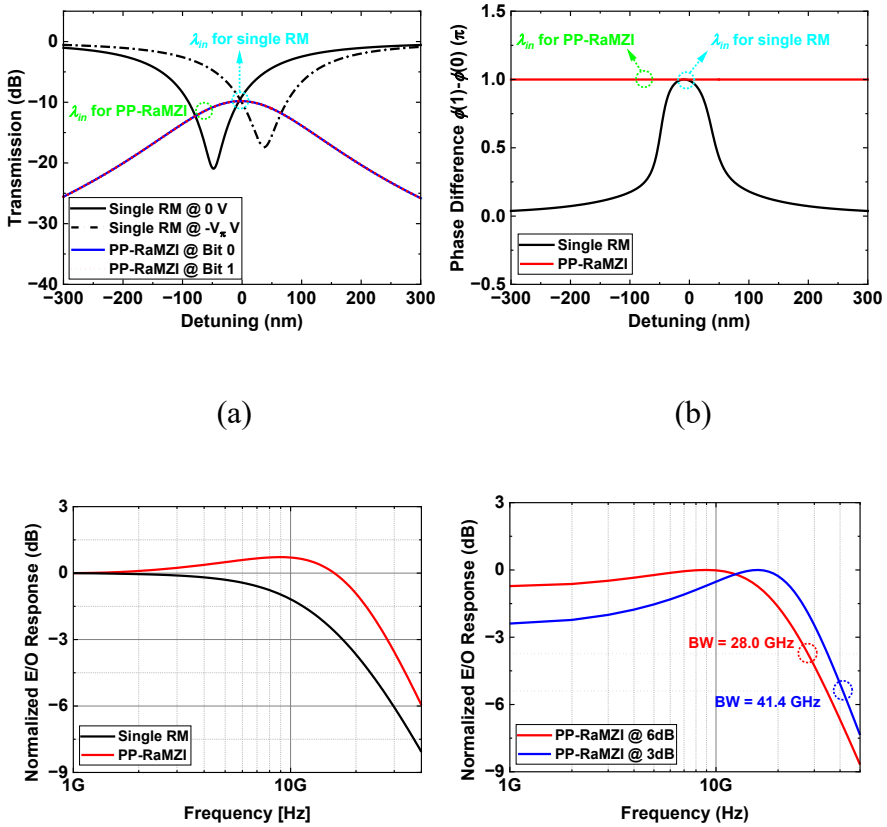

Fig. 6-8. Simulated (a) transmission spectra, (b) phase difference between "bit 1" and "bit 0", and (c) E/O response of the PP-RaMZI with "16_220" RMs for a single-quadrature modulator. (d) E/O responses of the PP-RaMZI for λ_{in} having a 3-dB and 6-dB DC insertion loss. The simulated results of "16_220" single RM for the single-quadrature modulator are also shown for comparison.

Device	"16_220"	***"16_220"***	
Configuration	Single RM	***PP-RaMZI***	
λ_{in}	@ π-phase shift	***@ DC insertion loss = -6 dB***	***@ DC insertion loss = -3 dB***
$V_{peak\text{-}to\text{-}peak}$ (V)	5.65	***2***	***2***
Dynamic insertion loss (dB)	10.1	***12.0***	***15.4***
3-dB E/O bandwidth (GHz)	18.2	***28.0***	***41.4***

Table 6-1. Simulated performance metrics of the PP-RaMZI and single RM based on the model parameters of "16_220" RM.

As in Chapter 4.3 and Chapter 6.1, the trade-offs of PP-RaMZI with RM model parameters are explored. Fig. 6-9 presents the simulated performance of PP-RaMZI, where each RM is supplied with a 2 $V_{peak\text{-}to\text{-}peak}$ driving voltage, assuming 100% of E/O efficiency. The model parameter ranges are consistent with those shown in Fig. 6-2. Fig. 6-9(a) and (b) respectively show the 3-dB E/O bandwidth and dynamic insertion loss when λ_{in} is set to have a 6-dB DC insertion loss for individual RMs. Smaller values of τ_l and τ_e allow the RM to have a higher modulation bandwidth exceeding 35 GHz, albeit at the cost of increased dynamic loss. To achieve even higher modulation bandwidth, the value of λ_{in} can be adjusted to have a 3-dB DC insertion loss for the individual RMs. This results in the 3-dB E/O bandwidth and dynamic insertion loss shown in Fig. 6-9(c) and (d), respectively. In the figure,

the PP-RaMZI demonstrates its possibility to have a modulation bandwidth of over 65 GHz with a corresponding increased dynamic insertion loss of around 19.0 dB.

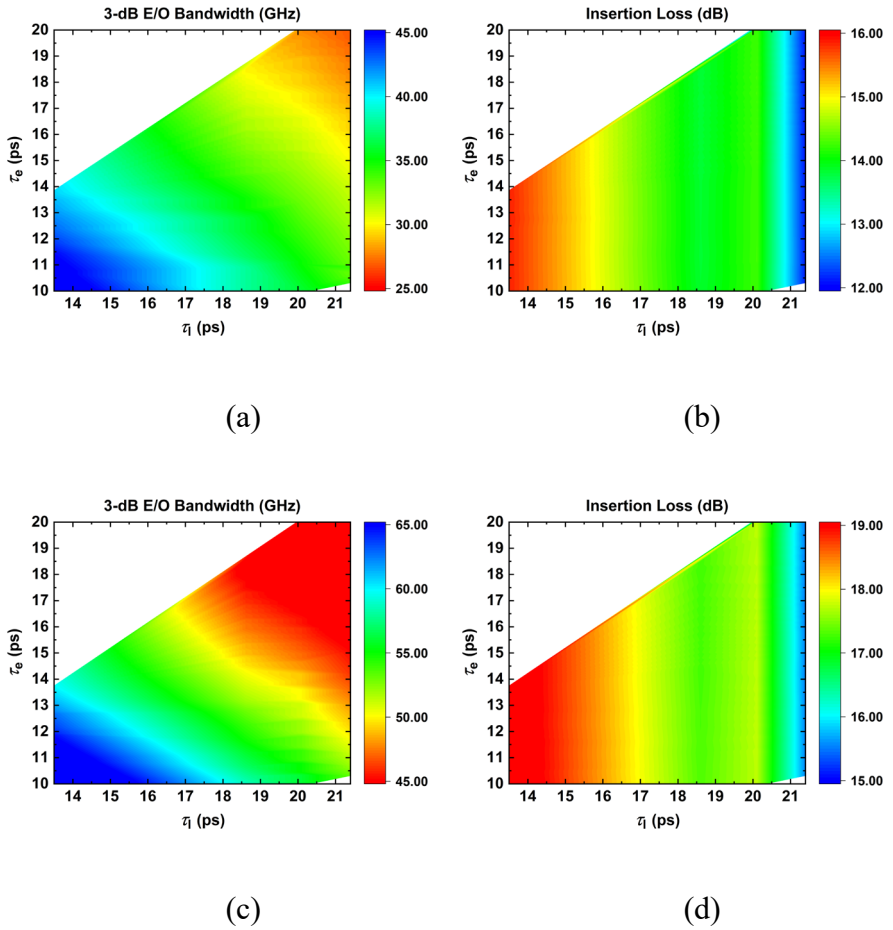

Fig. 6-9. Optimization of the PP-RaMZI's performance in terms of wider ranges of τ_l and τ_e at 0 V with 2 $V_{peak\text{-}to\text{-}peak}$ driving voltage and 100% of E/O efficiency assumed. (a) 3-dB E/O bandwidth in GHz and (b) dynamic insertion loss in dB for λ_{in} at 6-dB DC insertion loss. (c) 3-dB E/O bandwidth in GHz and (d) dynamic insertion loss in dB for λ_{in} at 3-dB DC insertion loss.

The increased dynamic insertion loss observed at 3-dB DC insertion loss comes from the smaller dynamic optical output. To overcome this, the E/O efficiency is assumed to be 200%. Fig. 6-10 (a) and (b) show the dynamic insertion loss when 200% E/O efficiency is assumed at 6-dB and 3-dB DC insertion loss, respectively. Compared to the 100% E/O efficiency case in Fig. 6-9, the 6-dB margin of dynamic insertion loss can be achieved with 200% E/O efficiency.

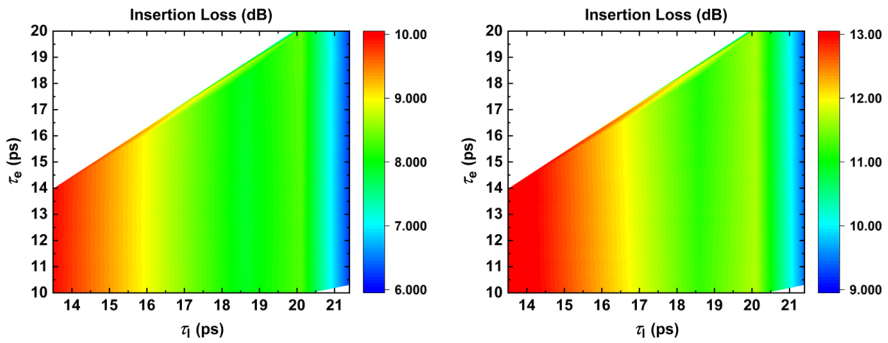

(a) (b)

Fig. 6-10. Dynamic insertion loss of the PP-RaMZI with 2 $V_{peak\text{-}to\text{-}peak}$ driving voltage and 200% of E/O efficiency assumed. Dynamic insertion loss for (a) λ_{in} at 6-dB DC insertion loss and (b) λ_{in} at 3-dB DC insertion loss.

The PP-RaMZI enables higher modulation bandwidths for single-quadrature modulators with a lower driving voltage of 2 $V_{peak\text{-}to\text{-}peak}$,

reducing power consumption of BiCMOS driver electronics. Non-zero detuning, such as 3- and 6-dB DC insertion loss, alleviates bandwidth limitations resulting from near-zero detuning operation in the case of single RM for a single-quadarature modulator. Additionally, the increased dynamic insertion loss can be mitigated with higher E/O modulation efficiency, providing a 6-dB margin for dynamic insertion loss with 200% E/O efficiency. Table 6-2 summarizes the optimized performance of the PP-RaMZI for 2 $V_{peak\text{-}to\text{-}peak}$ driving voltages, having 13.34 ps of τ_l and 8.80 ps of τ_e.

Configuration	PP-RaMZI			
τ_l (ps)	13.34			
τ_e (ps)	8.80			
$V_{peak\text{-}to\text{-}peak}$ (V)	2			
E/O modulation efficiency	***100%***		***200%***	
λ_{in}	***@ DC IL = -6 dB***	***@ DC IL = -3 dB***	***@ DC IL = -6 dB***	***@ DC IL = -3 dB***
Dynamic insertion loss (dB)	***15.93***	***19.39***	***10.02***	***13.39***
3-dB E/O bandwidth (GHz)	***50***	***74.5***	***50***	***74.5***

Table 6-2. Optimized performance of PP-RaMZI with 13.34 ps of τ_l and 8.80 ps of τ_e.

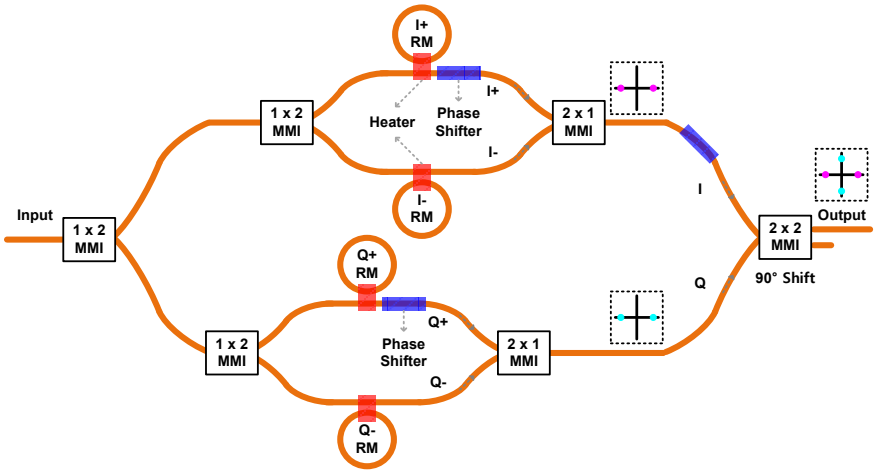

Fig. 6-11. Schematic of coherent IQ modulator with two PP-RaMZIs for I and Q channel.

Fig. 6-11 illustrates the schematic of a coherent IQ modulator with two PP-RaMZIs, each operating as a single-quadrature modulator for the I or Q channel. The input optical signal is divided by 1 x 2 MMI and delivered to each PP-RaMZI. The phase-modulated signals generated for the I and Q channels are then combined using a 2 x 2 MMI, introducing a 90° phase shift.

Because it is composed of 4 RMs, 2 sub-MZIs and 1 main-MZI, compensation for process variations of the RMs and MZIs is essential and can be achieved using integrated heaters and phase shifters, as discussed in Chapter 5.1. An automated bias controller can be used to align the resonances of the RMs and the phase of the MZI. Various bias controllers for RMs have been demonstrated to stabilize the RM's

operation in terms of input wavelength, optical power and temperature for both coherent transceivers [95] and IM/DD transceivers [100] applications. Leveraging the BiCMOS electronic process, a built-in temperature controller for the RMs can be realized within the coherent transmitter EPIC, as demonstrated previously for NRZ operation [68].

6.3. Expansion to Quadrature-Amplitude Modulation

To enhance the data capacity of the coherent modulator/transmitter, further optimizations considering device characteristics and driving schemes have been analyzed and proposed. Along with the improved device performance and alternative architectures, expandability towards higher-order coherent modulation, such as quadrature-amplitude modulation (QAM), is explored. As depicted in Fig. 6-12, the 16-QAM signals can be generated by the single-quadrature modulators for each I/Q channel, producing 4-level amplitude shift keying (ASK) signals, which are then combined to have 16 symbols with the combination of 4 symbols from each channel.

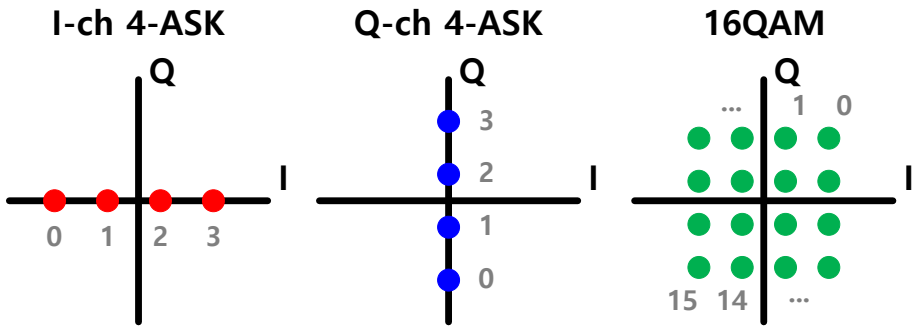

Fig. 6-12. Composition of 16-QAM signal's constellation.

For an application of RMs for QAM operation, the constellations of

coherent IQ modulator based on the RMs are simulated using the model parameters of "16_220" RMs. Two types of coherent IQ modulators were compared: one using a single RM for a single-quadrature modulator, which has been demonstrated as the coherent transmitter EPIC in this research (Fig. 4-1) utilizing the RaMZI for IQ modulation, and the other using the PP-RaMZI for a single-quadrature modulator analyzed in Chapter 6.2, utilizing two PP-RaMZIs for IQ modulation as depicted in Fig. 6-11. For the case of PP-RaMZI, 2 $V_{peak\text{-}to\text{-}peak}$ of driving voltage is used, and λ_{in} is set to have a 6-dB DC insertion loss.

Fig. 6-13 shows the simulated constellations using the RaMZI and the PP-RaMZI. Fig. 6-13(a) and (b) show the single-quadrature constellations for the 4-ASK signal with single RM and PP-RaMZI, respectively. The trajectory of symbols in Fig. 6-13(a) is observed to be bent, while Fig. 6-13(b) shows a linear trajectory of symbols. The RMs have the nonlinear modulation characteristics due to the inherent notch characteristics and the p-n diode, with the highest SFDR values observed at λ_{in} far from the resonance, as discussed in Chapter 3.5. Moreover, the single RM for single-quadrature operates with near-zero detuning, resulting in the lowest SFDR values, leading to the bent trajectory in Fig. 6-13(a). However, in the case of PP-RaMZI, since the values of λ_{in} are distant from the resonances, and the nonlinearities of

I+ and I- RMs for the PP-RaMZI counterbalance each other, a more linear trajectory is observed as in Fig. 6-13(b). The 16-QAM constellations with the single RM and PP-RaMZI are given in Fig. 6-13(c) and (d), and the 64-QAM constellations with the single RM and PP-RaMZI are also given in Fig. 6-13(e) and (f), confirming the PP-RaMZI as a more promising building block for RMs to the coherent IQ modulator applications with higher-order modulation formats.

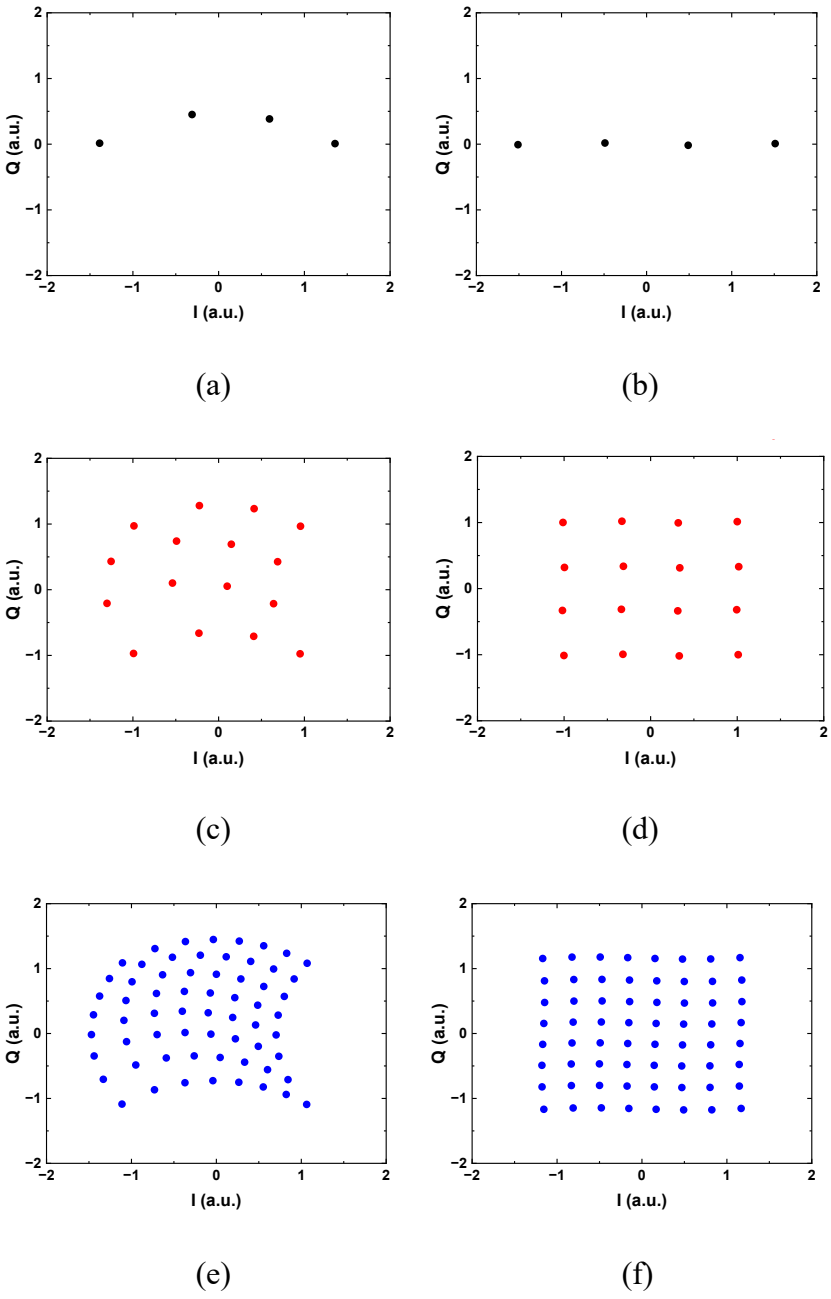

Fig. 6-13. 4-ASK constellation with (a) single RM and (b) PP-RaMZI. 16-QAM constellation with (c) single RM and (d) PP-RaMZI. 64-QAM constellation with (e) single RM and (f) PP-RaMZI.

6.4. Summary

The performance enhancement of coherent IQ modulators and transmitters can be achieved through several proposed aspects: (i) optimizing devices with respect to the model parameters and E/O efficiency, (ii) exploring alternative driving schemes and structures using two PP-RaMZI for IQ modulation and (iii) expanding to higher-order coherent modulation formats.

A more detailed analysis of the trade-offs related to the single RMs for single-quadrature modulators is given in terms of modulation bandwidth, V_π, dynamic insertion loss, and Q factor based on a wider range of model parameters and improved E/O efficiency. By reducing τ_l and τ_e values, representing smaller radius and coupling gap, improved RM performance for phase modulation can be achieved.

The alternative driving scheme of RaMZI, referred to as PP-RaMZI, has been introduced and investigated for single-quadrature operation. The PP-RaMZI operates with a π-phase shift from the integrated phase shifter rather than the RM itself, offering increased design flexibility among the trade-offs. Non-zero detuning alleviates bandwidth limitations by allowing a wider selection of the operation wavelength, albeit at the expense of higher dynamic insertion loss. Integration of

two PP-RaMZI for IQ modulation significantly enhances performance as a coherent IQ modulator.

The improved coherent IQ modulators enable higher data capacity through the expansion to higher-order modulations such as 16- and 64-QAM. To assess their potential, simulated constellations are provided for 4-ASK, 16-QAM and 64-QAM, comparing the performance between single RMs and PP-RaMZI operating as a single-quadrature modulator.

7. Conclusion

In this dissertation, the coherent transmitter electronic-photonic integrated circuit fabricated by IHP's photonic BiCMOS process is demonstrated. The device is realized with the ring modulators, which have high-energy efficiency, small device footprint and high modulation bandwidth. For a realization of an efficient coherent transmitter, the basic operation principle, the modulation linearity and the complex electro-optic modulation frequency responses are characterized and optimized when the ring modulator is phase modulated. The fabricated coherent transmitter is assessed with the coherent receiver electronic-photonic integrated circuit realized within the same photonic BiCMOS process. The measured results indicate that the coherent transmitter operates for 25-Gbaud and 28-Gbaud QPSK signals, and for the different optical laser sources and the case without an optical amplification. Based on the verified characterization method, the performance of the coherent modulator and transmitter is further optimized through the implementation of various techniques.

As can be seen in this dissertation, the monolithic coherent transmitter based on the ring modulators provides the high modulation performance within the compact device size, showing a great potential

as an all-silicon monolithic coherent transceiver sub-assembly for high-speed data center applications.

Bibliography

[1] Worlds Top Data Centers. 2023. “WORLD’S LARGEST DATA CENTER: CHINA TELECOM INNER MONGOLIA PARK.” https://worldstopdatacenters.com/china-telecom-inner-mongolia-information-park.

[2] Cisco Systems, Inc. 2023. “Scaling the Internet for the Future With 800G Innovations.” https://blogs.cisco.com/sp/scaling-the-internet-for-the-future-with-800g-innovations.

[3] Jones, Nicola. "How to stop data centres from gobbling up the world’s electricity." Nature 561.7722 (2018): 163-166.

[4] Dayarathna, Miyuru, Yonggang Wen, and Rui Fan. 2016. “Data Center Energy Consumption Modeling: A Survey.” *IEEE Communications Surveys and Tutorials* 18 (1): 732–94.

[5] Cisco Systems, Inc. 2021. “Co-Packaged Optics and an Open Ecosystem.” https://blogs.cisco.com/sp/co-packaged-optics-and-an-open-ecosystem.

[6] Intel Corporation, 2005. “Silicon Photonics Vision 2005.” https://www.intel.com/content/dam/www/public/us/en/documents/technology-briefs/intel-labs-hybrid-silicon-laser-announcement.pdf

[7] Bogaerts, Wim, Roel Baets, Pieter Dumon, Vincent Wiaux, Stephan Beckx, Dirk Taillaert, Bert Luyssaert, Joris Van Campenhout, Peter Bienstman, and Dries Van Thourhout. 2005. “Nanophotonic Waveguides in Silicon-on-Insulator Fabricated with CMOS Technology.” Journal of Lightwave Technology 23 (1): 401–12.

[8] Reed, G. T., G. Mashanovich, F. Y. Gardes, and D. J. Thomson. “Silicon Optical Modulators.” *Nature Photonics* 4, 518–526 (2010).

[9] Lischke, S., A. Peczek, J. S. Morgan, K. Sun, D. Steckler, Y. Yamamoto, F. Korndörfer, et al. 2021. “Ultra-Fast Germanium Photodiode with 3-DB Bandwidth of 265 GHz.” *Nature Photonics* 15 (12): 925–31.

[10] Shen, Yiwen, Xiang Meng, Qixiang Cheng, Sebastien Rumley, Nathan Abrams, Alexander Gazman, Evgeny Manzhosov, Madeleine Strom Glick, and Keren Bergman. 2019. “Silicon Photonics for Extreme Scale Systems.” *Journal of Lightwave Technology* 37 (2): 245–59.

[11] Liao, Ling, Saeed Fathololoumi, Kimchau Nguyen, Hari Mahalingam, David Hui, John Heck, Harel Frish, et al. “Silicon Photonics for Next-Generation Optical Connectivity.” 2023 *Optical Fiber Communications Conference and Exhibition (OFC)*. IEEE, 2023.

[12] Claes, Tom, Jordi Gironès Molera, Katrien De Vos, Etienne Schacht, Roel Baets, and Peter Bienstman. 2009. “Label-Free Biosensing with a Slot-Waveguide-Based Ring Resonator in Silicon on Insulator.” *IEEE Photonics Journal* 1 (3): 197–204.

[13] Densmore, Adam, D. X. Xu, P. Waldron, S. Janz, P. Cheben, J. Lapointe, A. Delâge, B. Lamontagne, J. H. Schmid, and E. Post. 2006. “A Silicon-on-Insulator Photonic Wire Based Evanescent Field Sensor.” *IEEE Photonics Technology Letters* 18 (23): 2520–22.

[14] Komljenovic, Tin, Roger Helkey, Larry Coldren, and John E. Bowers. 2017. “Sparse Aperiodic Arrays for Optical Beam Forming and LIDAR.” *Optics Express* 25 (3): 2511.

[15] Poulton, Christopher V., Ami Yaacobi, David B. Cole, Matthew J. Byrd, Manan Raval, Diedrik Vermeulen, and Michael R. Watts. 2017. “Coherent Solid-State LIDAR with Silicon Photonic Optical Phased Arrays.” *Optics Letters* 42 (20): 4091.

[16] Marpaung, David, Jianping Yao, and José Capmany. 2019. “Integrated Microwave Photonics.” *Nature Photonics*. Nature Publishing Group.

[17] Qiang, Xiaogang, Xiaoqi Zhou, Jianwei Wang, Callum M. Wilkes, Thomas Loke, Sean O’Gara, Laurent Kling, et al. 2018. “Large-Scale Silicon Quantum Photonics Implementing Arbitrary Two-Qubit Processing.” *Nature Photonics* 12 (9): 534–39.

[18] Shastri, Bhavin J., Alexander N. Tait, T. Ferreira de Lima, Wolfram H.P. Pernice, Harish Bhaskaran, C. D. Wright, and Paul R. Prucnal. 2021. “Photonics for Artificial Intelligence and Neuromorphic Computing.” *Nature Photonics*. Nature Research.

[19] Hochberg, Michael, and Tom Baehr-Jones. 2010. “Towards Fabless Silicon Photonics.” *Nature Photonics*.

[20] Rickman, Andrew. 2014. “The Commercialization of Silicon Photonics.” *Nature Photonics*. Nature Publishing Group.

[21] Siew, S. Y., B. Li, F. Gao, H. Y. Zheng, W. Zhang, P. Guo, S. W. Xie, et al. 2021. “Review of Silicon Photonics Technology and Platform Development.” *Journal of Lightwave Technology*. Institute of Electrical and Electronics Engineers Inc.

[22] Lischke, Stefan, Dieter Knoll, Christian Mai, and Lars Zimmermann. “Advanced Photonic BiCMOS Technology with High-Performance Ge Photo Detectors.” *Optical Sensing, Imaging, and Photon Counting: From X-Rays to THz 2019.* Vol. 11088. SPIE, 2019.

[23] “Silicon photonic ICs for prototyping - Imec.” Accessed: May 08, 2020. [Online]. https://www.imec-int.com/en/siliconphotonic-ICs-prototyping

[24] Giewont, Ken, Karen Nummy, Frederick A. Anderson, Javier Ayala, Tymon Barwicz, Yusheng Bian, Kevin K. Dezfulian, et al. 2019.

"300-mm Monolithic Silicon Photonics Foundry Technology." *IEEE Journal of Selected Topics in Quantum Electronics* 25 (5).

[25] Yole Group. 2022. "Silicon photonics: to SOI and beyond!" https://www.yolegroup.com/press-release/silicon-photonics-to-soi-and-beyond.

[26] Intel Corporation, 2020. "Silicon Photonics 400G DR4 QSFP-DD Transceiver." https://www.intel.com/content/www/us/en/architecture-and-technology/silicon-photonics/400g-dr4-qsfp-dd-optical-transceiver.html.

[27] Cisco Systems, Inc. 2023. "Cisco Silicon One Breaks the 51.2 Tbps Barrier." https://blogs.cisco.com/sp/cisco-silicon-one-breaks-the-51-2-tbps-barrier.

[28] Kikuchi, Kazuro. 2016. "Fundamentals of Coherent Optical Fiber Communications." *Journal of Lightwave Technology*. Institute of Electrical and Electronics Engineers Inc.

[29] Zhou, Xiang, Ryohei Urata, and Hong Liu. 2020. "Beyond 1 Tb/s Intra-Data Center Interconnect Technology: IM-DD or Coherent?" *Journal of Lightwave Technology* 38 (2): 475–84.

[30] Perin, Jose Krause, Anujit Shastri, and Joseph M. Kahn. 2021. "Coherent Data Center Links." *Journal of Lightwave Technology* 39 (3): 730–41.

[31] Zhou, Jianying, and Qun Zhang. 2022. "Multiple Tb/s Coherent Optical Transceivers for Short Reach Interconnect." *IEEE Journal of Selected Topics in Quantum Electronics* 28 (6).

[32] Acacia Communications, Inc. 2018. "Coherent Applications – Trending to the Edge." https://acacia-inc.com/blog/coherent-applications-trending-to-the-edge.

[33] Acacia Communications, Inc. 2022. “Coherent is Knocking on the Data Center Door.” https://acacia-inc.com/blog/coherent-is-knocking-on-the-data-center-door.

[34] Pang, Xiaodan, Weisheng Hu, Gunnar Jacobsen, Sergei Popov, Jiajia Chen, Oskars Ozolins, Rui Lin, et al. 2020. “200 Gbps/Lane IM/DD Technologies for Short Reach Optical Interconnects.” *Journal of Lightwave Technology* 38 (2): 492–503.

[35] Wen, Yang Jing, Yan Cui, and Yusheng Bai. 2020. “Mitigation of Optical Multipath Interference Impact for Directly Detected PAMn System.” *Optics Express* 28 (25): 38317.

[36] Morsy-Osman, Mohamed, Mohammed Sowailem, Eslam El-Fiky, Tristan Goodwill, Thang Hoang, Stephane Lessard, and David V. Plant. 2018. “DSP-Free ‘Coherent-Lite’ Transceiver for next Generation Single Wavelength Optical Intra-Datacenter Interconnects.” *Optics Express* 26 (7): 8890.

[37] Mecozzi, Antonio, Cristian Antonelli, and Mark Shtaif. 2016. “Kramers–Kronig Coherent Receiver.” *Optica* 3 (11): 1220.

[38] Che, Di, An Li, Xi Chen, Qian Hu, Yifei Wang, and William Shieh. 2014. “Stokes Vector Direct Detection for Short-Reach Optical Communication.” *Optics Letters* 39 (11): 3110.

[39] Perin, Jose Krause, Anujit Shastri, and Joseph M. Kahn. 2017. “Design of Low-Power DSP-Free Coherent Receivers for Data Center Links.” *Journal of Lightwave Technology* 35 (21): 4650–62.

[40] Nambath, Nandakumar, Rakesh Ashok, Sarath Manikandan, Nandish Bharat Thaker, Mehul Anghan, Rashmi Kamran, Saurabh Anmadwar, and Shalabh Gupta. 2020. “All-Analog Adaptive Equalizer for Coherent Data Center Interconnects.” *Journal of Lightwave Technology* 38 (21): 5867–74.

[41] Nokia Corporation. 2021. “Silicon photonics: the platform for the 400G era and beyond.” https://www.nokia.com/blog/silicon-photonics-the-platform-for-the-400g-era-and-beyond.

[42] Acacia Communications, Inc. 2017. “What is Siliconization of Optical Interconnect?” https://acacia-inc.com/blog/what-is-siliconization-of-optical-interconnect.

[43] Li, G. L., and P. K.L. Yu. 2003. “Optical Intensity Modulators for Digital and Analog Applications.” *Journal of Lightwave Technology* 21 (9): 2010–30.

[44] He, Mingbo, Mengyue Xu, Yuxuan Ren, Jian Jian, Ziliang Ruan, Yongsheng Xu, Shengqian Gao, et al. 2019. “High-Performance Hybrid Silicon and Lithium Niobate Mach–Zehnder Modulators for 100 Gbit s -1 and Beyond.” *Nature Photonics* 13 (5): 359–64.

[45] Lange, Sophie, Stefan Wolf, Joachim Lutz, Lars Altenhain, Rolf Schmid, Ronald Kaiser, Martin Schell, Christian Koos, and Sebastian Randel. 2018. “100 GBd Intensity Modulation and Direct Detection with an InP-Based Monolithic DFB Laser Mach-Zehnder Modulator.” *Journal of Lightwave Technology* 36 (1): 97–102.

[46] L. Chrostowski and M. Hochberg, *Silicon Photonics Design*. Cambridge: Cambridge University Press, 2015.

[47] Nedeljkovic, Milos, Richard Soref, and Goran Z. Mashanovich. 2011. “Free-Carrier Electrorefraction and Electroabsorption Modulation Predictions for Silicon over the 1-14-Mm Infrared Wavelength Range.” *IEEE Photonics Journal* 3 (6): 1171–80.

[48] Yu, Hui, and Wim Bogaerts. 2012. “An Equivalent Circuit Model of the Traveling Wave Electrode for Carrier-Depletion-Based Silicon Optical Modulators.” *Journal of Lightwave Technology* 30 (11): 1602–9.

[49] Zhou, Yanyang, Linjie Zhou, Haike Zhu, Chiyan Wong, Yida Wen, Lei Liu, Xinwan Li, and Jianping Chen. 2016. “Modeling and Optimization of a Single-Drive Push–Pull Silicon Mach–Zehnder Modulator.” *Photonics Research* 4 (4): 153.

[50] Zhou, Yanyang, Linjie Zhou, Feiran Su, Xinwan Li, and Jianping Chen. 2016. “Linearity Measurement and Pulse Amplitude Modulation in a Silicon Single-Drive Push-Pull Mach-Zehnder Modulator.” *Journal of Lightwave Technology* 34 (14): 3323–29.

[51] Kim, Younghyun, Mitsuru Takenaka, Takenori Osada, Masahiko Hata, and Shinichi Takagi. 2014. “Strain-Induced Enhancement of Plasma Dispersion Effect and Free-Carrier Absorption in SiGe Optical Modulators.” *Scientific Reports* 4.

[52] Srinivasan, Srinivasan Ashwyn, Marianna Pantouvaki, Shashank Gupta, Hong Tao Chen, Peter Verheyen, Guy Lepage, Gunther Roelkens, et al. 2016. “56 Gb/s Germanium Waveguide Electro-Absorption Modulator.” *Journal of Lightwave Technology* 34 (2): 419–24.

[53] Tang, Yongbo, Jonathan D. Peters, and John E. Bowers. "Over 67 GHz bandwidth hybrid silicon electroabsorption modulator with asymmetric segmented electrode for 1.3 μm transmission." *Optics express* 20.10 (2012): 11529-11535.

[54] M. Webster, P. Gothoskar, V. Patel, D. Piede, S. Anderson, R. Tummidi, D. Adams, C. Appel, P. Metz, S. Sunder, B. Dama, and K. Shastri., "An efficient MOS-capacitor based silicon modulator and CMOS drivers for optical transmitters." *11th International Conference on Group IV Photonics (GFP)*. IEEE, 2014.

[55] Han, Jae Hoon, Frederic Boeuf, Junichi Fujikata, Shigeki Takahashi, Shinichi Takagi, and Mitsuru Takenaka. 2017. “Efficient Low-Loss InGaAsP/Si Hybrid MOS Optical Modulator.” *Nature Photonics* 11 (8): 486–90.

[56] Harris, Nicholas C., Yangjin Ma, Jacob Mower, Tom Baehr-Jones, Dirk Englund, Michael Hochberg, and Christophe Galland. 2014. “Efficient, Compact and Low Loss Thermo-Optic Phase Shifter in Silicon.” *Optics Express* 22 (9): 10487.

[57] Wu, Xinru, Ranjeet Kumar, Duanni Huang, Chaoxuan Ma, Guan Lin Su, Xiaoxi Wang, Songtao Liu, and Haisheng Rong. 2023. “A Single-Chip High-Speed Silicon Photonic Transmitter with Integrated Laser and Micro-Ring Modulator.” In *IEEE International Conference on Group IV Photonics GFP*. Vol. 2023-April. IEEE Computer Society.

[58] D. Petousi, L. Zimmermann, P. Rito, M. Kroh, D. Knoll, S. Lischke, C. Mai, I. G. Lopez, A. C. Ulusoy, G. Winzer, K. Voigt, and K. Petermann, "Monolithic Photonic BiCMOS Sub-System Comprising MZM and Segmented Driver with 13 dB ER at 28 Gb/s," in *Conference on Lasers and Electro-Optics*, OSA Technical Digest (2016) (Optica Publishing Group, 2016), paper STu4G.3.

[59] Dong, Po, Chongjin Xie, Lawrence L Buhl, and Young-Kai Chen. “Silicon Microring Modulators for Advanced Modulation Formats.” *Optical Fiber Communication Conference*. Optica Publishing Group, 2013.

[60] Dong, Po, Chongjin Xie, Long Chen, Nicolas K Fontaine, and Young-Kai Chen. "Experimental demonstration of microring quadrature phase-shift keying modulators." *Optics letters* 37.7 (2012): 1178-1180.

[61] Shin, Myungjin, Yoojin Ban, Byung Min Yu, Min Hyeong Kim, Jinsoo Rhim, Lars Zimmermann, and Woo Young Choi. 2017. “A Linear Equivalent Circuit Model for Depletion-Type Silicon Microring Modulators.” *IEEE Transactions on Electron Devices* 64 (3): 1140–45.

[62] Kim, Minkyu, Myungjin Shin, Min-Hyeong Kim, Byung-Min Yu, Younghyun Kim, Yoojin Ban, Stefan Lischke, Christian Mai, Lars Zimmermann, and Woo-Young Choi. 2019. “Large-Signal SPICE Model for Depletion-Type Silicon Ring Modulators.” *Photonics Research* 7 (9): 948.

[63] Rhim, Jinsoo, Yoojin Ban, Byung-Min Yu, Jeong-Min Lee, and Woo-Young Choi. 2015. “Verilog-A Behavioral Model for Resonance-Modulated Silicon Micro-Ring Modulator.” *Optics Express* 23 (7): 8762.

[64] Shin, Myung Jin, Yoojin Ban, Byung Min Yu, Jinsoo Rhim, Lars Zimmermann, and Woo Young Choi. 2016. “Parametric Characterization of Self-Heating in Depletion-Type Si Micro-Ring Modulators.” *IEEE Journal of Selected Topics in Quantum Electronics* 22 (6): 116–22.

[65] Byung-Min Yu, Byung-Min Yu, Myungjin Shin Myungjin Shin, Min-Hyeong Kim Min-Hyeong Kim, Lars Zimmermann Lars Zimmermann, and Woo-Young Choi Woo-Young Choi. 2017. “Influence of Dynamic Power Dissipation on Si MRM Modulation Characteristics.” *Chinese Optics Letters* 15 (7): 071301.

[66] Jo, Youngkwan, Christian Mai, Stefan Lischke, Zimmermann Lars, and Woo Young Choi. 2021. “Modulation Linearity Characterization of Si Ring Modulators.” *Journal of Lightwave Technology*.

[67] Kim, Minkyu, Youngkwan Jo, Stefan Lischke, Christian Mai, Lars Zimmermann, and Woo Young Choi. 2021. “A Temperature-Aware Large-Signal SPICE Model for Depletion-Type Silicon Ring Modulators.” *IEEE Photonics Technology Letters* 33 (17): 947–50.

[68] Kim, Minkyu, Min-Hyeong Kim, Youngkwan Jo, Hyun-Kyu Kim, Stefan Lischke, Christian Mai, Lars Zimmermann, and Woo-Young Choi. 2021. “Silicon Electronic–Photonic Integrated 25 Gb/s Ring

Modulator Transmitter with a Built-in Temperature Controller." *Photonics Research* 9 (4): 507.

[69] Jo, Youngkwan, Yongjin Ji, Minkyu Kim, Stefan Lischke, Christian Mai, Lars Zimmermann, and Woo Young Choi. 2023. "Monte Carlo Characterization of Si Ring Modulator PAM-4 Eye Diagram Performance." *Japanese Journal of Applied Physics* 62 (6).

[70] Bogaerts, W., P. de Heyn, T. van Vaerenbergh, K. de Vos, S. Kumar Selvaraja, T. Claes, P. Dumon, P. Bienstman, D. van Thourhout, and R. Baets. 2012. "Silicon Microring Resonators." *Laser and Photonics Reviews*.

[71] Kim, Hyun-Kyu, Minkyu Kim, Min-hyeong Kim, Youngkwan Jo, Stefan Lischke, Christian Mai, Lars Zimmermann, and Woo-Young Choi. 2021. "Si Photonic-Electronic Monolithically Integrated Optical Receiver with a Built-in Temperature-Controlled Wavelength Filter." *Optics Express* 29 (6): 9565.

[72] Dong, Po. 2016. "Silicon Photonic Integrated Circuits for Wavelength-Division Multiplexing Applications." *IEEE Journal of Selected Topics in Quantum Electronics* 22 (6): 370–78.

[73] Qianfan Xu, Sasikanth Manipatruni, Brad Schmidt, Jagat Shakya, and Michal Lipson, "12.5 Gbit/s carrier-injection-based silicon micro-ring silicon modulators," Opt. Express 15, 430-436 (2007).

[74] Sun, Jie, Ranjeet Kumar, Meer Sakib, Jeffrey B. Driscoll, Hasitha Jayatilleka, and Haisheng Rong. 2019. "A 128 Gb/s PAM4 Silicon Microring Modulator With Integrated Thermo-Optic Resonance Tuning." *Journal of Lightwave Technology* 37 (1): 110–15.

[75] Little, B E, S T Chu, H A Haus, J Foresi, and J.-P Laine. 1997. "Microring Resonator Channel Dropping Filters." *Journal of Lightwave Technology* 15 (6): 998-1005.

[76] Frey, Bradley J., Douglas B. Leviton, and Timothy J. Madison. 2006. “Temperature-Dependent Refractive Index of Silicon and Germanium.” In *Optomechanical Technologies for Astronomy*, 6273:62732J. SPIE.

[77] Tsang, H. K., and Y. Liu. 2008. “Nonlinear Optical Properties of Silicon Waveguides.” *Semiconductor Science and Technology* 23 (6).

[78] Leuthold, J., C. Koos, and W. Freude. 2010. “Nonlinear Silicon Photonics.” *Nature Photonics*.

[79] Turner-Foster, Amy C, Mark A Foster, Jacob S Levy, Carl B Poitras, Reza Salem, Alexander L Gaeta, Michal Lipson, et al. 2002. “Demonstration of High Raman Gain in a Submicrometer-Size Silicon-on-Insulator Waveguide.” *J. Lightwave Technol*. Vol. 10.

[80] Bridges, William B, and James H Schaffner. 1995. “Distortion in Linearized Electrooptic Modulators.” *IEEE Transactions on Microwave Theory and Techniques*, *43*(9): 2184-2197.

[81] Jain, Aditya, Navid Hosseinzadeh, Xinru Wu, Hon Ki Tsang, Roger Helkey, John E. Bowers, and James F. Buckwalter. 2019. “A High Spur-Free Dynamic Range Silicon DC Kerr Ring Modulator for RF Applications.” *Journal of Lightwave Technology* 37 (13): 3261–72.

[82] Jo, Youngkwan, Yongjin Ji, Minkyu Kim, Hyun Kyu Kim, Min Hyeong Kim, Stefan Lischke, Christian Mai, Lars Zimmermann, and Woo Young Choi. 2023. “A Si Photonic BiCMOS Coherent QPSK Transmitter Based on Parallel-Dual Ring Modulators.” *2023 IEEE Silicon Photonics Conference (SiPhotonics)*, Washington, DC, USA, 2023, pp. 1-2.

[83] Seiler, Pascal M., Karsten Voigt, Anna Peczek, Galina Georgieva, Stefan Lischke, Andrea Malignaggi, and Lars Zimmermann. 2022.

"Multiband Silicon Photonic EPIC Coherent Receiver for 64 GBd QPSK." *Journal of Lightwave Technology* 40 (10): 3331–37.

[84] Weckenmann, Erwan, Laurent Bramerie, Mathilde Gay, Diego Perez-Galacho, Frederic Boeuf, Lucas Deniel, Delphine Marris-Morini, and Christophe Peucheret. 2022. "Frequency Chirp Characterization of Silicon Ring Resonator Modulators." *IEEE Photonics Technology Letters* 34 (12): 653–56.

[85] P. M. Seiler, G. Georgieva, A. Peczek, M. Oberon, C. Mai, S. Lischke, A. Malignaggi, and L. Zimmermann, "Monolithically Integrated O-Band Coherent ROSA Featuring 2D Grating Couplers for Self-Homodyne Intra Data Center Links," IEEE Photonics J **15**(3), (2023).

[86] K. Voigt, L. Zimmermann, G. Winzer, H. Tian, B. Tillack and K. Petermann, "Fully passive Si-photonic 90° hybrid for coherent receiver applications," *2011 37th European Conference and Exhibition on Optical Communication*, Geneva, Switzerland, 2011, pp. 1-3.

[87] G. Dziallas, A. Fatemi, A. Peczek, L. Zimmermann, A. Malignaggi, and G. Kahmen, "A 56-Gb/s Optical Receiver with 2.08-μA Noise Monolithically Integrated into a 250-nm SiGe BiCMOS Technology," IEEE Trans Microw Theory Tech **70**(1), 392–401 (2022).

[88] A. Awny, R. Nagulapalli, M. Kroh, J. Hoffmann, P. Runge, D. Micusik, G. Fischer, A. C. Ulusoy, M. Ko, and Di. Kissinger, "A Linear Differential Transimpedance Amplifier for 100-Gb/s Integrated Coherent Optical Fiber Receivers," IEEE Trans Microw Theory Tech **66**(2), 973–986 (2018).

[89] Seiler, Pascal M., Gregor Ronniger, Ute Troppenz, Ariane Sigmund, Martin Moehrle, Anna Peczek, and Lars Zimmermann. 2019.

“Novel Concept for VCSEL Enhanced Silicon Photonic Coherent Transceiver.” *AIP Advances* 9 (10).

[90] M. Seimetz, "Laser Linewidth Limitations for Optical Systems with High-Order Modulation Employing Feed Forward Digital Carrier Phase Estimation," *OFC/NFOEC 2008 - 2008 Conference on Optical Fiber Communication/National Fiber Optic Engineers Conference*, San Diego, CA, USA, 2008, pp. 1-3.

[91] D. S. Ly-Gagnon, S. Tsukamoto, K. Katoh, and K. Kikuchi, "Coherent detection of optical quadrature phase-shift keying signals with carrier phase estimation," in *Journal of Lightwave Technology* **24**(1), 12–20 (2006).

[92] I. Fatadin, D. Ives, and S. J. Savory, "Blind equalization and carrier phase recovery in a 16-QAM optical coherent system," in *Journal of Lightwave Technology* **27**(15), 3042–3049 (2009).

[93] G. Georgieva, P. M. Seiler, C. Mai, A. Peczek, K. Petermann and L. Zimmermann, "A Polarization-Independent Zig-Zag-Tilted Ovals Grating Coupler in a 0.25 µm Photonic BiCMOS Technology," *2022 European Conference on Optical Communication (ECOC)*, Basel, Switzerland, 2022, pp. 1-4.

[94] A. Geravand, Z. Zheng, S. Levasseur, L. A. Rusch and W. Shi, "Ultra-Compact Silicon Modulator for 124 GBaud Coherent Optical Links," *2023 IEEE Silicon Photonics Conference (SiPhotonics)*, Washington, DC, USA, 2023, pp. 1-2.

[95] X. Chen, A. Mistry, M. Bahadori, K. Padmaraju, M. Malinowski, D. Che, R. Sukkar, R. Younce, A. Horth, Y. Dziashko, H. Guan, R. Shi, D. Gill, A. Seyoum, J. Naik, D. Lim, A. El Sayed, A. Rylyakov, M. Schmidt, Z. Luo, P. Magill, G. Burrell, J. Basak, D. Chapman, A. Mikami, Y. Man, A. Leven, N. A. F. Jaeger, “Demonstration of a Silicon Ring Resonator Coupling-Modulator-based Coherent Optical Sub-Assembly Operating at 802 Gbps,” *2023 European*

Conference on Optical Communication (ECOC), Glasgow, Scotland, 2023, pp. 1-4 (to be published).

[96] Liu, J., Maharry, A., Wissing, A., Andrade, H., Misak, S. M., Gilardi, G., Liao, S., Liu, A., Akulova, Y., Coldren, L. A., Buckwalter, J. F., & Schow, C. L., "First O-band silicon coherent transmitter with integrated hybrid tunable laser and SOAs." *Silicon Photonics XVIII*. Vol. 12426. SPIE, 2023.

[97] Maharry, A., Liu, J., Misak, S., Andrade, H., Valenzuela, L. A., Gilardi, G., Liao, S., Liu, A., Akulova, Y., Coldren, L., Buckwalter, J. F., & Schow, C. L., "First Demonstration of an O-Band Coherent Link for Intra-Data Center Applications," in *Journal of Lightwave Technology*, vol. 41, no. 21, pp. 6643-6650, 1 Nov.1, 2023.

[98] Valenzuela, L. A., Xia, Y., Maharry, A., Andrade, H., Schow, C. L., & Buckwalter, J. F., "A 50-GBaud QPSK Optical Receiver With a Phase/Frequency Detector for Energy-Efficient Intra-Data Center Interconnects," in *IEEE Open Journal of the Solid-State Circuits Society*, vol. 2, pp. 50-60, 2022.

[99] Fujitsu Optical Components Limited, "96Gbaud Integrated Coherent Receiver (FIM24942)."

[100] Li, H., Balamurugan, G., Kim, T., Sakib, M. N., Kumar, R., Rong, H., ... & Casper, B., “A 3-D-integrated silicon photonic microring-based 112-Gb/s PAM-4 transmitter with nonlinear equalization and thermal control,” *IEEE Journal of Solid-State Circuits*, *56*(1), 19-29, 2020.

Abstract (In Korean)

링 변조기 기반 실리콘 포토닉 BiCMOS 코히런트 직교 위상 편이 변조 송신기

데이터 센터의 급격한 성장은 다양한 응용 프로그램에서 급증하는 데이터 트래픽 수요로 인해 전기 연결에서 성능, 소형 및 고 데이터 용량의 장점을 갖는 광 연결로의 전환을 촉발시켰다. 실리콘 포토닉스는 silicon-on-insulator (SOI) 공정을 바탕으로 한 경제성과 확장 가능성을 통해 광 집적 회로를 대량 생산하기 위한 유망한 해결책으로 등장하며 광 트랜스시버 등의 다양한 응용 분야에 활용되고 있다.

광 트랜스시버의 광 변조 형식에는 두 가지 주요 트렌드인 진폭 변조 직접 검출과 코히런트 광 변조가 있다. 코히런트 광 변조는 요구되는 수신기 감도가 비교적 작고, 광 신호의 편광 및 고차 변조를 통한 데이터 전송 용량의 증가가 가능하고, 파장 다중 분할의 낮은 필요성으로 인한 줄어든 하드웨어 비용 등의 여러 이점을 제공한다. 또한, 코히런트 광 트랜스시버는 간소화된 디지털 신호 처리 및 수신기 구조라는 장점을 필두로, 기존의 장거리 송수신의 응용만이 아니라 단거리 데이터 센터 연결로 응용이 확대되고 있다.

효율적인 광 변조기는 실리콘 포토닉 기반의 저전력 및 고 용량 광 트랜스시버를 집적하고 구현하는 데 중요한 역할을 한다. 이를 위해 고 에너지 효율, 작은 크기 및 넓은 변조 대역폭을 장점으로 하는 공핍형 실리콘 링 변조기는 Mach-Zehnder 변조기를 대체할 유망한 후보로 다양한 응용 분야에서 많은 연구 및 개발이 이루어지고 있다. 또한, 링 변조기는 플러그 형태의 트랜스시버에서 co-packaged optics (CPOs)로의 전환 단계에서 요구되는 작은 장치 크기와 저전력 소비에 대한 해결책을 제공한다.

본 연구에서 링 변조기 기반의 실리콘 포토닉 코히런트 광-전자 송신기 집적회로가 0.25-μm 실리콘 포토닉 BiCMOS 공정을 바탕으로 구현되고, 28-Gbaud 직교 위상 변이 변조 신호에 대해 검증된다. 효율적인 송신기를 구현하기 위해 링 변조기는 위상 변조에 대해 특성화되고 최적화된다. 제작된 코히런트 송신기는 다양한 광원과 같은 여러 측정 구성에 대해, 동일한 포토닉 BiCMOS 공정에서 구현된 코히런트 수신기와 함께 검증되며, 이러한 결과는 링 변조기 기반 실리콘 포토닉 BiCMOS 코히런트 송신기의 단일 칩 코히런트 트랜스시버로 확장 가능성을 보여준다.

핵심 단어: 광 연결, 실리콘 포토닉스, 실리콘 포토닉 BiCMOS 공정, 단일 칩 집적, 광-전자 집적회로, 코히런트 광 통신, 직교 위상 편이 변조기, 코히런트 송신기, 링 변조기, 변조기 구동회로, 코히런트 수신기.

List of Publications

International Journal Papers

[1] **Youngkwan Jo**, Stefan Lischke, Christian Mai, Lars Zimmermann, and Woo-Young Choi, "Modulation Linearity Characterization of Si Ring Modulators," IEEE/OSA Journal of Lightwave Technology, Vol. 39, No. 24, pp.7842-7849, Dec. 2021.

[2] **Youngkwan Jo**, Yongjin Ji, Minkyu Kim, Stefan Lischke, Christian Mai, Lars Zimmermann and Woo-Young Choi, "Monte Carlo characterization of Si ring modulator PAM-4 eye diagram performance," Japanese Journal of Applied Physics, Vol. 62, No. 6, pp.066502-1 - 8, Jun. 2023.

[3] Younghyun Kim, **Youngkwan Jo**, Minkyu Kim, Byung-Min Yu, Christian Mai, Stefan Lischke, Lars Zimmermann, and Woo-Young Choi, "Parametric Optimization of Depletion-type Si Micro-ring Modulator Performances," Japanese Journal of Applied Physics, Vol. 58, No. 6, pp.062006-1 - 6, Jun. 2019.

[4] Hyun-Kyu Kim, Minkyu Kim, Min-Hyeong Kim, **Youngkwan Jo**, Stefan Lischke, Christian Mai, Lars Zimmermann and Woo-Young Choi, "Si photonic-electronic monolithically integrated optical receiver with a built-in temperature-controlled wavelength filter," Optics Express, Vol. 29, No. 6, pp.9565-9573, Mar. 2021.

[5] Minkyu Kim, Min-Hyeong Kim, **Youngkwan Jo**, Hyun-Kyu Kim, Stefan Lischke, Christian Mai, Lars Zimmermann, and Woo-Young Choi, "A Silicon Electronic-Photonic Integrated 25-Gb/s Ring Modulator Transmitter with a Built-in Temperature Controller," Photonics Research, Vol. 9, No. 4, pp.507-513, Apr. 2021.

[6] Minkyu Kim, **Youngkwan Jo**, Stefan Lischke, Christian Mai, Lars Zimmermann, and Woo-Young Choi, "A Temperature-Aware Large-signal SPICE Model for Depletion-type Silicon Ring Modulators," IEEE Photonics Technology Letters, Vol. 33, No. 17, pp. 947-950, Sep. 2021.

[7] Hyun-Kyu Kim, Jae-Ho Lee, Minkyu Kim, **Youngkwan Jo**, Stefan Lischke, Christian Mai, Lars Zimmermann, and Woo-Young Choi, "A 4-λ × 28-Gb/s/λ Silicon Ring-resonator-based WDM Receiver with a Reconfigurable Temperature Controller," IEEE/OPG Journal of Lightwave Technology, November 2023, Accepted (In press).

Domestic Journal Papers

[1] 성민혁, **조영관**, 김민규, 박강엽, 오원석, 최우영, “25-Gbps Depletion-Type 실리콘 링 변조기 성능 극대화를 위한 소자 구조 최적화,” 전자공학회 논문지, Vol.58, No.01, pp.21-29, 2021년 1월.

International Conference Presentations

[1] **Youngkwan Jo**, Byung-Min Yu, Christian Mai, Stefan Lischke, Lars Zimmerman and Woo-Young Choi, "Modulation linearity analysis of depletion-type Si Ring Modulator," SPIE Photonics West, San Francisco, California, USA, 1-7 Feb. 2019.

[2] **Youngkwan Jo**, Yongjin Ji, Minkyu Kim, Stefan Lischke, Christian Mai, Lars Zimmermann and Woo-Young Choi, "Parametric Monte-Carlo Characterization of Si Ring Modulators," IEEE Group IV Photonics (GFP), Virtual Conference, 7-10 Dec. 2021.

[3] **Youngkwan Jo**, Yongjin Ji, Minkyu Kim, Hyun-Kyu Kim, Min-Hyeong Kim, Stefan Lischke, Christian Mai, Lars Zimmermann and Woo-Young Choi, "A Si Photonic BiCMOS Coherent QPSK Transmitter Based on Parallel-Dual Ring Modulators," IEEE SiPhotonics 2023, Arlington, VA, USA, 4-7 Apr. 2023.

[4] **Youngkwan Jo**, Yongjin Ji, Hyun-Kyu Kim, Stefan Lischke, Christian Mai, Lars Zimmermann and Woo-Young Choi, "Complex Electro-Optic Frequency-Response Characterization of a Si Ring Modulator," IEEE SiPhotonics 2024, Tokyo, Japan, April 2024, Accepted (to be presented).

[5] Hyun-Kyu Kim, **Youngkwan Jo**, Minkyu Kim, Hyun-Yong Jung, Christian Mai, Stefan Lischke, Lars Zimmermann and Woo-Young Choi, "A Monolithically Integrated 2 × 25-Gb/s Si Photonic WDM Receiver with Thermally-Tunable Ring-Resonator Filters," SPIE Photonics West, San Francisco, California, USA, 1-6 Feb. 2020.

[6] Minkyu Kim, Min-Hyeong Kim, **Youngkwan Jo**, Hyun-Kyu Kim, Stefan Lischke, Christian Mai, Lars Zimmermann, and Woo-Young Choi, "A Fully Integrated 25 Gb/s Si Ring Modulator Transmitter

with a Temperature Controller," Optical Fiber Communications Conference (OFC), San Diego, California, USA, 8-12 Mar. 2020.

[7] Jae-Ho Lee, Hyun-Kyu Kim, Minkyu Kim, **Youngkwan Jo**, Stefan Lischke, Christian Mai, Lars Zimmermann, and Woo-Young Choi, "A 112-Gb/s Hybrid-Integrated Si Photonic WDM Receiver with Ring-Resonator Filters," IEEE SiPhotonics 2024, Tokyo, Japan, April 2024, Accepted (to be presented).

Domestic Conference Presentations

[1] **조영관**, 유병민, 최우영, “Silicon Micro-Ring 기반 Optical BPSK Modulator 설계,” 2017 Photonics Conference, Jeju, Korea, 8-10 Nov. 2017.

[2] **Youngkwan Jo**, Byung-Min Yu, Christian Mai, Stefan Lischke, Lars Zimmerman and Woo-Young Choi, “Depletion-Type Si Ring Modulators의 Modulation Linearity Analysis,” 2018 Photonics Conference, Pyeongchang, Korea, 28-30 Nov. 2018.

[3] **조영관**, 지용진, 김민규, 최우영, “Si Micro-Ring 변조기 40Gbps PAM4 eye diagram의 Monte-Carlo 분석,” 제29회 광전자 및 광통신 학술대회 (COOC 2022), Busan, Korea, 25-27 May. 2022.

[4] **조영관**, Matthieu Oberon, Anna Peczek, 지용진, 김현규, Pascal M. Seiler, Lars Zimmermann, 최우영, “링 변조기 기반 컴팩트 실리콘 포토닉 BiCMOS 코히런트 트랜스시버,” 2023 Photonics Conference, Pyeongchang, Korea, 29 Nov. - 1 Dec. 2023.

[5] 김영현, 유병민, **조영관**, 김민규, 최우영, “Modulation performance optimization of 40-Gbps Si micro-ring modulators,” 2017 Photonics Conference, Jeju, Korea, 8-10 Nov. 2017.

[6] 성민혁, **조영관**, 최우영, “1.3um 대역 25-Gbps Silicon Micro-Ring Modulator의 Parametric Optimization,” 2018 Photonics Conference, Pyeongchang, Korea, 28-30 Nov. 2018.

[7] 성민혁, **조영관**, 최우영, “Date Rate에 따른 실리콘 링 변조기의 구조 최적화,” 제26회 광전자 및 광통신 학술대회 (COOC 2019), Busan, Korea, 3-5 Jun. 2019.

[8] 성민혁, **조영관**, 최우영, “Performance Optimization of 25-Gbps O-Band Depletion-Type Silicon Ring Modulators,” 2019 Photonics Conference, Pyeongchang, Korea, 4-6 Dec. 2019.

[9] 지용진, **조영관**, 최우영, “Dependence of 40-Gbps PAM-4 Si MRM Eye Characteristics on Input Optical Wavelength,” 제29회 광전자 및 광통신 학술대회 (COOC 2022), Busan, Korea, 25-27 May. 2022.